

CHARACTERISATION OF ODS Fe-14Cr-2W-0.3Ti BEFORE AND AFTER HIGH TEMPERATURE TRIPLE AND LOW TEMPERATURE SINGLE ION IRRADIATIONS

Abstract

Oxide dispersion strengthened reduced activation ferritic steels are being considered as structural materials for future fusion reactors and Gen IV fission reactors. In this work, the stability of the nanometric oxides after being irradiated at different conditions and temperatures has been investigated. A Fe-14Cr-2W-0.3Ti-0.3Y₂O₃ alloy was simultaneously triple-beam irradiated at 600°C with Fe, He and H ions. The same alloy was irradiated with Fe ions at -80°C. The microstructure of this alloy was investigated using Transmission Electron Microscopy, Atom Probe Tomography and nanoindentation before and after the irradiations. There were no significant changes in the morphology and chemical composition of the nanoparticles after the irradiations, although the size of the smaller ones tends to decrease for both irradiation conditions. Small irradiation-induced bubbles were present after the triple simultaneous irradiation at high temperature. Nanoindentation also shows no significant differences with a slight increase in hardness for the sample irradiated at low temperature, while softening appears in the high temperature irradiation.

Keywords: Oxide Dispersion Strengthened steels, ion irradiation, Transmission Electron Microscopy, nanoindentation, Atom Probe Tomography, nanoparticles.

1. Introduction

In the face of depleting sources of fossil fuels, nuclear fusion is regarded as one of the most promising, low carbon, solutions. At this moment, the International Thermonuclear Experimental Reactor (ITER) is being built [1], after which a Demonstration power plant (DEMO) is planned as the next step towards commercial fusion reactors [2]. One of the biggest challenges is the development of the materials that are to be used in these reactors, especially at high temperatures. Oxide dispersion strengthened (ODS) Fe-Cr alloys are being considered as candidate materials for structural applications. They are envisaged to be used in the first wall of advanced nuclear fusion reactors and as fuel cladding in some GEN IV fission designs, therefore they will have to sustain high doses, as a consequence of the 14 MeV neutron irradiation, operating temperatures up to 700°C, and large amounts of He produced by transmutation reactions [3,4]. It has been shown that a fine dispersion of nanoparticles homogeneously distributed in the matrix of these materials improves their mechanical performance by impeding dislocation motion, raising operating temperatures while also enhancing creep strength [5,6].

The nano-sized yttria particles are chosen for their superior thermodynamic stability, compared to nitrides and carbides, and because they act as sinks for irradiation induced defects [7,8]. ODS materials are usually produced by powder metallurgy involving mechanical alloying (MA) and consolidation by hot isostatic pressing (HIP) or hot extrusion after which they undergo thermomechanical treatments in order to further enhance their mechanical properties [6,9].

Due to the lack of neutron irradiation facilities operating in the fusion energy regime, to simulate the effect of the severe irradiation conditions in the nuclear fusion reactor, materials are usually self-ion irradiated. Moreover, as production of transmutation gasses (He and H) plays a significant role in the evolution of the microstructure, materials can be also irradiated with high doses of He and/or H.

Studies of the ion irradiation induced evolution of nanoparticles in ferritic ODS steels have been inconclusive to date. In the case of 18CrODS irradiated at 500°C with Fe^+ ions, nanoparticles are stable at doses ranging from 4 to 45 dpa [10] while for high doses (150 dpa) the sizes of nanoparticles increase while the number density decreases [11]. For 14YWT irradiated with Ni^{2+} ions at 600°C and irradiation doses ranging from 5 to 100 dpa, with Atom Probe Tomography (APT) it has been observed that nanoparticle sizes and their number densities remained stable, while both values increase when investigated using Energy Filtered Transmission Electron Microscopy (EFTEM) [12]. Wharry et al have recently summarized available experimental studies on nanoparticle evolution under irradiation in ODS steels showing the complexity to fully understand the evolution and mechanisms present [13]. Moreover, comparing irradiations across different batches of materials is difficult due to differing initial chemical compositions, processing conditions and thermomechanical histories. Thus, it is important to investigate materials, from the same batch, irradiated under different conditions using complementary techniques in order to describe the evolution of nanoparticles on different scales, together with any changes in the microstructure and mechanical properties.

In this work, the effects of two different ion irradiations on an ODS Fe-14Cr-2W-0.3Ti steel were investigated. The alloy was simultaneously irradiated with Fe^{5+} , He^+ and H^+ ions at 600°C, or single irradiated with Fe^{5+} ions at -80°C. The microstructure before and after the irradiations was investigated with advanced techniques such as Transmission Electron Microscopy (TEM) and APT and compared with previous positron annihilation spectroscopy (PAS) results. The evolution of the nanoparticles was analysed in terms of their size, shape and chemical composition. Nanoindentation was used to examine possible changes in the hardness of both irradiated samples with respect to the unirradiated one.

2. Experimental

2.1. Material

The nominal composition of the material investigated in this work is Fe-14Cr-2W-0.3Ti-0.3Y₂O₃ (wt%) which, in unirradiated state, will be referred to as 14YWTi. The alloy was produced by adding Y₂O₃ nanoparticles to a high purity elemental powder, mechanically alloyed under H₂ atmosphere and consolidated by hot isostatic pressing (HIP) at 1100 °C and 200 MPa for 2 h. After consolidation, the alloy billets were forged at ~ 1150 °C and subsequently heat treated at 850°C for 2 h. The detailed fabrication procedure can be found in [14]. Samples with dimensions 7×7×0.2 mm³ were mechanically polished with SiC polishing pads and then mirror polished with 50 nm alumina slurry.

2.2 Irradiation conditions

Two irradiations were carried out as detailed below.

2.2.1 JANNuS-Saclay facility

The simultaneous triple-ion irradiation with Fe⁵⁺, He⁺ and H⁺ ions was performed at the JANNuS-Saclay facility in France [15–17]. The samples were irradiated at 600 °C to 30 dpa with Fe⁵⁺, 1500 appm H⁺ and 600 appm He⁺ to simulate fusion relevant conditions. The energies were 14 MeV for Fe⁵⁺, 1.6 MeV for He⁺ and 500 keV for H⁺ and were specifically chosen to achieve the maximum damage (Bragg peak) at the same depth for all ions, see Fig. 1a displaying the SRIM profile for the irradiation. In this case, the Bragg peak is estimated at ~ 2.4 μm from SRIM calculations and limited by the minimum feasible implantation energy of the H⁺ ions (500 keV) [18]. More details about this irradiation can be found in [19]. This sample will be referred to as

14YWTi 600°C.

2.2.2 CMAM facility

A sample of the same material was irradiated at the Centre for Micro Analysis of Materials (CMAM) in Madrid, Spain with a low temperature setup [20,21]. This irradiation was carried out with 1 MeV Fe^+ ions up to a damage of 15 dpa at a temperature of -80°C to avoid possible temperature-related recovery of defects. In this sample, the Bragg peak was estimated at ~ 300 nm from the sample surface, see Fig. 1b. This sample will be referred to as **14YWTi -80°C** .

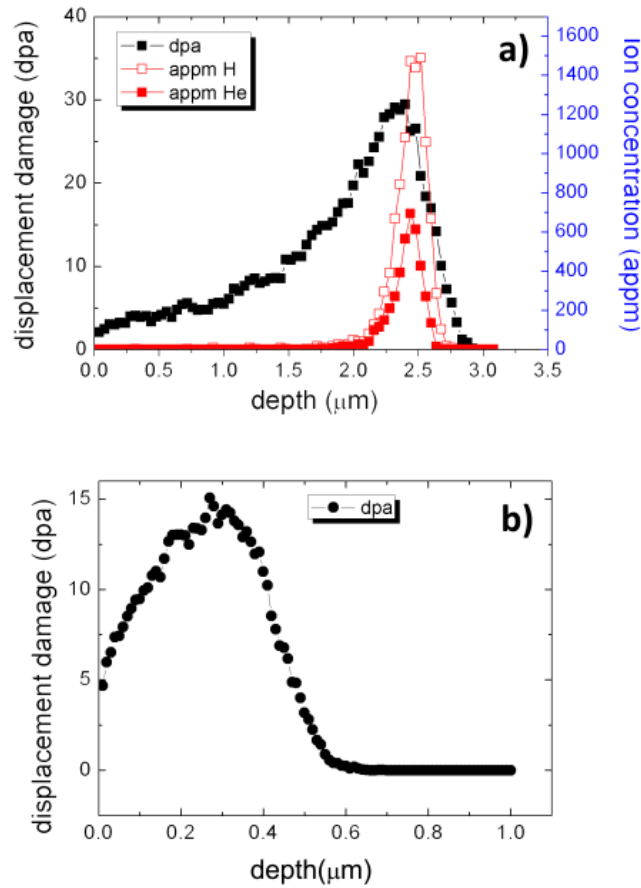


Figure 1. SRIM profiles for a) JANNuS irradiation (He^+ and H^+ ions implantation profile and Fe^{5+} ions damage profile) and b) CMAM irradiation (Fe^+ ions damage profile).

Table 1 shows the relevant parameters (ions, energy, temperature, dose rate and fluence) for the two irradiation conditions.

Irradiation facility	Ion type	Energy	Temp (°C)	Dose rate (ions·cm ⁻² s ⁻¹)	Fluence (ions·cm ⁻²)	Maximum dose (dpa) / concentration (appm)
JANNUS	Fe ⁵⁺	14 MeV	600	8.3 x 10 ¹¹	1.49 x 10 ¹⁶	~30 dpa
	He ⁺	1.6 MeV		8 x 10 ¹⁰	1.4 x 10 ¹⁵	~600 appm
	H ⁺	500 keV		1.97 x 10 ¹¹	3.55 x 10 ¹⁵	~1500 appm
CMAM	Fe ⁺	1 MeV	-80	1.35 x 10 ¹²	6.5 x 10 ¹⁵	~15 dpa

Table 1. Irradiation conditions

2.3 Transmission Electron Microscopy (TEM)

The unirradiated samples were electropolished in a TENUPO 5 twin jet polisher using a solution of 5 vol % perchloric acid in methanol. Irradiated samples for TEM analyses were prepared in a Zeiss AURIGA 40 focused ion beam (FIB) instrument fitted with a scanning electron microscope (SEM). A Ga²⁺ beam was used to mill the trenches, in the site previously covered by a layer of Pt, thus obtaining a cantilever. It was subsequently lifted out, attached to a TEM grid and further milled until electron transparency was reached. The detailed process of this in-situ lift-out method is described in [19]. The investigated FIBed samples are presented in Fig. 2a (14YWTi 600°C) and Fig. 2b (14YWTi -80°C). The original surface location is marked by the remaining Pt at the sides of the lift out sample.

Imaging was done in areas nearby the calculated Bragg peaks, where the maximum damage was achieved. The chemical information was obtained by Scanning Transmission Electron Microscopy- Energy Dispersive Spectroscopy (STEM-EDS) and Energy Filtered Transmission Electron Microscopy (EFTEM) using a JEOL 2200MCO microscope operating at 200 kV beam energy equipped with an Ω -filter and an Oxford Instruments EDS detector. EFTEM elemental maps were extracted using the multiple linear least square (MLLS) method with reference spectra for each element [22].

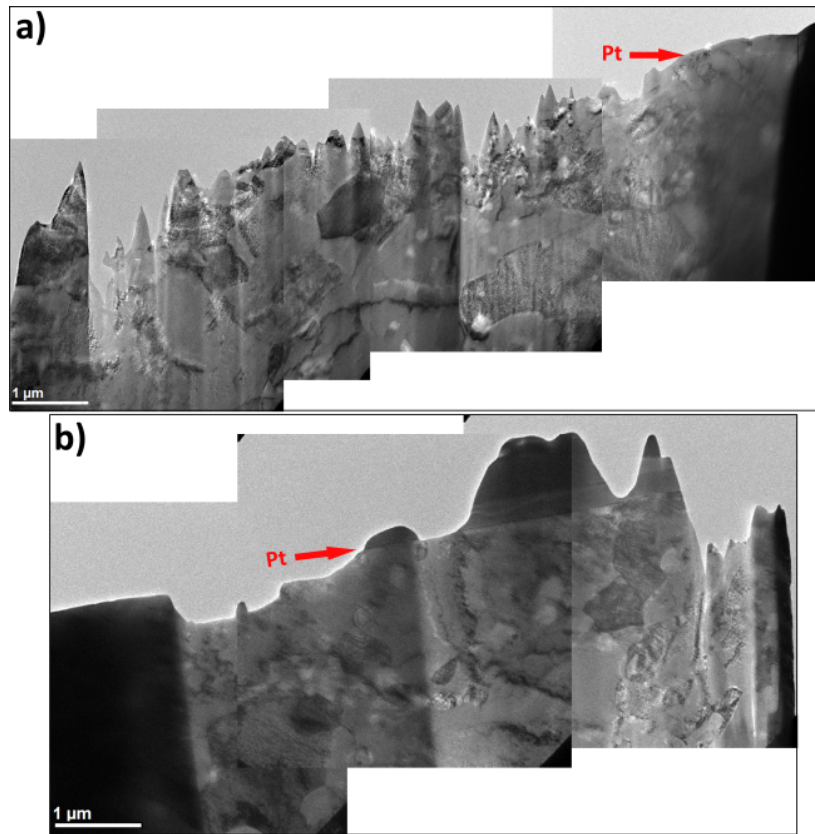


Figure 2. TEM images of FIBed samples of a) 14YWTi 600°C and b) 14YWTi -80°C. The arrows show the position of the remaining platinum layer.

2.4 Atom Probe Tomography (APT)

The unirradiated samples were prepared for APT by standard electropolishing methods [23]. Rod-shaped samples of the material ($0.5 \times 0.5 \times 20 \text{ mm}^3$) were repeatedly dipped into a solution (25 vol% perchloric acid, 75 vol% acetic acid) applying a DC voltage of 15 V, which was later reduced to 10 V as the specimen area was reduced, until the necked region split the sample into 2 parts. These parts were then micropolished with the specimen repeatedly pushed through a gold loop containing a drop of electrolyte (2 vol% perchloric acid, 98 vol% 2-butoxyethanol) with DC voltage going from 8 to 5 V until specimens with the suitable shape for APT (needle shaped with a final tip radius below 100 nm) were obtained. The irradiated samples were prepared by the FIB lift-out method using Zeiss Auriga FIB/SEM and Zeiss NVision 40 FIB/SEM instruments [24].

14YWTi and 14YWTi 600°C samples were run in a CAMECA LEAP3000™ in laser mode ($\lambda=532$ nm), using a laser energy of 0.40 nJ at 200 kHz repetition rate. 14YWTi -80°C sample was run in a CAMECA LEAP5000™ in laser mode ($\lambda= 355$ nm), using a laser energy of 0.040 nJ at 200 kHz repetition rate. The sample temperature was kept at 50K in all the measurements.

For data reconstruction and analysis, the CAMECA IVAS software package and MATLAB software were used. Nanoclusters were identified by using the maximum separation method, which requires two parameters, namely d_{\max} (maximum distance between ions) and N_{\min} (minimum number of ions for a cluster to be non-random) [25]. The cluster size was defined as the Guinier diameter, i.e. twice the Guinier radius [26]. The shape of the clusters was defined in terms of the best-fit ellipsoids. The smallest, middle and largest characteristic lengths of each best-fit ellipsoid enclosing each identified cluster were used to calculate their oblateness (smallest characteristic length/middle characteristic length) and the aspect ratio (middle characteristic length/largest characteristic length). Combination of oblateness and aspect ratio values can be used to define the cluster shape as sphere, rod, lath or disc [27]. The distance between one cluster and its nearest neighbour was calculated as the distance between their centres of mass [26].

2.5 Nanoindentation

Nanoindentation is widely used technique to obtain depth-dependent properties of thin irradiated layers [28,29]. It measures the hardness and elastic modulus of a material from indentation load-displacement data obtained during one cycle of loading and unloading [30]. In this work, continuous stiffness measurements (CSM) were performed with a MTS NanoXP indenter using a Berkovich tip with a maximum indentation displacement of 3 μm for the unirradiated and the JANNuS irradiated samples, and 2 μm for the CMAM irradiated sample. That displacement was the target depth, chosen to encompass layers with maximum irradiation

damage (Bragg peak) in both irradiated samples. All of the samples were indented with an array of 6x6 indents and average hardness and modulus –depth curves plotted.

3. Results

3.1 Microstructure before irradiation

Previous TEM analyses of the unirradiated alloy show a duplex grain structure and the presence of different secondary phases, such as Ti-Cr rich particles with round morphology and sizes ranging from 50 nm to 500 nm as well as Y-Ti rich round nanoparticles with sizes mostly below 30 nm [14]. EDS and EFTEM maps of these Ti-Cr and Y-Ti rich particles are shown in Figs. 3 and 4. The Y-Ti rich nanoparticles, with mean size of 8 ± 5 nm, are found to be quite uniformly dispersed throughout the matrix. Some of them were identified as Y_2TiO_5 oxides, as reported in [14]. The nanoparticle size distribution is presented in the histogram shown in Fig. 5a. The number density of 13 measured regions containing Y-Ti rich nanoparticles and having volumes of the order of 10^{-21} m^3 varies between $(1.2 \pm 0.2) \times 10^{21} \text{ m}^{-3}$ and $(3.8 \pm 0.8) \times 10^{22} \text{ m}^{-3}$ with an average value of $(1.1 \pm 0.2) \times 10^{22} \text{ m}^{-3}$.

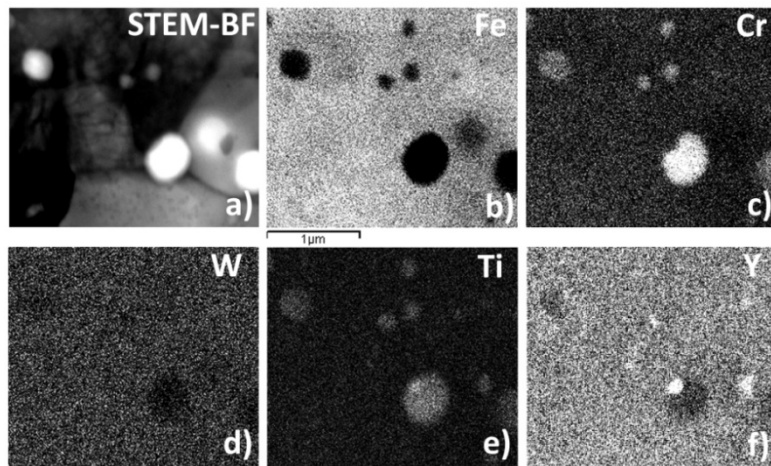


Figure 3. STEM image and EDS elemental maps of the 14YWTi unirradiated alloy. a) BF image, b) Fe K map, c) Cr K map, d) W L map, e) Ti K map, f) Y (K+L) map.

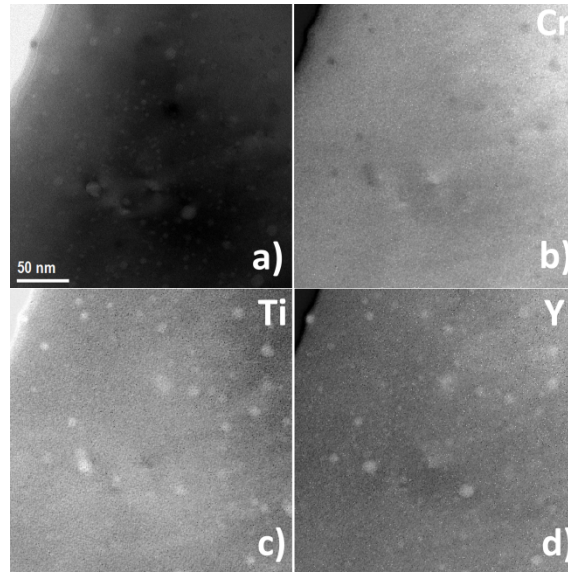


Figure 4. EFTEM elemental maps of the unirradiated 14YWTi alloy showing the morphology and chemical composition of Y-rich nanoparticles a) elastic image, b) Cr M2,3 map, c) Ti M2,3 map, d) Y N2,3 map.

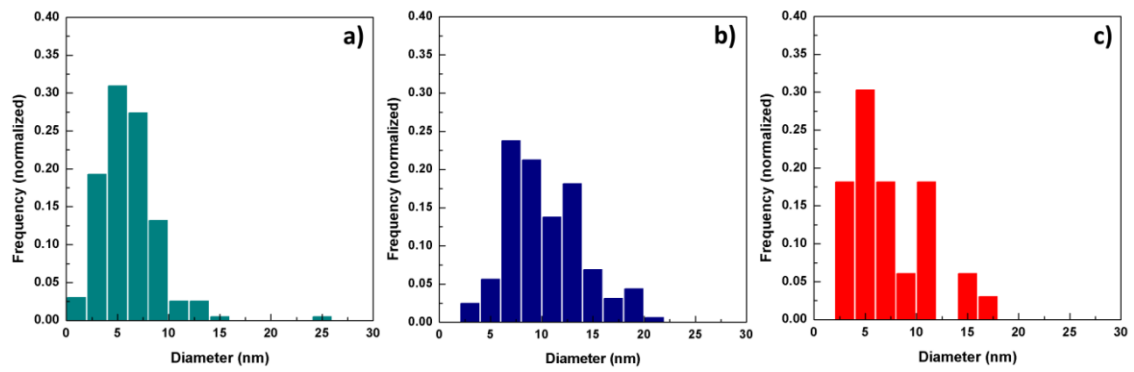


Figure 5. Histograms showing the nanoparticle size distribution for a) unirradiated 14YWTi, b) 14YWTi 600°C and c) 14YWTi -80°C.

In agreement with TEM observations, by APT it was possible to observe Y-Ti-O rich nanoclusters, according to the 3D ion maps displayed in Fig. 6a and Video 1.

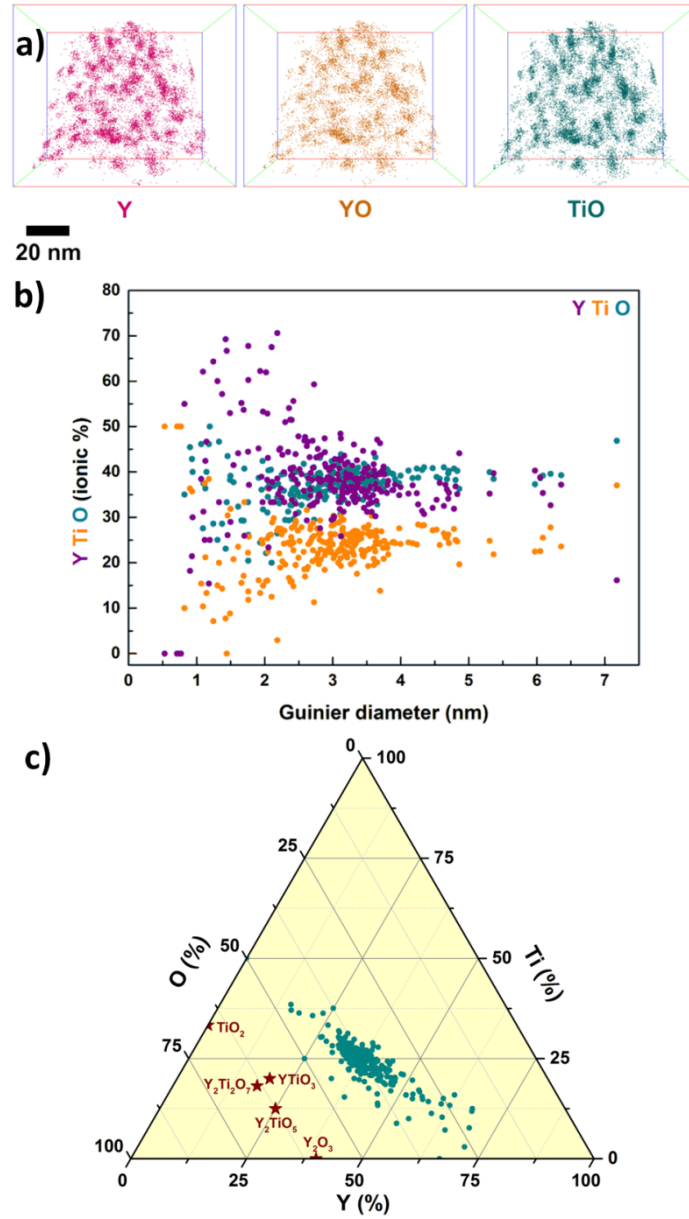


Figure 6. APT measurements for 14YWTi unirradiated. a) 3D-ion maps of Y, YO and TiO [Video 1] Y, Ti and O content in the clusters, b) as a function of their size and c) as a ternary diagram.

Video 1. 3D-ion maps of Y, YO and TiO for 14YWTi unirradiated.

The cluster size distribution obtained from APT reconstructions is shown in Fig. 7a. Sizes were in the range 0.5 to 7 nm with mean size 2.9 ± 1.1 nm. The number densities of measured nanoclusters in two regions with volumes of 2.2 and $1.8 \times 10^{-22} \text{ m}^3$ are $(3.4 \pm 0.7) \times 10^{23} \text{ m}^{-3}$ and $(1.0 \pm 0.2) \times 10^{24} \text{ m}^{-3}$. The shape of the clusters is summarized in Fig. 7b and in Table 2; most of them being spherical. A histogram for the distance between nearest clusters is shown in Fig. 8a. The measured distances are in the range $[2.5, 27]$ nm, with an average value of 9 ± 3 nm.

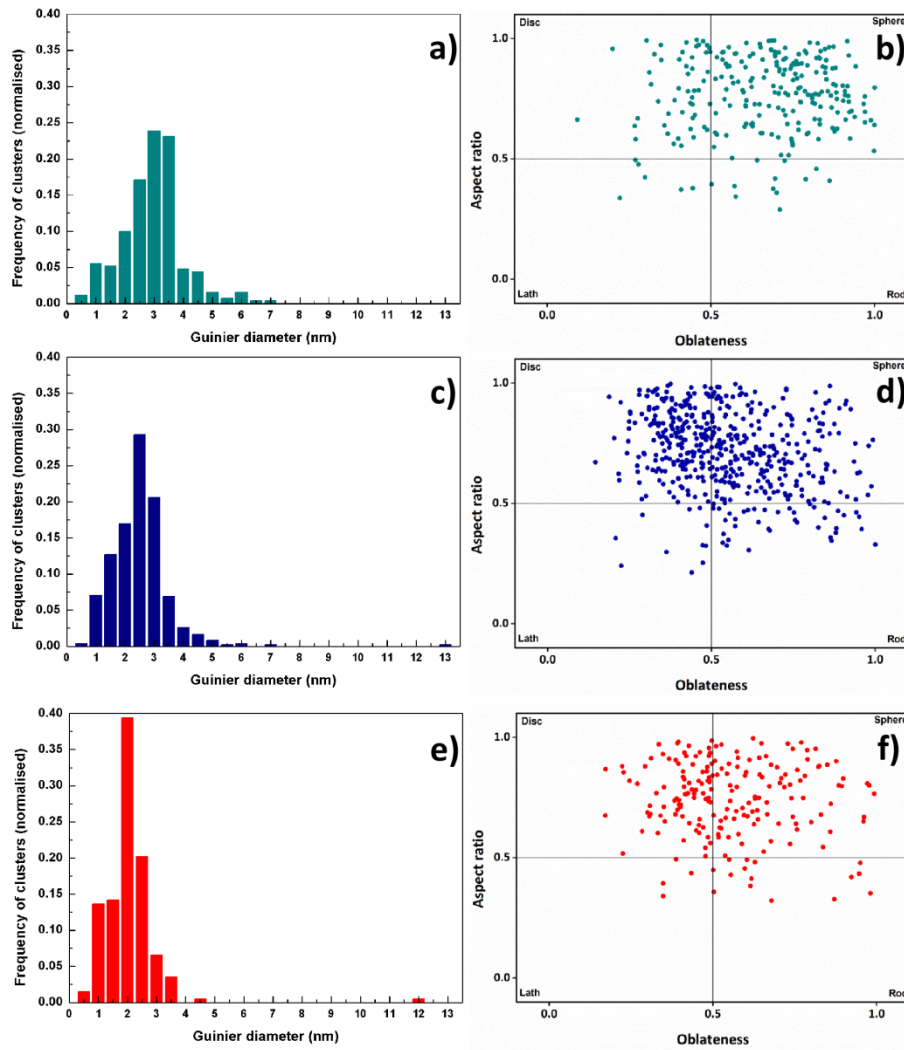


Figure 7. APT cluster size distribution histograms for a) 14YWTi unirradiated, c) 14YWTi 600°C and e) 14YWTi -80°C and cluster shape distribution for b) 14YWTi unirradiated, d) 14YWTi 600°C and f) 14YWTi -80°C.

Sample	Sphere	Disc	Rod	Lath
14YWTi unirradiated	72.5%	20.32%	4.78%	2.4%
14YWTi 600°C	48.69%	41.41%	7.68%	2.22%
14YWTi -80°C	46.97%	43.43%	7.57%	2.02%

Table 2. APT cluster shape quantification for all samples

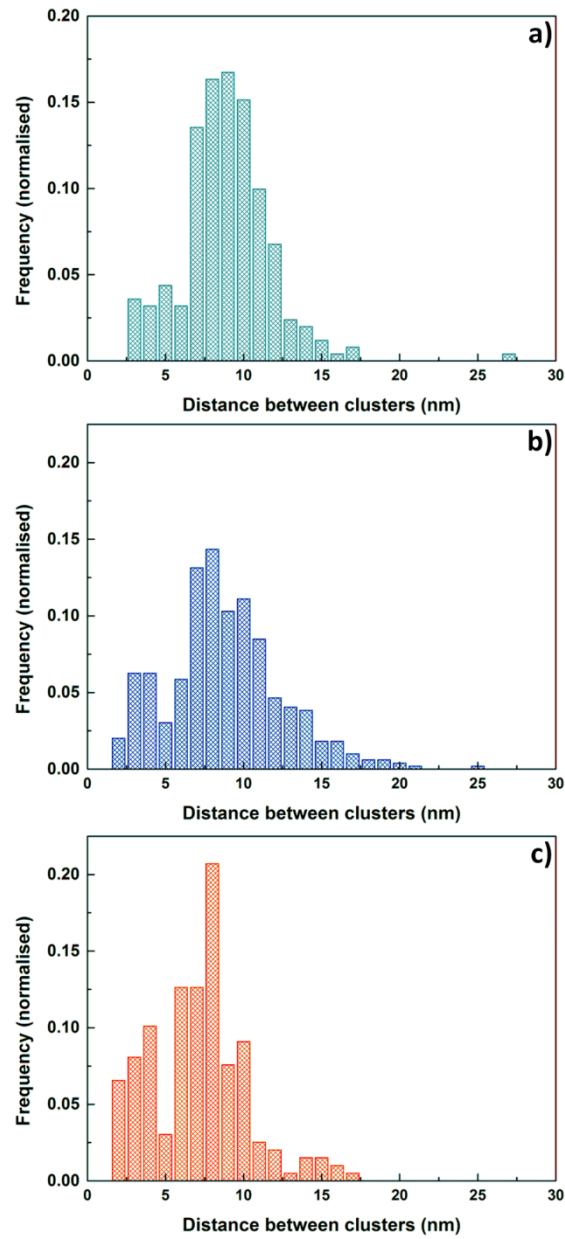


Figure 8. APT distance between clusters for a) 14YWTi unirradiated, b) 14YWTi 600°C and c) 14YWTi -80°C.

The chemical composition of the nanoclusters, i.e. their Y, Ti and O content, is displayed in Fig. 6b as a function of the cluster size and in Fig. 6c as a ternary diagram. The substoichiometry of the smaller nanoparticles (< 4 nm) in a ODS Fe-14Cr model alloy has been observed by the authors in [31] and by Brandes et al. in a similar ODS ferritic steel [32]. The chemical composition of the measured clusters is summarized in Table 3.

The variations in the mean size and number densities of nanoparticles between TEM and APT can be attributed to the different resolutions, sensitivities and volumes measured with the two techniques.

Sample	Y (at. %)	Ti (at. %)	O (at. %)
14YWTi unirradiated	38±10	24±6	38±6
14YWTi 600°C	41±9	21±7	38 ± 4
14YWTi -80°C	39±8	24 ± 6	38±4

Table 3. APT chemical composition of nanoclusters for all samples (averaged values)

3.2 Microstructure after triple irradiation at 600°C

For 14YWTi 600°C, previous TEM analyses show that there are no changes in the grain structure of the alloy [19]. Figs. 9 and 10 depict the distribution of nanoparticles in the irradiated alloy. As for the unirradiated alloy, they have round morphologies and are Ti-Cr or Y- Ti rich. Their size distribution is shown in Fig. 5b, with an average nanoparticle size of 10 ± 4 nm. Number densities of particles measured in five regions with volumes of the order of 10^{-21} m^3 vary between $(3.5 \pm 0.7) \times 10^{21} \text{ m}^{-3}$ and $(6.9 \pm 1.4) \times 10^{21} \text{ m}^{-3}$ with an average value of $(4.8 \pm 1.0) \times 10^{21} \text{ m}^{-3}$ [19]. In

any case, it must be taken into account that the number of nanoparticles measured in this case was much lower, i.e. 150 vs 700 due to the lower number of regions available to be analysed.

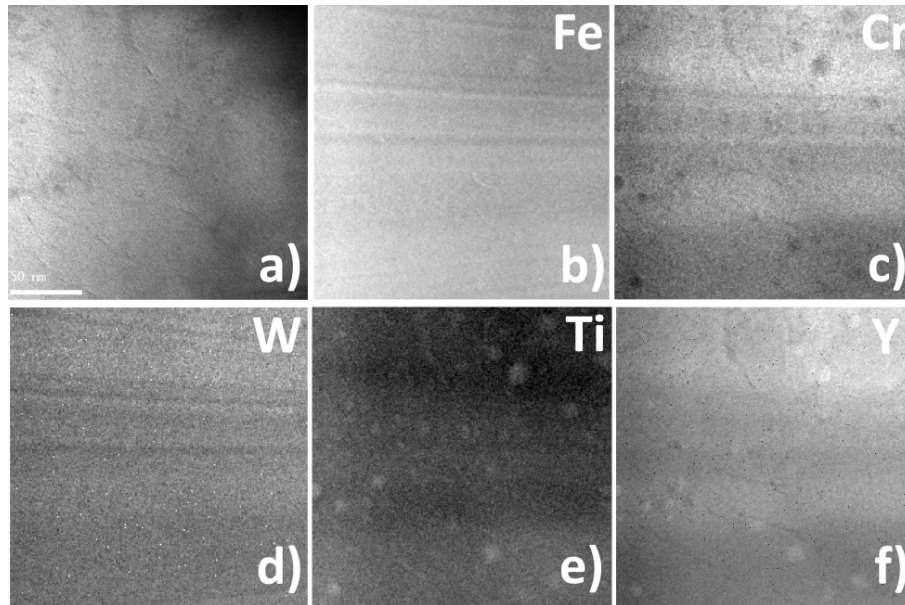


Figure 9. EFTEM elemental maps of the 14YWTi 600°C alloy showing the morphology and chemical composition of Y-rich nanoparticles a) elastic image, b) Fe M2,3 map, c) Cr M2,3 map, d) W (N6,3 + O2,3) map, e) Ti M2,3 map and f) Y N2,3 map.

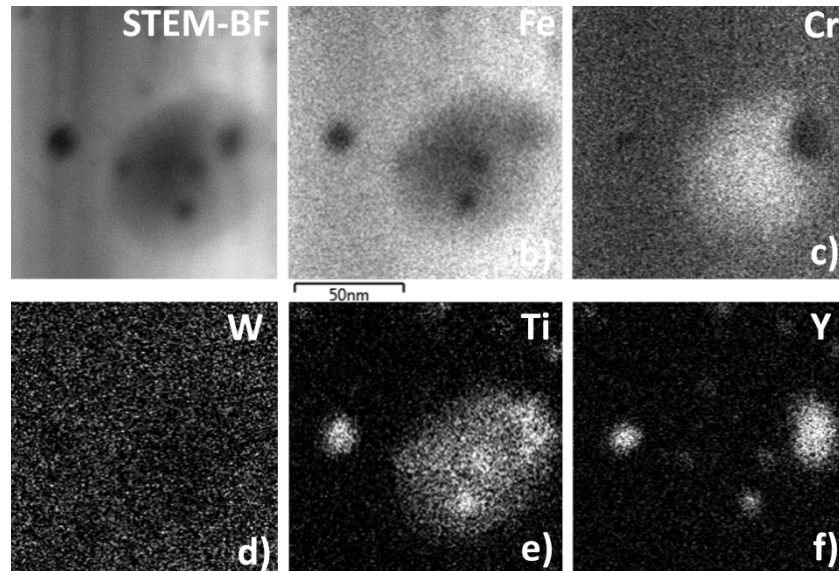


Figure 10. STEM image and EDS elemental maps of the 14YWTi 600°C alloy. a) BF image, b) Fe K map, c) Cr K map, d) W L map, e) Ti K map, f) Y L map.

In this case, four APT datasets with volumes between 2.5×10^{-23} and $2.9 \times 10^{-22} \text{ m}^3$ were analysed; 3D ion maps from one of them are displayed in Fig. 11a and Video 2.

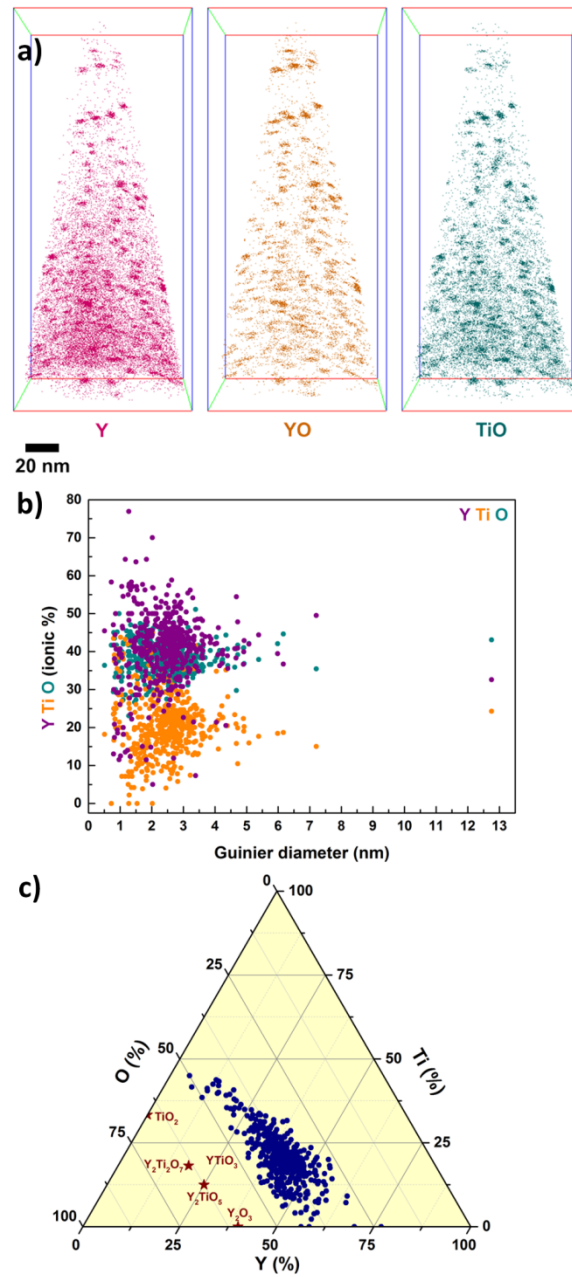


Figure 11. APT measurements for the 14YWTi 600°C sample. a) 3D-ion maps of Y, YO and TiO [Video 2]. Y, Ti and O content in the clusters, b) as a function of their size and c) as a ternary diagram.

Video 2. 3D-ion maps of Y, YO and TiO for the 14YWTi unirradiated sample.

The cluster size measured by APT is displayed in Fig. 7c; the average cluster size after the irradiation is 2.5 ± 1.0 nm for sizes in the range [0.5, 13] nm. The cluster shape is displayed in Fig. 7d and summarised in Table 2; even though most of the clusters are spherical, the amount of disc shaped clusters is double than in the unirradiated sample. The amount of rod shaped clusters has increased slightly, while the amount of lath shaped remains the same. In the cluster distance histogram shown in Fig. 8b, it is observed that the distance between nanoclusters does not change as compared to the unirradiated samples. In this case, the measured distances are in the range [1.6, 25] nm, with an average value of 9 ± 4 nm. The chemical composition of the nanoclusters can be seen in Figs. 11b and 11c and in Table 3. The number density measured by APT ranges between $(1.6 \pm 0.3) \times 10^{23} \text{ m}^{-3}$ and $(1.9 \pm 0.4) \times 10^{24} \text{ m}^{-3}$.

Irradiation-induced bubbles are visible by TEM, see Fig. 12. They can be seen as bright dots in underfocused images (Fig. 12a) and as dark dots in overfocused ones (Fig. 12c). The majority of the bubbles (presumably filled with He) have sizes <4 nm, being mostly at nanoparticle-matrix interfaces although few larger bubbles can be seen attached to larger precipitates as shown in Fig. 12. These sizes are in agreement with other investigations of high temperature irradiations of similar materials [33–35].

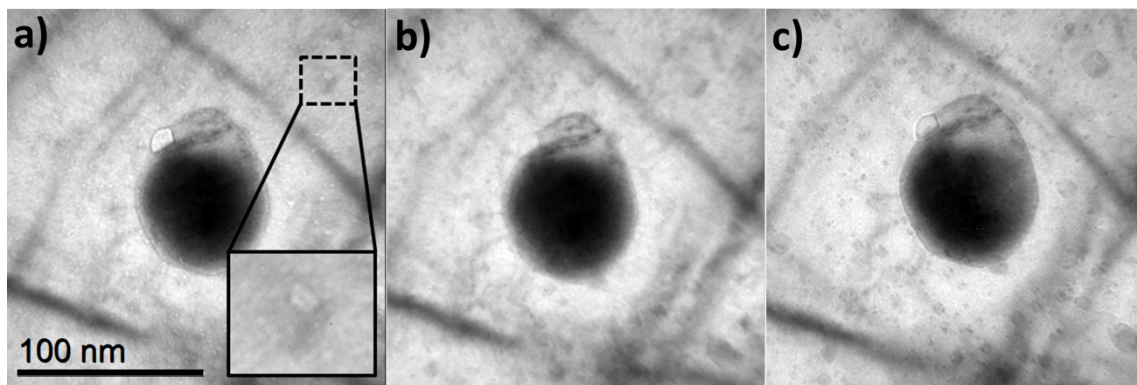


Figure 12. Through-focal series of irradiation induced bubbles in the 14YWTi 600°C alloy. a) underfocused by $1\mu\text{m}$, b) in focus and c) overfocused by $1\mu\text{m}$.

Other irradiation-induced defects could not be analysed by TEM due to the fact that the samples had been FIBed. However, previous Doppler Broadening (DB) slow PAS measurements were performed on the same ODS steels irradiated under the same conditions as a function of depth [36]. This technique allows extracting information about open volume defects (such as dislocations, vacancies, vacancy clusters...) as the DB shift of photon energies coming from e^+e^- annihilations depends on the momentum distribution of the annihilation electrons of the material [37]. The broadening can be characterized using the S-parameter, defined as the count ratio between the central area of the annihilation peak and the total peak counts. These results show that for this high temperature irradiation there is a noticeable defect annealing, see Fig. 13.

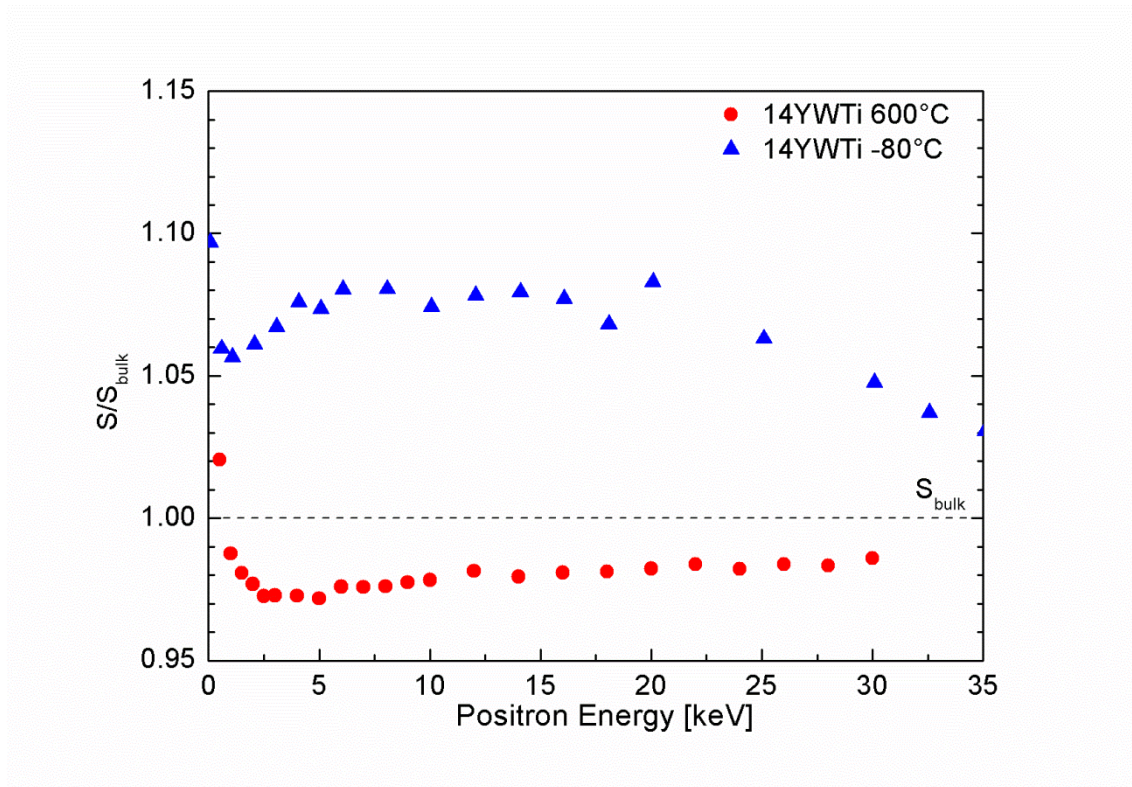


Figure 13. PAS line-shape parameter S/S_{bulk} for 14YWTi 600°C and 14YWTi -80°C with respect to positron energy.

3.3 Microstructure after single irradiation at -80°C

The microstructure of grains in the 14YWTi -80°C sample also appears to have remained unaffected by the low temperature irradiation. A series of STEM images of the nanoparticle dispersion can be seen in Fig. 14.

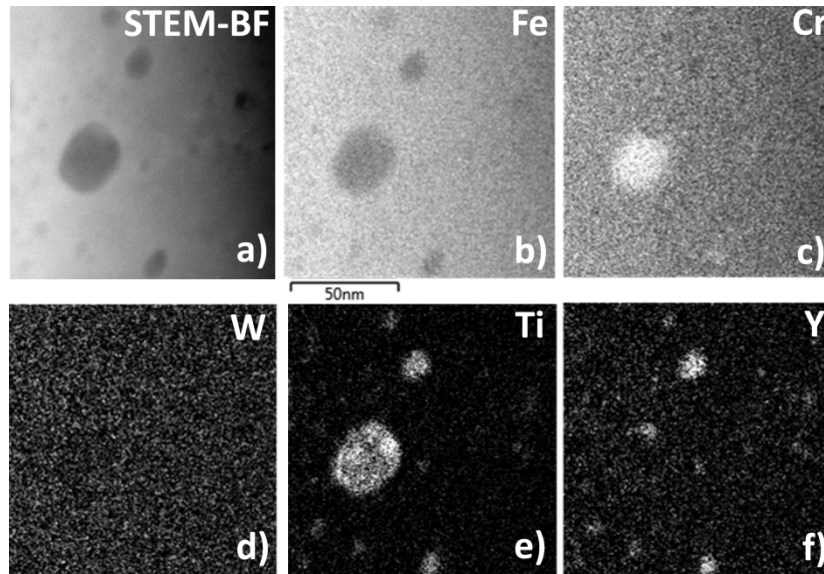


Figure 14. STEM image and EDS elemental maps of the 14YWTi- CMAM alloy. a) BF image, b) Fe K map, c) Cr K map, d) W L map, e) Ti K map, f) Y L map.

It appears that after this low temperature irradiation the morphology and chemical composition of the nanoparticles remain unaltered, being Ti-Cr rich (larger particles) or Y- Ti rich (smaller particles). The particle size distribution measured by TEM is depicted in Fig. 5c. In this case only 35 nanoparticles were visible in the available regions, therefore although the average particle size (7 ± 4 nm) appears to be similar than before irradiation, the statistics is not enough to be conclusive. For the same reason number densities were not calculated.

Fig. 15a and Video 3 depict an APT reconstruction after the low temperature irradiation. In this case, one APT dataset with a volume of 2.1×10^{-22} m³ was analysed with nanoparticle sizes ranging between 0.5 and 12 nm. The APT histogram in Fig. 7e shows that after the low temperature irradiation the average cluster size is 2.1 ± 1.0 nm. The number density of the

measured nanoclusters is $(9.2 \pm 1.8) \times 10^{23} \text{ m}^{-3}$. The cluster shape is shown in Fig. 7f and summarized in Table 2. The cluster distance histogram depicted in Fig. 8c shows a decrease in the distance between nanoclusters respect to the other two samples, with an average value of $7 \pm 3 \text{ nm}$ in a [1.8, 17] nm range. The chemical composition appears to remain unaltered, see Figs 15b and 15c and Table 3.

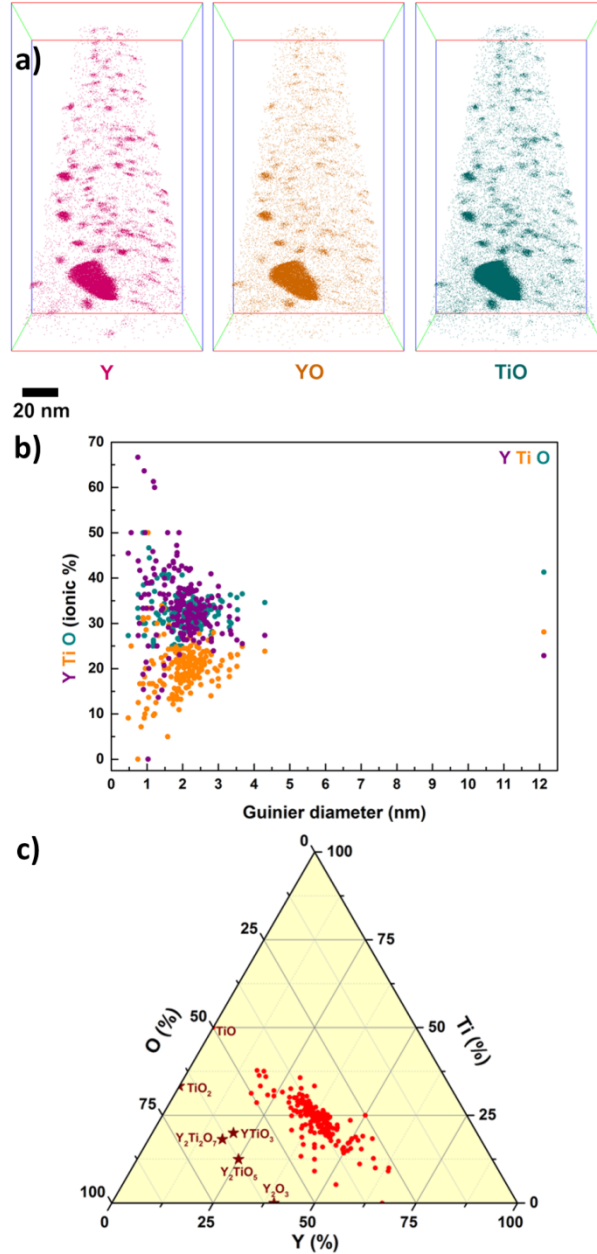


Figure 15. APT measurements for the 14YWTi -80°C sample. a) 3D-ion maps of Y, YO and TiO [Video 3]. Y, Ti and O content in the clusters b) as a function of their size and c) as a ternary diagram.

Video 3 3D-ion maps of Y, YO and TiO for the 14YWTi unirradiated sample.

Regarding defect structure, no voids are visible by TEM. However, slow PAS measurements which can detect open volume defects well below TEM resolution show that this low temperature irradiation increases their number considerably (Fig. 13) [38].

3.4 Nanoindentation

The results of the nanoindentation experiments as a function of depth are depicted in Figs. 16a (elastic modulus) and 16b (hardness). Although the ion range is different in both irradiations the results can be compared with respect to the unirradiated material. No changes in modulus data is seen for either irradiation condition. As it can be seen there are no significant differences between the hardness values obtained in the irradiated samples, as all the data lay within the standard deviation of the unirradiated sample. In any case, some subtle differences could be addressed. For sample 14YWTi 600°C the hardness values appear to be below those for the unirradiated sample for all the measured depths. Cluster distances measured by APT do not change with this irradiation (Fig. 8b). This suggests that the material could have been annealed during this irradiation, which would lead to this slight decrease of the hardness value in agreement with the slow PAS results. It seems that there is no hardening effect due to the He bubbles in agreement with previous results of a 19Cr ODS steel dual ion irradiated at 500°C [39].

For 14YWTi -80°C there appears to be a slight hardening in the region with maximum irradiation damage (Bragg peak estimated at ~ 300nm, Fig. 1b), although it is well within the experimental error of the values obtained for the unirradiated sample. These results would be consistent with both APT and slow PAS measurements. APT results show a decrease in the distance between nanoclusters (Fig. 8c) and slow PAS show an increase in the number of open volume defects (Fig.

13). All these changes would lead to an increase in hardness in agreement with other studies performed in an ODS FeCrAl alloy irradiated at room temperature [40].

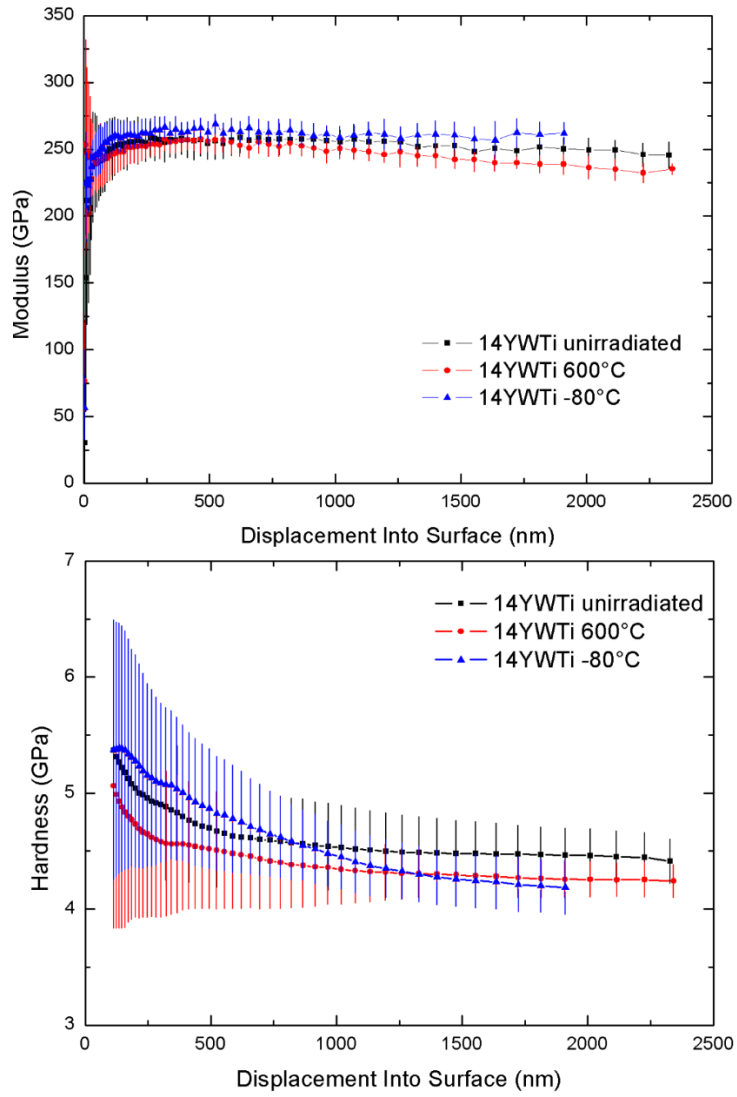


Figure 16. Nanoindentation results for 14YWTi, 14YWTi 600°C and 14YWTi -80°C: a) Elastic modulus with respect to depth and b) hardness with respect to depth.

4. Discussion

Table 4 presents a summary of the results obtained with TEM and APT in all the materials investigated. For the sample triple irradiated at 600°C, combined TEM and APT observations suggest that the irradiation does not induce any change in the composition of nanoparticles, while there are some subtle changes in their sizes and morphology. TEM nanoparticle size histograms depicted in Figs. 5a and 5b show that, for the five studied regions, there appears to be a lower amount of particles smaller than 5 nm, while there is a small increase in the overall average size suggesting some coarsening. Moreover, APT results, that focus almost solely on nanoparticles smaller than ~ 5 nm, show a slight decrease in their sizes and, in some of them, a modification of their morphologies from spherical to disc shaped. This may match the observed TEM histogram supposing that larger nanoparticles grow at the expense of the smaller ones. Furthermore, the smallest nanoclusters may now be below TEM resolution thus explaining the decrease in density measured by TEM. The fact that nanocluster distances measured by APT do not change would imply that even if the size of the smaller nanoparticles has decreased during the irradiation, they do not completely dissolve. Irradiation induced bubbles are present in the matrix with sizes smaller than 4nm. Hardness values post irradiation are slightly lower than those for the unirradiated sample which suggests that the sample could have been annealed due to the high temperature of the irradiation.

The results obtained for the samples irradiated at -80°C also show that the composition does not change significantly, while the morphology of the clusters tends to be more disc shaped. The percentages of each shape type (spherical and disk) are very similar to the 14YWTi 600°C samples, suggesting that both irradiations similarly altered the geometry of the clusters. The average nanoparticle size measured by TEM does not grow after the low temperature irradiation, contrary to what happened in the previous irradiation, while APT measurements indicate a size reduction of the smaller particles of ~27%. The decrease in average cluster size

observed by APT agrees with previously published results of low temperature (-75°C) heavy ion irradiations of a material with similar nominal composition which show that already at the irradiation damage of 5 dpa, there is a noticeable dissolution of nanoclusters [12]. In the present work the decrease in the average cluster distance measured would also suggest that for these irradiation conditions dissolution could be accompanied by nucleation of new clusters.

Sample	Technique	Morphology	Average Chemical composition (at%)	Average Size (nm)	Number density (m ⁻³)	Average cluster distance (nm)
14YWTi unirradiated	TEM	round	Y-Ti rich	8 ± 5	(1.1 ± 0.2) × 10 ²²	
	APT	72.5% spherical 20.3% disc	38±10% Y 24±6% Ti 38±6% O	2.9 ± 1.1	(3.4 ± 0.7) × 10 ²³ – (1.0 ± 0.2) × 10 ²⁴	9 ± 3
14YWTi 600°C	TEM	round	Y-Ti rich	10 ± 4	(4.8 ± 1.0) × 10 ²¹	
	APT	48.7% spherical 41.4% disc	41±9% Y 21±7% Ti 38±4% O	2.5 ± 1.0	(1.6 ± 0.3) × 10 ²³ – (1.9 ± 0.4) × 10 ²⁴	9 ± 4
14YWTi -80°C	TEM	round	Y-Ti rich	7 ± 4	N.A.	
	APT	47.0% spherical 43.4% disc	39±8% Y 24±6% Ti 38±4% O	2.1 ± 1.0	(9.2 ± 1.8) × 10 ²³	7 ± 3

Table 4. TEM and APT results of nanoparticle evolution due to both irradiations.

5. Conclusions

In this work, a Fe-14Cr-2W-0.2Ti-0.3Y₂O₃ alloy was irradiated with two different conditions. One sample of this alloy was triple ion-beam irradiated at high temperature, and another was single ion beam irradiated at low temperature. The nanoparticle evolution was analysed by TEM and APT as complementary techniques. Nanoparticles appear to remain quite stable after the two irradiations investigated. Both samples seem to have maintained their composition after the irradiations, and the effects in the nanoparticle size distribution are very weak. In any case, some changes could be observed. APT results show a slight decrease of the nanoparticle sizes below 5 nm at both temperatures while TEM histograms would suggest growth of the larger nanoparticles for the high temperature irradiation. The distance between clusters measured by APT does not change for the high temperature irradiation while their distance decreases for the low temperature one. These differences could indicate that incomplete dissolution of some of the smaller nanoparticles occurs after both irradiations, with nucleation of new particles in the case of the low temperature irradiation, and slight coarsening of existing particles after the triple-beam irradiation at high temperature. In the triple-beam irradiated sample, a dispersion of small irradiation induced bubbles is present. Nanoindentation experiments also show very little differences, pointing to some recovery in the high temperature irradiation, which would be in agreement with the microstructural changes observed.

References

- [1] O. Motojima, The ITER project construction status, Nucl. Fusion. 55 (2015) 104023.
doi:10.1088/0029-5515/55/10/104023.
- [2] D. Stork, P. Agostini, J.L. Boutard, D. Buckthorpe, E. Diegele, S.L. Dudarev, C. English, G. Federici, M.R. Gilbert, S. Gonzalez, A. Ibarra, C. Linsmeier, A. Li Puma, G. Marbach, P.F. Morris, L.W. Packer, B. Raj, M. Rieth, M.Q. Tran, D.J. Ward, S.J. Zinkle, Developing structural, high-heat flux and plasma facing materials for a near-term DEMO fusion

- power plant: The EU assessment, *J. Nucl. Mater.* 455 (2014) 277–291.
doi:10.1016/j.jnucmat.2014.06.014.
- [3] J.L. Boutard, A. Alamo, R. Lindau, M. Rieth, Fissile core and Tritium-Breeding Blanket: structural materials and their requirements, *Comptes Rendus Phys.* 9 (2008) 287–302.
doi:10.1016/j.crhy.2007.11.004.
- [4] R.L. Klueh, D.R. Harries, High-chromium ferritic and martensitic steels for nuclear applications, ASTM International, 2001.
- [5] G.R. Romanoski, L.L. Snead, R.L. Klueh, D.T. Hoelzer, Development of an oxide dispersion strengthened, reduced-activation steel for fusion energy, *J. Nucl. Mater.* 283–287 (2000) 642–646. doi:10.1016/S0022-3115(00)00137-9.
- [6] G.R. Odette, M.J. Alinger, B.D. Wirth, Recent Developments in Irradiation-Resistant Steels, *Annu. Rev. Mater. Res.* 38 (2008) 471–503.
doi:10.1146/annurev.matsci.38.060407.130315.
- [7] R. Schäublin, A. Ramar, N. Baluc, V. de Castro, M.A. Monge, T. Leguey, N. Schmid, C. Bonjour, Microstructural development under irradiation in European ODS ferritic/martensitic steels, *J. Nucl. Mater.* 351 (2006) 247–260.
doi:10.1016/j.jnucmat.2006.02.005.
- [8] S.J. Zinkle, L.L. Snead, Designing Radiation Resistance in Materials for Fusion Energy, *Annu. Rev. Mater. Res.* 44 (2014) 241–67. doi:10.1146/annurev-matsci-070813-113627.
- [9] S. Ukai, M. Fujiwara, Perspective of ODS alloys application in nuclear environments, *J. Nucl. Mater.* 307–311 (2002) 749–757. doi:10.1016/S0022-3115(02)01043-7.
- [10] M.L. Lescoat, J. Ribis, A. Gentils, O. Kaïtasov, Y. De Carlan, A. Legris, In situ TEM study of the stability of nano-oxides in ODS steels under ion-irradiation, *J. Nucl. Mater.* 428 (2012) 176–182. doi:10.1016/j.jnucmat.2011.12.009.
- [11] M.L. Lescoat, J. Ribis, Y. Chen, E.A. Marquis, E. Bordas, P. Trocellier, Y. Serruys, A. Gentils, O. Kaïtasov, Y. De Carlan, A. Legris, Radiation-induced Ostwald ripening in oxide

- dispersion strengthened ferritic steels irradiated at high ion dose, *Acta Mater.* 78 (2014) 328–340. doi:10.1016/j.actamat.2014.06.060.
- [12] A. Certain, S. Kuchibhatla, V. Shutthanandan, D.T. Hoelzer, T.R. Allen, Radiation stability of nanoclusters in nano-structured oxide dispersion strengthened (ODS) steels, *J. Nucl. Mater.* 434 (2013) 311–321. doi:10.1016/j.jnucmat.2012.11.021.
- [13] J.P. Wharry, M.J. Swenson, K.H. Yano, A review of the irradiation evolution of dispersed oxide nanoparticles in the b.c.c. Fe-Cr system: Current understanding and future directions, *J. Nucl. Mater.* 486 (2017) 11–20. doi:10.1016/j.jnucmat.2017.01.009.
- [14] M. a. Auger, V. de Castro, T. Leguey, M. a. Monge, a. Muñoz, R. Pareja, Microstructure and tensile properties of oxide dispersion strengthened Fe–14Cr–0.3Y₂O₃ and Fe–14Cr–2W–0.3Ti–0.3Y₂O₃, *J. Nucl. Mater.* 442 (2013) S142–S147. doi:10.1016/j.jnucmat.2012.11.001.
- [15] Y. Serruys, P. Trocellier, S. Miro, E. Bordas, M.O. Ruault, O. Kaïtasov, S. Henry, O. Leseigneur, T. Bonnaillie, S. Pellegrino, S. Vaubaillon, D. Uriot, JANNUS: A multi-irradiation platform for experimental validation at the scale of the atomistic modelling, *J. Nucl. Mater.* 386–388 (2009) 967–970. doi:10.1016/j.jnucmat.2008.12.262.
- [16] S. Pellegrino, P. Trocellier, S. Miro, Y. Serruys, É. Bordas, H. Martin, N. Chaâbane, S. Vaubaillon, J.P. Gallien, L. Beck, The JANNUS Saclay facility: A new platform for materials irradiation, implantation and ion beam analysis, *Nucl. Instruments Methods Phys. Res. Sect. B Beam Interact. with Mater. Atoms.* 273 (2012) 213–217. doi:10.1016/j.nimb.2011.07.078.
- [17] P. Trocellier, S. Miro, Y. Serruys, S. Vaubaillon, S. Pellegrino, S. Agarwal, S. Moll, L. Beck, Study of helium migration in nuclear materials at Jannus-Saclay, *Nucl. Instruments Methods Phys. Res. Sect. B Beam Interact. with Mater. Atoms.* 331 (2014) 55–64. doi:10.1016/j.nimb.2014.01.027.
- [18] J.P. Biersack, J.F. Ziegler, *The Stopping and Range of Ions in Solids*, Pergamon, New

- York, 1982. doi:10.1007/978-3-642-68779-2_5.
- [19] M. Šćepanović, V. de Castro, T. Leguey, M.A. Auger, S. Lozano-Perez, R. Pareja, Microstructural stability of ODS Fe-14Cr (-2W-0.3Ti) steels after simultaneous triple irradiation, *Nucl. Mater. Energy*. 9 (2016) 490–495. doi:10.1016/j.nme.2016.08.001.
 - [20] A. Climent-Font, F. Pászti, G. García, M.T. Fernández-Jiménez, F. Agulló, First measurements with the Madrid 5 MV tandem accelerator, *Nucl. Instruments Methods Phys. Res. Sect. B Beam Interact. with Mater. Atoms*. 219–220 (2004) 400–404. doi:10.1016/j.nimb.2004.01.090.
 - [21] F.J. Sánchez, I. García-Cortés, J.F. Marco, D. Jiménez-Rey, A. Maira, J. Castellanos, R. Vila, Á. Ibarra, Influence of an external magnetic field on damage by self-ion irradiation in Fe 90 Cr 10 alloy, *Nucl. Mater. Energy*. 9 (2016) 476–479. doi:10.1016/j.nme.2016.05.010.
 - [22] D.B. Williams, C.C. Barry, *Transmission Electron Microscopy*, Springer US, 2009. doi:10.1007/978-0-387-76501-3.
 - [23] B. Gault, M.P. Moody, J.M. Cairney, S.P. Ringer, *Atom Probe Microscopy*, Springer-Verlag New York, 2012. doi:10.1007/978-1-4614-3436-8.
 - [24] M.K. Miller, K.F. Russell, K. Thompson, R. Alvis, D.J. Larson, Review of atom probe FIB-based specimen preparation methods, *Microsc. Microanal.* 13 (2007) 428–436. doi:10.1017/S1431927607070845.
 - [25] J.M. Hyde, E.A. Marquis, K.B. Wilford, T.J. Williams, A sensitivity analysis of the maximum separation method for the characterisation of solute clusters, *Ultramicroscopy*. 111 (2011) 440–447. doi:10.1016/j.ultramic.2010.12.015.
 - [26] M.K. Miller, E.A. Kenik, *Atom Probe Tomography : A Technique for Nanoscale Characterization*, *Microsc. Microanal.* (2004) 336–341. doi:10.1017/S1431927604040577.
 - [27] R.K.W. Marceau, L.T. Stephenson, C.R. Hutchinson, S.P. Ringer, Quantitative atom

- probe analysis of nanostructure containing clusters and precipitates with multiple length scales, *Ultramicroscopy*. 111 (2011) 738–742.
doi:10.1016/j.ultramic.2010.12.029.
- [28] P. Hosemann, C. Vieh, R.R. Greco, S. Kabra, J.A. Valdez, M.J. Cappiello, S.A. Maloy, Nanoindentation on ion irradiated steels, *J. Nucl. Mater.* 389 (2009) 239–247.
doi:10.1016/j.jnucmat.2009.02.026.
- [29] C. Heintze, F. Bergner, M. Hernandez-Mayoral, Ion-irradiation-induced damage in Fe-Cr alloys characterized by nanoindentation, *J. Nucl. Mater.* 417 (2011) 980–983.
doi:10.1016/j.jnucmat.2010.12.196.
- [30] W.C. Oliver, G.M. Pharr, Measurement of hardness and elastic modulus by instrumented indentation: Advances in understanding and refinements to methodology, *J. Mater. Res.* 19 (2004) 3–20. doi:10.1557/jmr.2004.19.1.3.
- [31] M.A. Auger, V. de Castro, T. Leguey, S. Lozano-Perez, P.A.J. Bagot, M.P. Moody, S.G. Roberts, Effect of the milling atmosphere on the microstructure and mechanical properties of a ODS Fe-14Cr model alloy, *Mater. Sci. Eng. A*. 671 (2016) 264–274.
doi:10.1016/j.msea.2016.06.054.
- [32] M.C. Brandes, L. Kovarik, M.K. Miller, M.J. Mills, Morphology, structure, and chemistry of nanoclusters in a mechanically alloyed nanostructured ferritic steel, *J. Mater. Sci.* 47 (2012) 3913–3923. doi:10.1007/s10853-012-6249-x.
- [33] T. Tanaka, K. Oka, S. Ohnuki, S. Yamashita, T. Suda, S. Watanabe, E. Wakai, Synergistic effect of helium and hydrogen for defect evolution under multi-ion irradiation of Fe-Cr ferritic alloys, *J. Nucl. Mater.* 329–333 (2004) 294–298.
doi:10.1016/j.jnucmat.2004.04.051.
- [34] P.D. Edmondson, C.M. Parish, Y. Zhang, A. Hallén, M.K. Miller, Helium bubble distributions in a nanostructured ferritic alloy, *J. Nucl. Mater.* 434 (2013) 210–216.
doi:10.1016/j.jnucmat.2012.11.049.

- [35] I.-S. Kim, J.D. Hunn, N. Hashimoto, D.L. Larson, P.J. Maziasz, K. Miyahara, E.H. Lee, Defect and void evolution in oxide dispersion strengthened ferritic steels under 3.2 MeV Fe⁺ ion irradiation with simultaneous helium injection, *J. Nucl. Mater.* 280 (2000) 264–274. doi:10.1016/S0022-3115(00)00066-0.
- [36] P. Parente, T. Leguey, V. De Castro, T. Gigl, M. Reiner, C. Hugenschmidt, R. Pareja, Characterization of ion-irradiated ODS Fe-Cr alloys by doppler broadening spectroscopy using a positron beam, *J. Nucl. Mater.* 464 (2015) 140–146. doi:10.1016/j.jnucmat.2015.04.033.
- [37] M.J. Puska, R.M. Nieminen, The Theory of Positrons in solids and on solid surfaces, *Rev. Mod. Physics*,. 66 (1994) 749–759.
- [38] W. Anwand, T. Leguey, M. Scepanovic, F.J. Sanchez, I. García-Cortés, A. Wagner, Fe⁺ Implantation Induced Damage in Oxide Dispersion Strengthened Steels Investigated by Doppler Broadening Spectroscopy, *Defect Diffus. Forum.* 373 (2017) 113–116. doi:10.4028/www.scientific.net/DDF.373.113.
- [39] H. Kishimoto, K. Yutani, R. Kasada, A. Kimura, Helium cavity formation research on oxide dispersed strengthening (ODS) ferritic steels utilizing dual-ion irradiation facility, *Fusion Eng. Des.* 81 (2006) 1045–1049. doi:10.1016/j.fusengdes.2005.09.049.
- [40] R. Kögler, W. Anwand, A. Richter, M. Butterling, X. Ou, A. Wagner, C.L. Chen, Nanocavity formation and hardness increase by dual ion beam irradiation of oxide dispersion strengthened FeCrAl alloy, *J. Nucl. Mater.* 427 (2012) 133–139. doi:10.1016/j.jnucmat.2012.04.029.

- Nanoparticles stable after high temperature triple-beam and low temperature single-beam irradiation.
- Samples appear to have maintained the composition after both irradiations.
- Slight decrease of the nanoparticle sizes below 5nm after both irradiations.
- There appears to be incomplete dissolution of smaller nanoparticles after both irradiations.

Title: CHARACTERISATION OF ODS Fe-14Cr-2W-0.3Ti BEFORE AND AFTER HIGH TEMPERATURE TRIPLE AND LOW TEMPERATURE SINGLE ION IRRADIATIONS

M. Šćepanović^{1*}, T. Leguey¹, M. A. Auger², S. Lozano-Perez², D.E.J. Armstrong², I. García-Cortés³, V. de Castro¹

¹*Departamento de Física. Universidad Carlos III de Madrid. 28911-Leganés, Spain*

²*Department of Materials. University of Oxford. OX1 3PH, Oxford, UK*

³*Laboratorio Nacional de Fusión, CIEMAT, Avda. de la Complutense 40, 28040, Madrid, Spain*

Corresponding Author:

Maša Šćepanović,

Department of Physics,

Universidad Carlos III de Madrid

Avda. de la Universidad 30

28911 Leganes Madrid, Spain

Email: mscepano@fis.uc3m.es

Abstract

Oxide dispersion strengthened reduced activation ferritic steels are being considered as structural materials for future fusion reactors and Gen IV fission reactors. In this work, the stability of the nanometric oxides after being irradiated at different conditions and temperatures has been investigated. A Fe-14Cr-2W-0.3Ti-0.3Y₂O₃ alloy was simultaneously triple-beam irradiated at 600°C with Fe, He and H ions. The same alloy was irradiated with Fe ions at -80°C. The microstructure of this alloy was investigated using Transmission Electron Microscopy, Atom Probe Tomography and nanoindentation before and after the irradiations. There were no significant changes in the morphology and chemical composition of the nanoparticles after the irradiations, although the size of the smaller ones tends to decrease for both irradiation conditions. Small irradiation-induced bubbles were present after the triple simultaneous irradiation at high temperature.

Nanoindentation also shows no significant differences with a slight increase in hardness for the sample irradiated at low temperature, while softening appears in the high temperature irradiation.

Acknowledgements: This investigation was supported by the Ministerio de Economía y Competitividad (project ENE2015-70300-C3-2-R), the Comunidad de Madrid through the program TECHNOFUSION-II (S2013/MAE-2745), the UK Engineering and Physical Sciences Research Council (EPSRC) (Refs: EP/H018921/1 and EP/M022803/1) and the European Union Seventh Framework Programme under Grant Agreement 312483 - ESTEEM2 (Integrated Infrastructure Initiative – I3). The authors acknowledge the JANNuS-Saclay and the CMAM team for their scientific and technological advice. DEJA acknowledges support through a Royal Academy of Engineering Research Fellowship. MA acknowledges Dr A.J. London for providing MatLab codes.

Conflict of interest statement: The authors declare no conflicts of interest for this article.

CHARACTERISATION OF ODS Fe-14Cr-2W-0.3Ti BEFORE AND AFTER HIGH TEMPERATURE TRIPLE AND LOW TEMPERATURE SINGLE ION IRRADIATIONS

Abstract

Oxide dispersion strengthened reduced activation ferritic steels are being considered as structural materials for future fusion reactors and Gen IV fission reactors. In this work, the stability of the nanometric oxides after being irradiated at different conditions and temperatures has been investigated. A Fe-14Cr-2W-0.3Ti-0.3Y₂O₃ alloy was simultaneously triple-beam irradiated at 600°C with Fe, He and H ions. The same alloy was irradiated with Fe ions at -80°C. The microstructure of this alloy was investigated using Transmission Electron Microscopy, Atom Probe Tomography and nanoindentation before and after the irradiations. There were no significant changes in the morphology and chemical composition of the nanoparticles after the irradiations, although the size of the smaller ones tends to decrease for both irradiation conditions. Small irradiation-induced bubbles were present after the triple simultaneous irradiation at high temperature. Nanoindentation also shows no significant differences with a slight increase in hardness for the sample irradiated at low temperature, while softening appears in the high temperature irradiation.

Keywords: Oxide Dispersion Strengthened steels, ion irradiation, Transmission Electron Microscopy, nanoindentation, Atom Probe Tomography, nanoparticles.

1. Introduction

In the face of depleting sources of fossil fuels, nuclear fusion is regarded as one of the most promising, low carbon, solutions. At this moment, the International Thermonuclear Experimental Reactor (ITER) is being built [1], after which a Demonstration power plant (DEMO) is planned as the next step towards commercial fusion reactors [2]. One of the biggest challenges is the development of the materials that are to be used in these reactors, especially at high temperatures. Oxide dispersion strengthened (ODS) Fe-Cr alloys are being considered as candidate materials for structural applications. They are envisaged to be used in the first wall of advanced nuclear fusion reactors and as fuel cladding in some GEN IV fission designs, therefore they will have to sustain high doses, as a consequence of the 14 MeV neutron irradiation, operating temperatures up to 700°C, and large amounts of He produced by transmutation reactions [3,4]. It has been shown that a fine dispersion of nanoparticles homogeneously distributed in the matrix of these materials improves their mechanical performance by impeding dislocation motion, raising operating temperatures while also enhancing creep strength [5,6].

The nano-sized yttria particles are chosen for their superior thermodynamic stability, compared to nitrides and carbides, and because they act as sinks for irradiation induced defects [7,8]. ODS materials are usually produced by powder metallurgy involving mechanical alloying (MA) and consolidation by hot isostatic pressing (HIP) or hot extrusion after which they undergo thermomechanical treatments in order to further enhance their mechanical properties [6,9].

Due to the lack of neutron irradiation facilities operating in the fusion energy regime, to simulate the effect of the severe irradiation conditions in the nuclear fusion reactor, materials are usually self-ion irradiated. Moreover, as production of transmutation gasses (He and H) plays a significant role in the evolution of the microstructure, materials can be also irradiated with high doses of He and/or H.

Studies of the ion irradiation induced evolution of nanoparticles in ferritic ODS steels have been inconclusive to date. In the case of 18CrODS irradiated at 500°C with Fe^+ ions, nanoparticles are stable at doses ranging from 4 to 45 dpa [10] while for high doses (150 dpa) the sizes of nanoparticles increase while the number density decreases [11]. For 14YWT irradiated with Ni^{2+} ions at 600°C and irradiation doses ranging from 5 to 100 dpa, with Atom Probe Tomography (APT) it has been observed that nanoparticle sizes and their number densities remained stable, while both values increase when investigated using Energy Filtered Transmission Electron Microscopy (EFTEM) [12]. Wharry et al have recently summarized available experimental studies on nanoparticle evolution under irradiation in ODS steels showing the complexity to fully understand the evolution and mechanisms present [13]. Moreover, comparing irradiations across different batches of materials is difficult due to differing initial chemical compositions, processing conditions and thermomechanical histories. Thus, it is important to investigate materials, from the same batch, irradiated under different conditions using complementary techniques in order to describe the evolution of nanoparticles on different scales, together with any changes in the microstructure and mechanical properties.

In this work, the effects of two different ion irradiations on an ODS Fe-14Cr-2W-0.3Ti steel were investigated. The alloy was simultaneously irradiated with Fe^{5+} , He^+ and H^+ ions at 600°C, or single irradiated with Fe^{5+} ions at -80°C. The microstructure before and after the irradiations was investigated with advanced techniques such as Transmission Electron Microscopy (TEM) and APT and compared with previous positron annihilation spectroscopy (PAS) results. The evolution of the nanoparticles was analysed in terms of their size, shape and chemical composition. Nanoindentation was used to examine possible changes in the hardness of both irradiated samples with respect to the unirradiated one.

2. Experimental

2.1. Material

The nominal composition of the material investigated in this work is Fe-14Cr-2W-0.3Ti-0.3Y₂O₃ (wt%) which, in unirradiated state, will be referred to as 14YWTi. The alloy was produced by adding Y₂O₃ nanoparticles to a high purity elemental powder, mechanically alloyed under H₂ atmosphere and consolidated by hot isostatic pressing (HIP) at 1100 °C and 200 MPa for 2 h. After consolidation, the alloy billets were forged at ~ 1150 °C and subsequently heat treated at 850°C for 2 h. The detailed fabrication procedure can be found in [14]. Samples with dimensions 7×7×0.2 mm³ were mechanically polished with SiC polishing pads and then mirror polished with 50 nm alumina slurry.

2.2 Irradiation conditions

Two irradiations were carried out as detailed below.

2.2.1 JANNuS-Saclay facility

The simultaneous triple-ion irradiation with Fe⁵⁺, He⁺ and H⁺ ions was performed at the JANNuS-Saclay facility in France [15–17]. The samples were irradiated at 600 °C to 30 dpa with Fe⁵⁺, 1500 appm H⁺ and 600 appm He⁺ to simulate fusion relevant conditions. The energies were 14 MeV for Fe⁵⁺, 1.6 MeV for He⁺ and 500 keV for H⁺ and were specifically chosen to achieve the maximum damage (Bragg peak) at the same depth for all ions, see Fig. 1a displaying the SRIM profile for the irradiation. In this case, the Bragg peak is estimated at ~ 2.4 μm from SRIM calculations and limited by the minimum feasible implantation energy of the H⁺ ions (500 keV) [18]. More details about this irradiation can be found in [19]. This sample will be referred to as 14YWTi 600°C.

2.2.2 CMAM facility

A sample of the same material was irradiated at the Centre for Micro Analysis of Materials (CMAM) in Madrid, Spain with a low temperature setup [20,21]. This irradiation was carried out with 1 MeV Fe^+ ions up to a damage of 15 dpa at a temperature of -80°C to avoid possible temperature-related recovery of defects. In this sample, the Bragg peak was estimated at ~ 300 nm from the sample surface, see Fig. 1b. This sample will be referred to as 14YWTi -80°C .

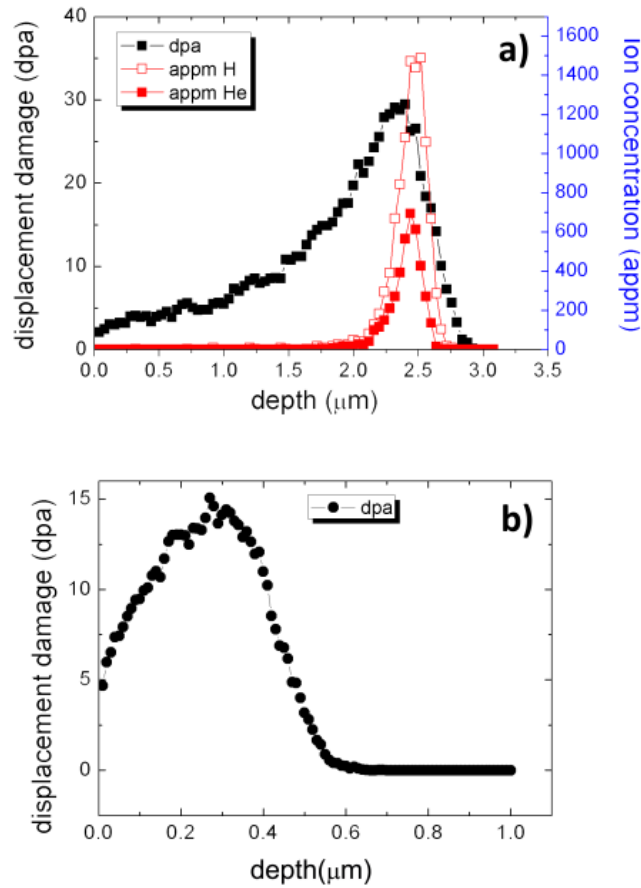


Figure 1. SRIM profiles for a) JANNuS irradiation (He^+ and H^+ ions implantation profile and Fe^{5+} ions damage profile) and b) CMAM irradiation (Fe^+ ions damage profile).

Table 1 shows the relevant parameters (ions, energy, temperature, dose rate and fluence) for the two irradiation conditions.

Irradiation facility	Ion type	Energy	Temp (°C)	Dose rate (ions·cm ⁻² s ⁻¹)	Fluence (ions·cm ⁻²)	Maximum dose (dpa) / concentration (appm)
JANNUS	Fe ⁵⁺	14 MeV	600	8.3×10^{11}	1.49×10^{16}	~30 dpa
	He ⁺	1.6 MeV		8×10^{10}	1.4×10^{15}	~600 appm
	H ⁺	500 keV		1.97×10^{11}	3.55×10^{15}	~1500 appm
CMAM	Fe ⁺	1 MeV	-80	1.35×10^{12}	6.5×10^{15}	~15 dpa

Table 1. Irradiation conditions

2.3 Transmission Electron Microscopy (TEM)

The unirradiated samples were electropolished in a TENUPO 5 twin jet polisher using a solution of 5 vol % perchloric acid in methanol. Irradiated samples for TEM analyses were prepared in a Zeiss AURIGA 40 focused ion beam (FIB) instrument fitted with a scanning electron microscope (SEM). A Ga²⁺ beam was used to mill the trenches, in the site previously covered by a layer of Pt, thus obtaining a cantilever. It was subsequently lifted out, attached to a TEM grid and further milled until electron transparency was reached. The detailed process of this in-situ lift-out method is described in [19]. The investigated FIBed samples are presented in Fig. 2a (14YWTi 600°C) and Fig. 2b (14YWTi -80°C). The original surface location is marked by the remaining Pt at the sides of the lift out sample.

Imaging was done in areas nearby the calculated Bragg peaks, where the maximum damage was achieved. The chemical information was obtained by Scanning Transmission Electron Microscopy- Energy Dispersive Spectroscopy (STEM-EDS) and Energy Filtered Transmission Electron Microscopy (EFTEM) using a JEOL 2200MCO microscope operating at 200 kV beam energy equipped with an Ω -filter and an Oxford Instruments EDS detector. EFTEM elemental maps were extracted using the multiple linear least square (MLLS) method with reference spectra for each element [22].

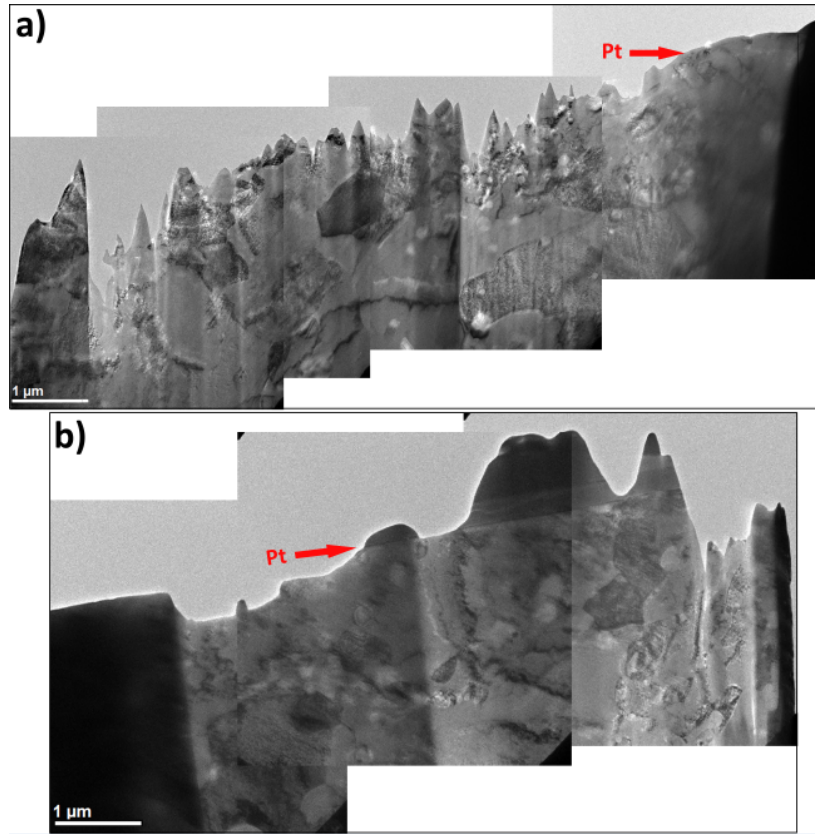


Figure 2. TEM images of FIBed samples of a) 14YWTi 600°C and b) 14YWTi -80°C. The arrows show the position of the remaining platinum layer.

2.4 Atom Probe Tomography (APT)

The unirradiated samples were prepared for APT by standard electropolishing methods [23]. Rod-shaped samples of the material ($0.5 \times 0.5 \times 20 \text{ mm}^3$) were repeatedly dipped into a solution (25 vol% perchloric acid, 75 vol% acetic acid) applying a DC voltage of 15 V, which was later reduced to 10 V as the specimen area was reduced, until the necked region split the sample into 2 parts. These parts were then micropolished with the specimen repeatedly pushed through a gold loop containing a drop of electrolyte (2 vol% perchloric acid, 98 vol% 2-butoxyethanol) with DC voltage going from 8 to 5 V until specimens with the suitable shape for APT (needle shaped with a final tip radius below 100 nm) were obtained. The irradiated samples were prepared by the FIB lift-out method using Zeiss Auriga FIB/SEM and Zeiss NVision 40 FIB/SEM instruments [24].

14YWTi and 14YWTi 600°C samples were run in a CAMECA LEAP3000™ in laser mode ($\lambda=532$ nm), using a laser energy of 0.40 nJ at 200 kHz repetition rate. 14YWTi -80°C sample was run in a CAMECA LEAP5000™ in laser mode ($\lambda= 355$ nm), using a laser energy of 0.040 nJ at 200 kHz repetition rate. The sample temperature was kept at 50K in all the measurements.

For data reconstruction and analysis, the CAMECA IVAS software package and MATLAB software were used. Nanoclusters were identified by using the maximum separation method, which requires two parameters, namely d_{\max} (maximum distance between ions) and N_{\min} (minimum number of ions for a cluster to be non-random) [25]. The cluster size was defined as the Guinier diameter, i.e. twice the Guinier radius [26]. The shape of the clusters was defined in terms of the best-fit ellipsoids. The smallest, middle and largest characteristic lengths of each best-fit ellipsoid enclosing each identified cluster were used to calculate their oblateness (smallest characteristic length/middle characteristic length) and the aspect ratio (middle characteristic length/largest characteristic length). Combination of oblateness and aspect ratio values can be used to define the cluster shape as sphere, rod, lath or disc [27]. The distance between one cluster and its nearest neighbour was calculated as the distance between their centres of mass [26].

2.5 Nanoindentation

Nanoindentation is widely used technique to obtain depth-dependent properties of thin irradiated layers [28,29]. It measures the hardness and elastic modulus of a material from indentation load-displacement data obtained during one cycle of loading and unloading [30]. In this work, continuous stiffness measurements (CSM) were performed with a MTS NanoXP indenter using a Berkovich tip with a maximum indentation displacement of 3 μm for the unirradiated and the JANNuS irradiated samples, and 2 μm for the CMAM irradiated sample. That displacement was the target depth, chosen to encompass layers with maximum irradiation

damage (Bragg peak) in both irradiated samples. All of the samples were indented with an array of 6x6 indents and average hardness and modulus –depth curves plotted.

3. Results

3.1 Microstructure before irradiation

Previous TEM analyses of the unirradiated alloy show a duplex grain structure and the presence of different secondary phases, such as Ti-Cr rich particles with round morphology and sizes ranging from 50 nm to 500 nm as well as Y-Ti rich round nanoparticles with sizes mostly below 30 nm [14]. EDS and EFTEM maps of these Ti-Cr and Y-Ti rich particles are shown in Figs. 3 and 4. The Y-Ti rich nanoparticles, with mean size of 8 ± 5 nm, are found to be quite uniformly dispersed throughout the matrix. Some of them were identified as Y_2TiO_5 oxides, as reported in [14]. The nanoparticle size distribution is presented in the histogram shown in Fig. 5a. The number density of 13 measured regions containing Y-Ti rich nanoparticles and having volumes of the order of 10^{-21} m^3 varies between $(1.2 \pm 0.2) \times 10^{21} \text{ m}^{-3}$ and $(3.8 \pm 0.8) \times 10^{22} \text{ m}^{-3}$ with an average value of $(1.1 \pm 0.2) \times 10^{22} \text{ m}^{-3}$.

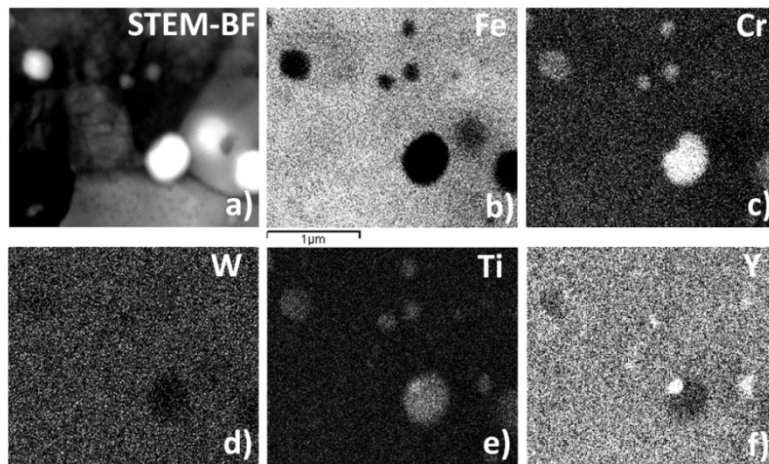


Figure 3. STEM image and EDS elemental maps of the 14YWTi unirradiated alloy. a) BF image, b) Fe K map, c) Cr K map, d) W L map, e) Ti K map, f) Y (K+L) map.

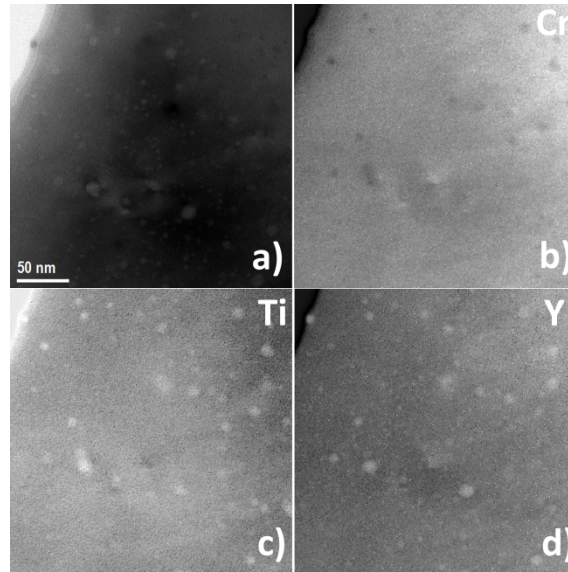


Figure 4. EFTEM elemental maps of the unirradiated 14YWTi alloy showing the morphology and chemical composition of Y-rich nanoparticles a) elastic image, b) Cr M2,3 map, c) Ti M2,3 map, d) Y N2,3 map.

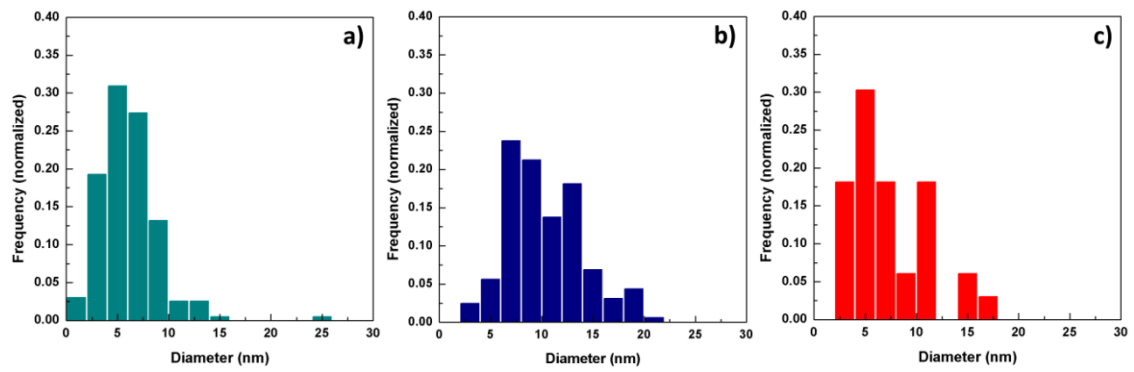


Figure 5. Histograms showing the nanoparticle size distribution for a) unirradiated 14YWTi, b) 14YWTi 600°C and c) 14YWTi -80°C.

In agreement with TEM observations, by APT it was possible to observe Y-Ti-O rich nanoclusters, according to the 3D ion maps displayed in Fig. 6a and Video 1.

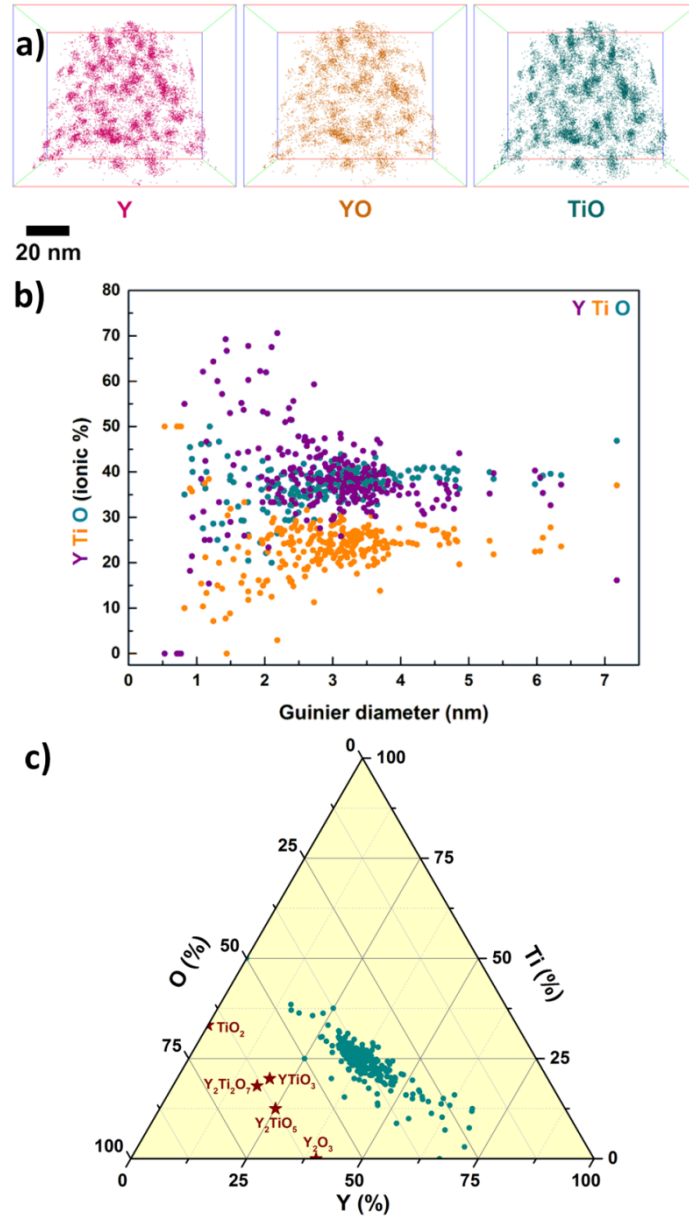


Figure 6. APT measurements for 14YWTi unirradiated. a) 3D-ion maps of Y, YO and TiO [Video 1] Y, Ti and O content in the clusters, b) as a function of their size and c) as a ternary diagram.

Video 1. 3D-ion maps of Y, YO and TiO for 14YWTi unirradiated.

The cluster size distribution obtained from APT reconstructions is shown in Fig. 7a. Sizes were in the range 0.5 to 7 nm with mean size 2.9 ± 1.1 nm. The number densities of measured nanoclusters in two regions with volumes of 2.2 and $1.8 \times 10^{-22} \text{ m}^3$ are $(3.4 \pm 0.7) \times 10^{23} \text{ m}^{-3}$ and $(1.0 \pm 0.2) \times 10^{24} \text{ m}^{-3}$. The shape of the clusters is summarized in Fig. 7b and in Table 2; most of them being spherical. A histogram for the distance between nearest clusters is shown in Fig. 8a. The measured distances are in the range $[2.5, 27]$ nm, with an average value of 9 ± 3 nm.

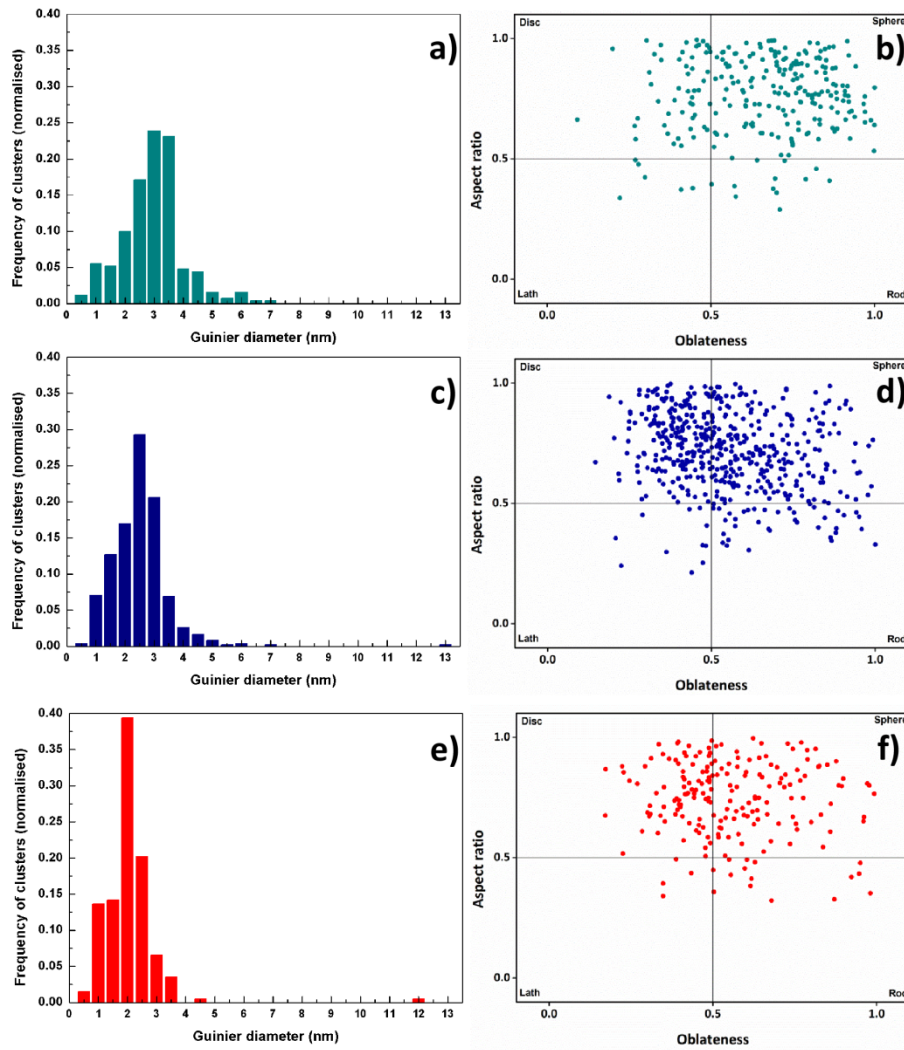


Figure 7. APT cluster size distribution histograms for a) 14YWTi unirradiated, c) 14YWTi 600°C and e) 14YWTi -80°C and cluster shape distribution for b) 14YWTi unirradiated, d) 14YWTi 600°C and f) 14YWTi -80°C.

Sample	Sphere	Disc	Rod	Lath
14YWTi unirradiated	72.5%	20.32%	4.78%	2.4%
14YWTi 600°C	48.69%	41.41%	7.68%	2.22%
14YWTi -80°C	46.97%	43.43%	7.57%	2.02%

Table 2. APT cluster shape quantification for all samples

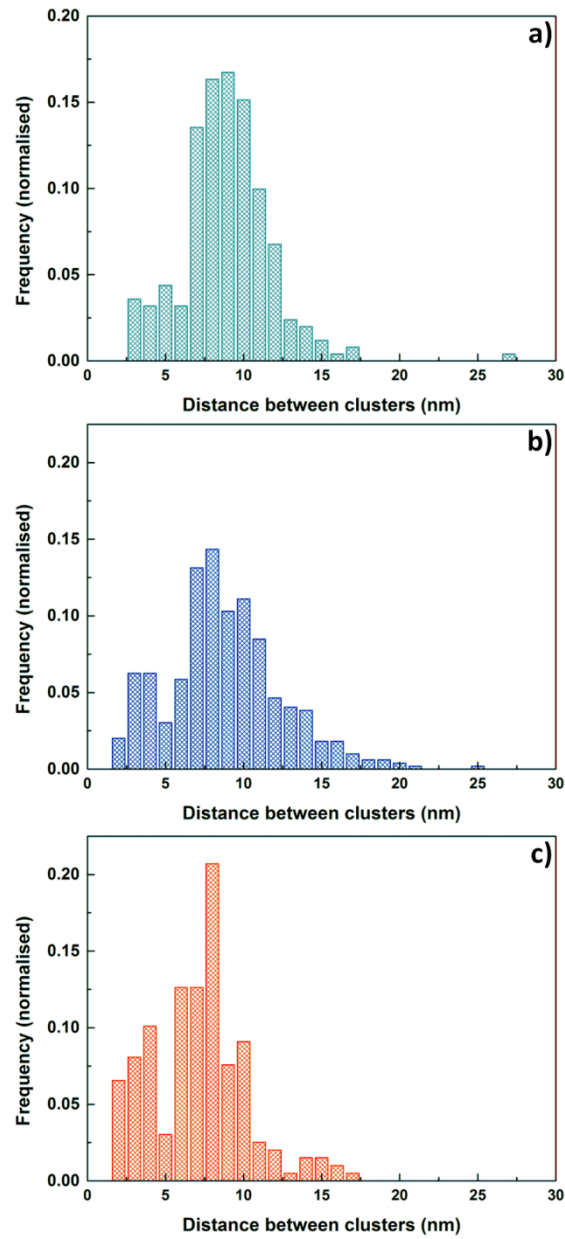


Figure 8. APT distance between clusters for a) 14YWTi unirradiated, b) 14YWTi 600°C and c) 14YWTi -80°C.

The chemical composition of the nanoclusters, i.e. their Y, Ti and O content, is displayed in Fig. 6b as a function of the cluster size and in Fig. 6c as a ternary diagram. The substoichiometry of the smaller nanoparticles (< 4 nm) in a ODS Fe-14Cr model alloy has been observed by the authors in [31] and by Brandes et al. in a similar ODS ferritic steel [32]. The chemical composition of the measured clusters is summarized in Table 3.

The variations in the mean size and number densities of nanoparticles between TEM and APT can be attributed to the different resolutions, sensitivities and volumes measured with the two techniques.

Sample	Y (at. %)	Ti (at. %)	O (at. %)
14YWTi unirradiated	38±10	24±6	38±6
14YWTi 600°C	41±9	21±7	38 ± 4
14YWTi -80°C	39±8	24 ± 6	38±4

Table 3. APT chemical composition of nanoclusters for all samples (averaged values)

3.2 Microstructure after triple irradiation at 600°C

For 14YWTi 600°C, previous TEM analyses show that there are no changes in the grain structure of the alloy [19]. Figs. 9 and 10 depict the distribution of nanoparticles in the irradiated alloy. As for the unirradiated alloy, they have round morphologies and are Ti-Cr or Y- Ti rich. Their size distribution is shown in Fig. 5b, with an average nanoparticle size of 10 ± 4 nm. Number densities of particles measured in five regions with volumes of the order of 10^{-21} m^3 vary between $(3.5 \pm 0.7) \times 10^{21} \text{ m}^{-3}$ and $(6.9 \pm 1.4) \times 10^{21} \text{ m}^{-3}$ with an average value of $(4.8 \pm 1.0) \times 10^{21} \text{ m}^{-3}$ [19]. In

any case, it must be taken into account that the number of nanoparticles measured in this case was much lower, i.e. 150 vs 700 due to the lower number of regions available to be analysed.

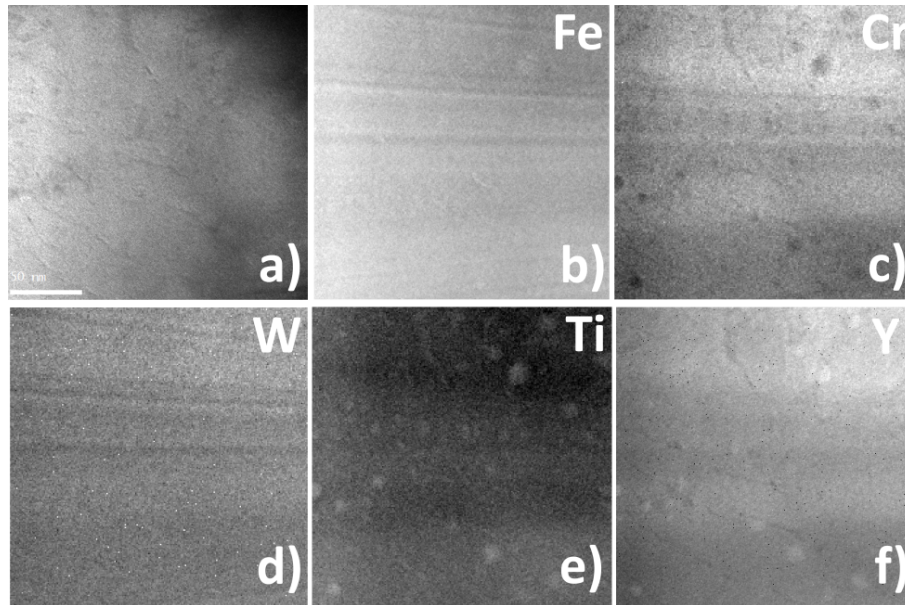


Figure 9. EFTEM elemental maps of the 14YWTi 600°C alloy showing the morphology and chemical composition of Y-rich nanoparticles a) elastic image, b) Fe M2,3 map, c) Cr M2,3 map, d) W (N6,3 + O2,3) map, e) Ti M2,3 map and f) Y N2,3 map.

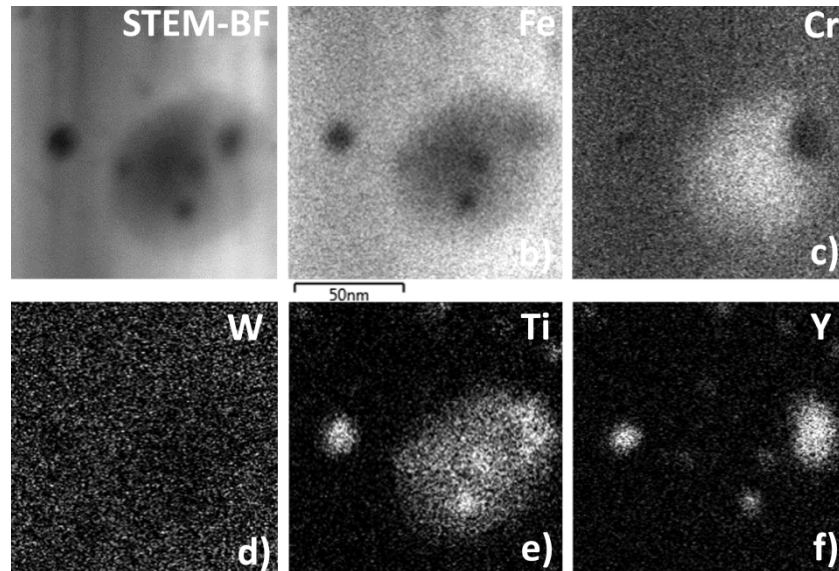


Figure 10. STEM image and EDS elemental maps of the 14YWTi 600°C alloy. a) BF image, b) Fe K map, c) Cr K map, d) W L map, e) Ti K map, f) Y L map.

In this case, four APT datasets with volumes between 2.5×10^{-23} and $2.9 \times 10^{-22} \text{ m}^3$ were analysed; 3D ion maps from one of them are displayed in Fig. 11a and Video 2.

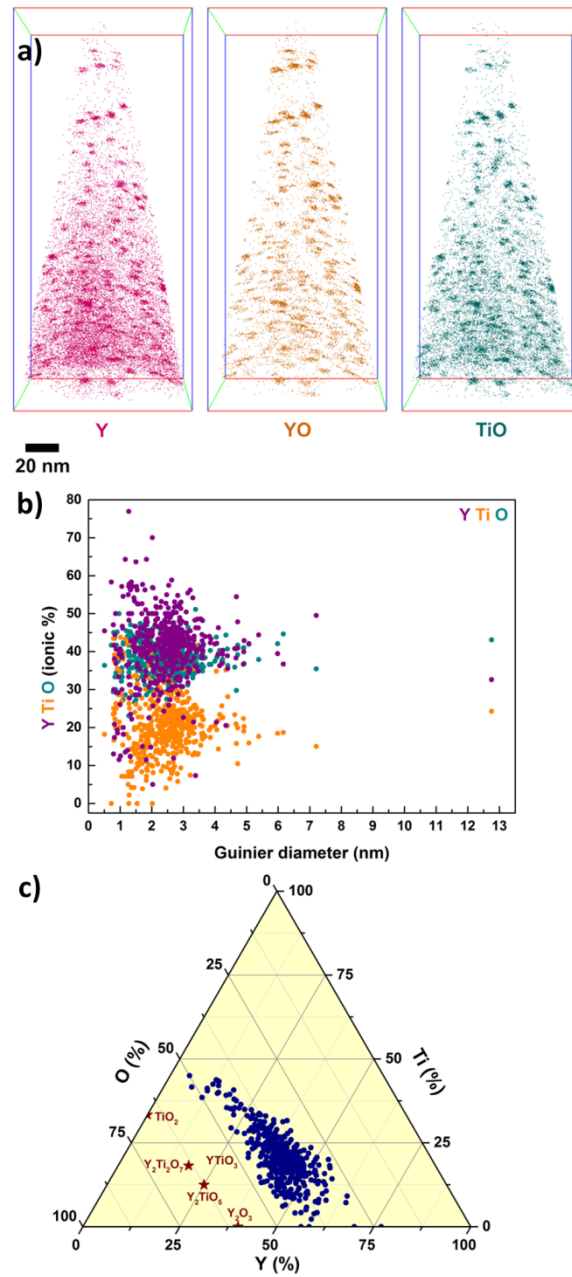


Figure 11. APT measurements for the 14YWTi 600°C sample. a) 3D-ion maps of Y, YO and TiO [Video 2]. Y, Ti and O content in the clusters, b) as a function of their size and c) as a ternary diagram.

Video 2. 3D-ion maps of Y, YO and TiO for the 14YWTi unirradiated sample.

The cluster size measured by APT is displayed in Fig. 7c; the average cluster size after the irradiation is 2.5 ± 1.0 nm for sizes in the range [0.5, 13] nm. The cluster shape is displayed in Fig. 7d and summarised in Table 2; even though most of the clusters are spherical, the amount of disc shaped clusters is double than in the unirradiated sample. The amount of rod shaped clusters has increased slightly, while the amount of lath shaped remains the same. In the cluster distance histogram shown in Fig. 8b, it is observed that the distance between nanoclusters does not change as compared to the unirradiated samples. In this case, the measured distances are in the range [1.6, 25] nm, with an average value of 9 ± 4 nm. The chemical composition of the nanoclusters can be seen in Figs. 11b and 11c and in Table 3. The number density measured by APT ranges between $(1.6 \pm 0.3) \times 10^{23} \text{ m}^{-3}$ and $(1.9 \pm 0.4) \times 10^{24} \text{ m}^{-3}$.

Irradiation-induced bubbles are visible by TEM, see Fig. 12. They can be seen as bright dots in underfocused images (Fig. 12a) and as dark dots in overfocused ones (Fig. 12c). The majority of the bubbles (presumably filled with He) have sizes <4 nm, being mostly at nanoparticle-matrix interfaces although few larger bubbles can be seen attached to larger precipitates as shown in Fig. 12. These sizes are in agreement with other investigations of high temperature irradiations of similar materials [33–35].

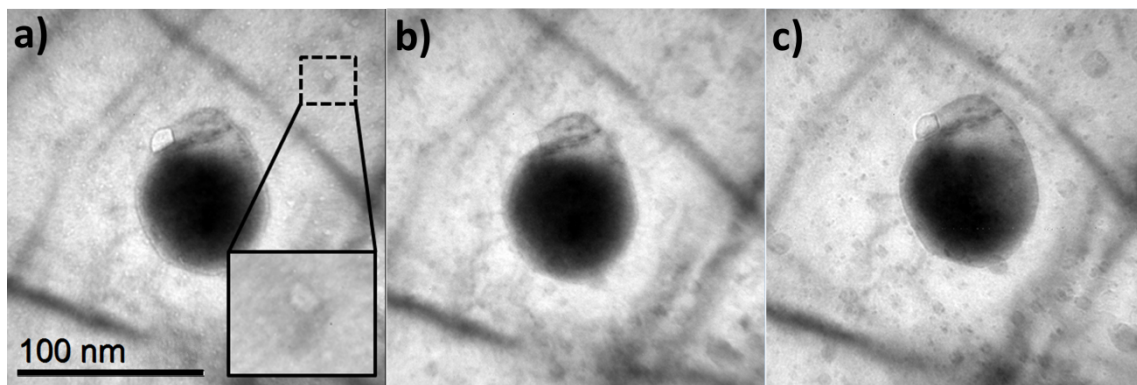


Figure 12. Through-focal series of irradiation induced bubbles in the 14YWTi 600°C alloy. a) underfocused by $1\mu\text{m}$, b) in focus and c) overfocused by $1\mu\text{m}$.

Other irradiation-induced defects could not be analysed by TEM due to the fact that the samples had been FIBed. However, previous Doppler Broadening (DB) slow PAS measurements were performed on the same ODS steels irradiated under the same conditions as a function of depth [36]. This technique allows extracting information about open volume defects (such as dislocations, vacancies, vacancy clusters...) as the DB shift of photon energies coming from e^+e^- annihilations depends on the momentum distribution of the annihilation electrons of the material [37]. The broadening can be characterized using the S-parameter, defined as the count ratio between the central area of the annihilation peak and the total peak counts. These results show that for this high temperature irradiation there is a noticeable defect annealing, see Fig. 13.

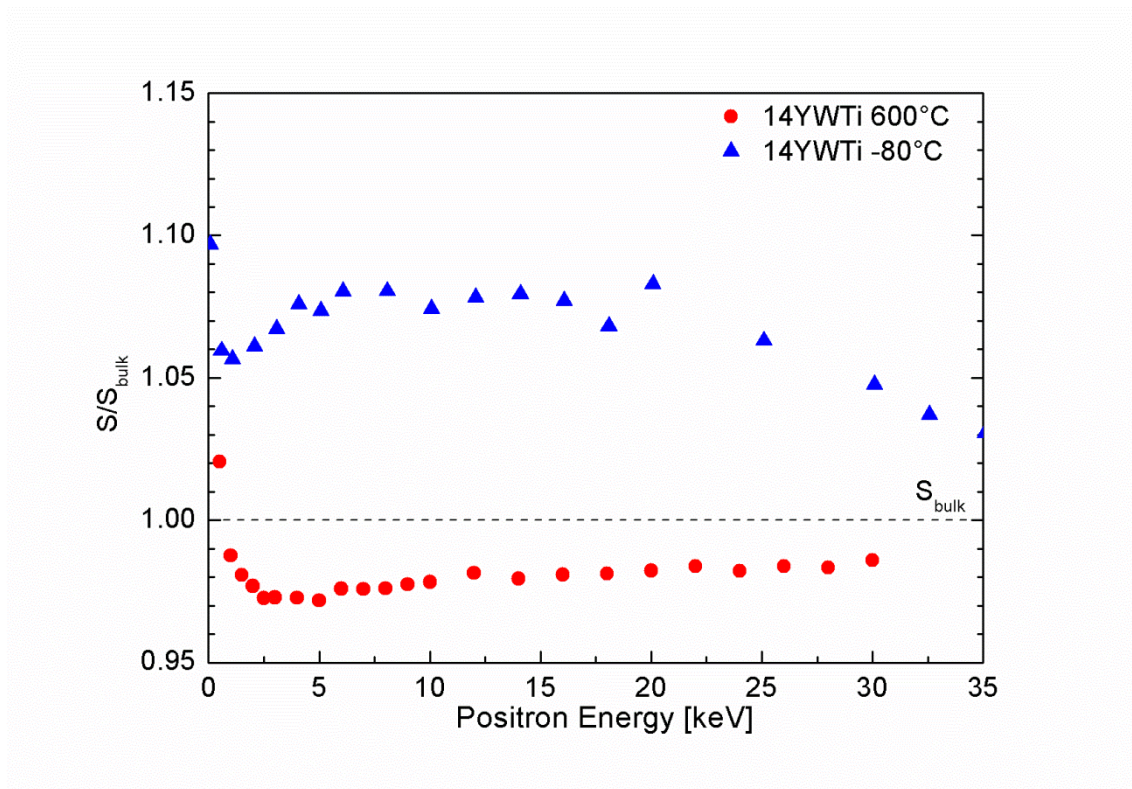


Figure 13. PAS line-shape parameter S/S_{bulk} for 14YWTi 600°C and 14YWTi -80°C with respect to positron energy.

3.3 Microstructure after single irradiation at -80°C

The microstructure of grains in the 14YWTi -80°C sample also appears to have remained unaffected by the low temperature irradiation. A series of STEM images of the nanoparticle dispersion can be seen in Fig. 14.

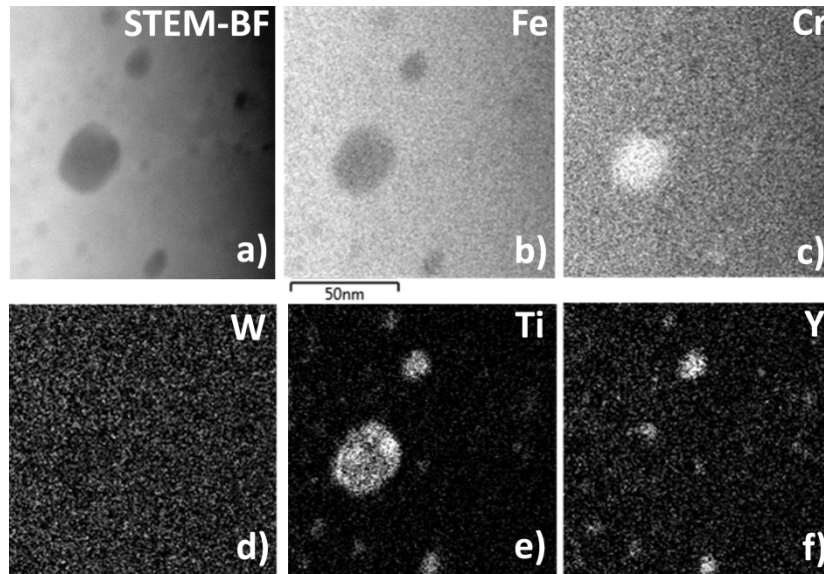


Figure 14. STEM image and EDS elemental maps of the 14YWTi- CMAM alloy. a) BF image, b) Fe K map, c) Cr K map, d) W L map, e) Ti K map, f) Y L map.

It appears that after this low temperature irradiation the morphology and chemical composition of the nanoparticles remain unaltered, being Ti-Cr rich (larger particles) or Y- Ti rich (smaller particles). The particle size distribution measured by TEM is depicted in Fig. 5c. In this case only 35 nanoparticles were visible in the available regions, therefore although the average particle size (7 ± 4 nm) appears to be similar than before irradiation, the statistics is not enough to be conclusive. For the same reason number densities were not calculated.

Fig. 15a and Video 3 depict an APT reconstruction after the low temperature irradiation. In this case, one APT dataset with a volume of 2.1×10^{-22} m³ was analysed with nanoparticle sizes ranging between 0.5 and 12 nm. The APT histogram in Fig. 7e shows that after the low temperature irradiation the average cluster size is 2.1 ± 1.0 nm. The number density of the

measured nanoclusters is $(9.2 \pm 1.8) \times 10^{23} \text{ m}^{-3}$. The cluster shape is shown in Fig. 7f and summarized in Table 2. The cluster distance histogram depicted in Fig. 8c shows a decrease in the distance between nanoclusters respect to the other two samples, with an average value of $7 \pm 3 \text{ nm}$ in a [1.8, 17] nm range. The chemical composition appears to remain unaltered, see Figs 15b and 15c and Table 3.

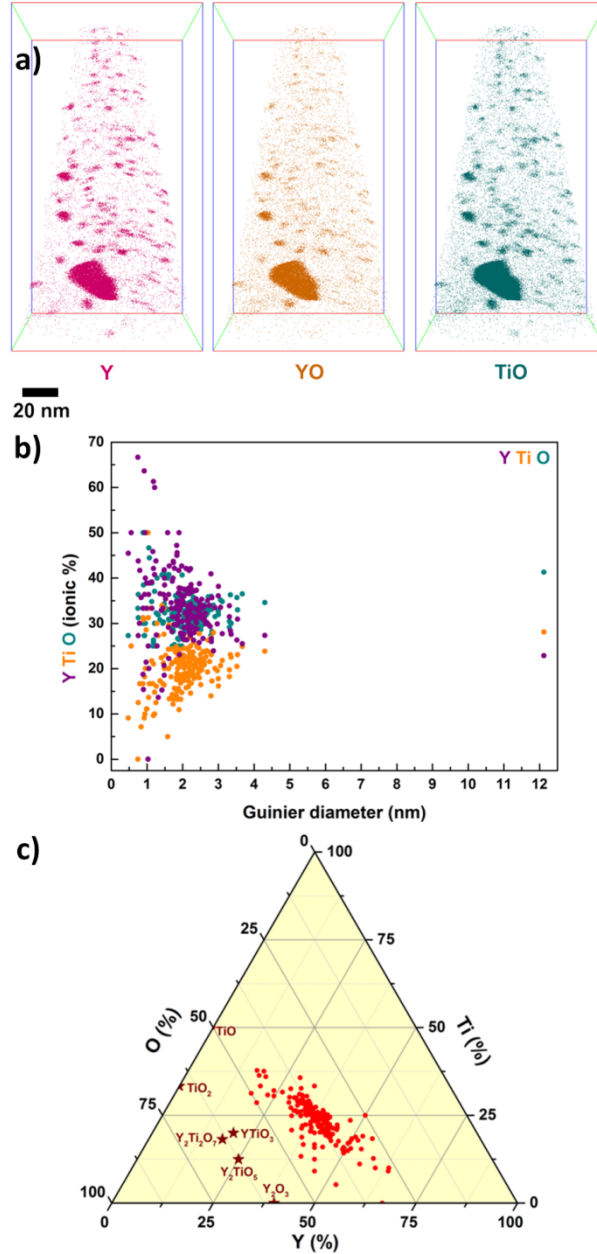


Figure 15. APT measurements for the 14YWTi -80°C sample. a) 3D-ion maps of Y, YO and TiO [Video 3]. Y, Ti and O content in the clusters b) as a function of their size and c) as a ternary diagram.

Video 3 3D-ion maps of Y, YO and TiO for the 14YWTi unirradiated sample.

Regarding defect structure, no voids are visible by TEM. However, slow PAS measurements which can detect open volume defects well below TEM resolution show that this low temperature irradiation increases their number considerably (Fig. 13) [38].

3.4 Nanoindentation

The results of the nanoindentation experiments as a function of depth are depicted in Figs. 16a (elastic modulus) and 16b (hardness). Although the ion range is different in both irradiations the results can be compared with respect to the unirradiated material. No changes in modulus data is seen for either irradiation condition. As it can be seen there are no significative differences between the hardness values obtained in the irradiated samples, as all the data lay within the standard deviation of the unirradiated sample. In any case, some subtle differences could be addressed. For sample 14YWTi 600°C the hardness values appear to be below those for the unirradiated sample for all the measured depths. Cluster distances measured by APT do not change with this irradiation (Fig. 8b). This suggests that the material could have been annealed during this irradiation, which would lead to this slight decrease of the hardness value in agreement with the slow PAS results. It seems that there is no hardening effect due to the He bubbles in agreement with previous results of a 19Cr ODS steel dual ion irradiated at 500°C [39].

For 14YWTi -80°C there appears to be a slight hardening in the region with maximum irradiation damage (Bragg peak estimated at ~ 300nm, Fig. 1b), although it is well within the experimental error of the values obtained for the unirradiated sample. These results would be consistent with both APT and slow PAS measurements. APT results show a decrease in the distance between nanoclusters (Fig. 8c) and slow PAS show an increase in the number of open volume defects (Fig.

13). All these changes would lead to an increase in hardness in agreement with other studies performed in an ODS FeCrAl alloy irradiated at room temperature [40].

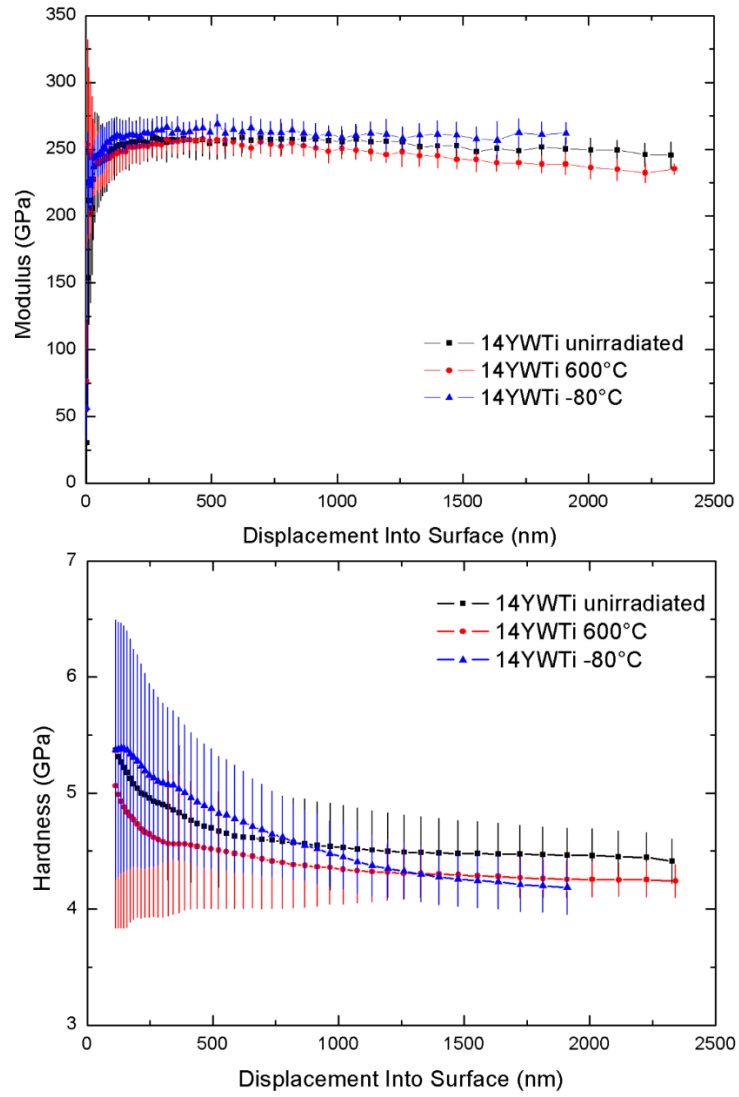


Figure 16. Nanoindentation results for 14YWTi, 14YWTi 600°C and 14YWTi -80°C: a) Elastic modulus with respect to depth and b) hardness with respect to depth.

4. Discussion

Table 4 presents a summary of the results obtained with TEM and APT in all the materials investigated. For the sample triple irradiated at 600°C, combined TEM and APT observations suggest that the irradiation does not induce any change in the composition of nanoparticles, while there are some subtle changes in their sizes and morphology. TEM nanoparticle size histograms depicted in Figs. 5a and 5b show that, for the five studied regions, there appears to be a lower amount of particles smaller than 5 nm, while there is a small increase in the overall average size suggesting some coarsening. Moreover, APT results, that focus almost solely on nanoparticles smaller than ~ 5 nm, show a slight decrease in their sizes and, in some of them, a modification of their morphologies from spherical to disc shaped. This may match the observed TEM histogram supposing that larger nanoparticles grow at the expense of the smaller ones. Furthermore, the smallest nanoclusters may now be below TEM resolution thus explaining the decrease in density measured by TEM. The fact that nanocluster distances measured by APT do not change would imply that even if the size of the smaller nanoparticles has decreased during the irradiation, they do not completely dissolve. Irradiation induced bubbles are present in the matrix with sizes smaller than 4nm. Hardness values post irradiation are slightly lower than those for the unirradiated sample which suggests that the sample could have been annealed due to the high temperature of the irradiation.

The results obtained for the samples irradiated at -80°C also show that the composition does not change significantly, while the morphology of the clusters tends to be more disc shaped. The percentages of each shape type (spherical and disk) are very similar to the 14YWTi 600°C samples, suggesting that both irradiations similarly altered the geometry of the clusters. The average nanoparticle size measured by TEM does not grow after the low temperature irradiation, contrary to what happened in the previous irradiation, while APT measurements indicate a size reduction of the smaller particles of ~27%. The decrease in average cluster size

observed by APT agrees with previously published results of low temperature (-75°C) heavy ion irradiations of a material with similar nominal composition which show that already at the irradiation damage of 5 dpa, there is a noticeable dissolution of nanoclusters [12]. In the present work the decrease in the average cluster distance measured would also suggest that for these irradiation conditions dissolution could be accompanied by nucleation of new clusters.

Sample	Technique	Morphology	Average Chemical composition (at%)	Average Size (nm)	Number density (m ⁻³)	Average cluster distance (nm)
14YWTi unirradiated	TEM	round	Y-Ti rich	8 ± 5	(1.1 ± 0.2) x 10 ²²	
	APT	72.5% spherical 20.3% disc	38±10% Y 24±6% Ti 38±6% O	2.9 ± 1.1	(3.4 ± 0.7) x 10 ²³ - (1.0 ± 0.2) x 10 ²⁴	9 ± 3
14YWTi 600°C	TEM	round	Y-Ti rich	10 ± 4	(4.8 ± 1.0) x 10 ²¹	
	APT	48.7% spherical 41.4% disc	41±9% Y 21±7% Ti 38±4% O	2.5 ± 1.0	(1.6 ± 0.3) x 10 ²³ - (1.9 ± 0.4) x 10 ²⁴	9 ± 4
14YWTi -80°C	TEM	round	Y-Ti rich	7 ± 4	N.A.	
	APT	47.0% spherical 43.4% disc	39±8% Y 24±6% Ti 38±4% O	2.1 ± 1.0	(9.2 ± 1.8) x 10 ²³	7 ± 3

Table 4. TEM and APT results of nanoparticle evolution due to both irradiations.

5. Conclusions

In this work, a Fe-14Cr-2W-0.2Ti-0.3Y₂O₃ alloy was irradiated with two different conditions. One sample of this alloy was triple ion-beam irradiated at high temperature, and another was single ion beam irradiated at low temperature. The nanoparticle evolution was analysed by TEM and APT as complementary techniques. Nanoparticles appear to remain quite stable after the two irradiations investigated. Both samples seem to have maintained their composition after the irradiations, and the effects in the nanoparticle size distribution are very weak. In any case, some changes could be observed. APT results show a slight decrease of the nanoparticle sizes below 5 nm at both temperatures while TEM histograms would suggest growth of the larger nanoparticles for the high temperature irradiation. The distance between clusters measured by APT does not change for the high temperature irradiation while their distance decreases for the low temperature one. These differences could indicate that incomplete dissolution of some of the smaller nanoparticles occurs after both irradiations, with nucleation of new particles in the case of the low temperature irradiation, and slight coarsening of existing particles after the triple-beam irradiation at high temperature. In the triple-beam irradiated sample, a dispersion of small irradiation induced bubbles is present. Nanoindentation experiments also show very little differences, pointing to some recovery in the high temperature irradiation, which would be in agreement with the microstructural changes observed.

References

- [1] O. Motojima, The ITER project construction status, Nucl. Fusion. 55 (2015) 104023.
doi:10.1088/0029-5515/55/10/104023.
- [2] D. Stork, P. Agostini, J.L. Boutard, D. Buckthorpe, E. Diegele, S.L. Dudarev, C. English, G. Federici, M.R. Gilbert, S. Gonzalez, A. Ibarra, C. Linsmeier, A. Li Puma, G. Marbach, P.F. Morris, L.W. Packer, B. Raj, M. Rieth, M.Q. Tran, D.J. Ward, S.J. Zinkle, Developing structural, high-heat flux and plasma facing materials for a near-term DEMO fusion

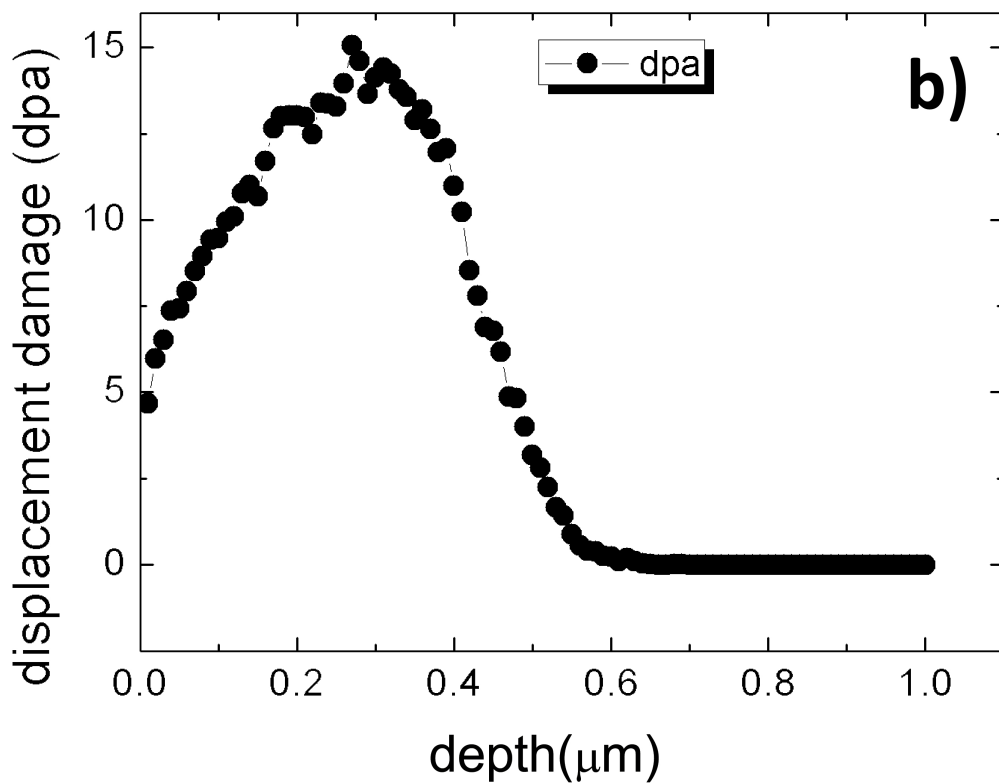
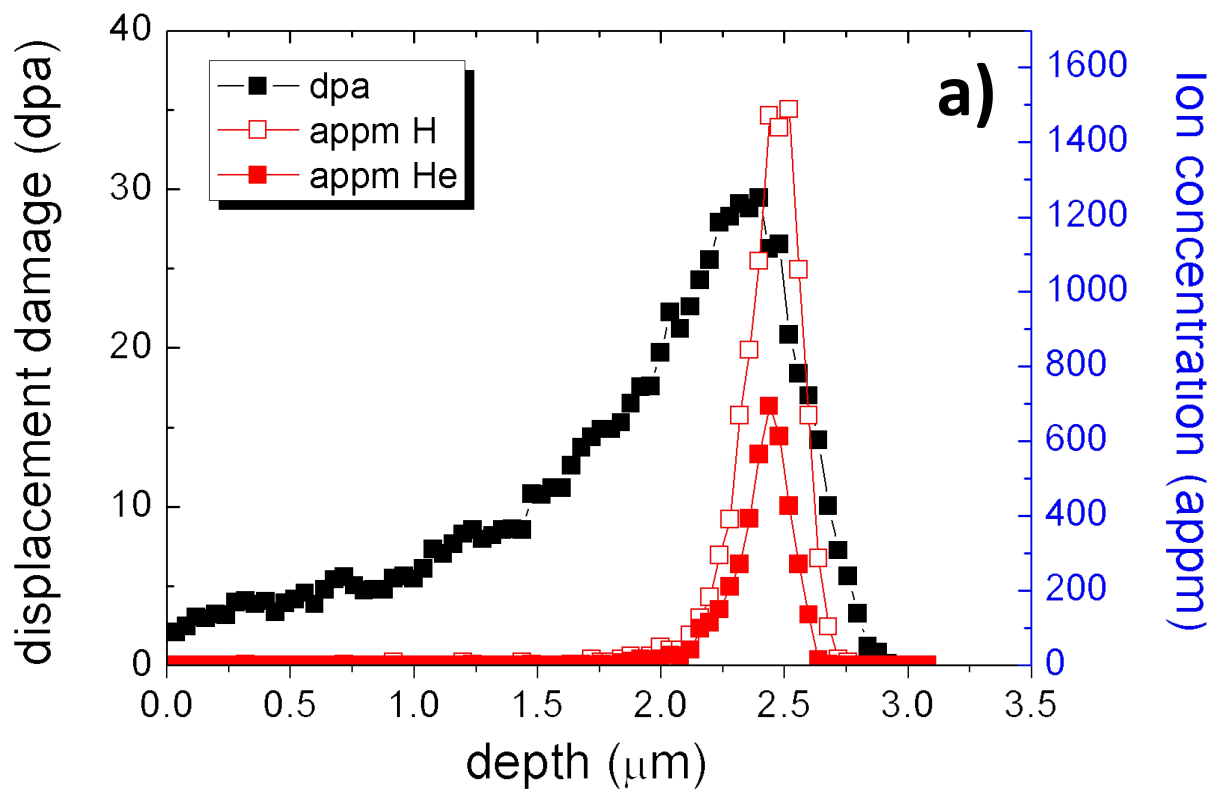
- power plant: The EU assessment, *J. Nucl. Mater.* 455 (2014) 277–291.
doi:10.1016/j.jnucmat.2014.06.014.
- [3] J.L. Boutard, A. Alamo, R. Lindau, M. Rieth, Fissile core and Tritium-Breeding Blanket: structural materials and their requirements, *Comptes Rendus Phys.* 9 (2008) 287–302.
doi:10.1016/j.crhy.2007.11.004.
- [4] R.L. Klueh, D.R. Harries, High-chromium ferritic and martensitic steels for nuclear applications, ASTM International, 2001.
- [5] G.R. Romanoski, L.L. Snead, R.L. Klueh, D.T. Hoelzer, Development of an oxide dispersion strengthened, reduced-activation steel for fusion energy, *J. Nucl. Mater.* 283–287 (2000) 642–646. doi:10.1016/S0022-3115(00)00137-9.
- [6] G.R. Odette, M.J. Alinger, B.D. Wirth, Recent Developments in Irradiation-Resistant Steels, *Annu. Rev. Mater. Res.* 38 (2008) 471–503.
doi:10.1146/annurev.matsci.38.060407.130315.
- [7] R. Schäublin, A. Ramar, N. Baluc, V. de Castro, M.A. Monge, T. Leguey, N. Schmid, C. Bonjour, Microstructural development under irradiation in European ODS ferritic/martensitic steels, *J. Nucl. Mater.* 351 (2006) 247–260.
doi:10.1016/j.jnucmat.2006.02.005.
- [8] S.J. Zinkle, L.L. Snead, Designing Radiation Resistance in Materials for Fusion Energy, *Annu. Rev. Mater. Res.* 44 (2014) 241–67. doi:10.1146/annurev-matsci-070813-113627.
- [9] S. Ukai, M. Fujiwara, Perspective of ODS alloys application in nuclear environments, *J. Nucl. Mater.* 307–311 (2002) 749–757. doi:10.1016/S0022-3115(02)01043-7.
- [10] M.L. Lescoat, J. Ribis, A. Gentils, O. Kaïtasov, Y. De Carlan, A. Legris, In situ TEM study of the stability of nano-oxides in ODS steels under ion-irradiation, *J. Nucl. Mater.* 428 (2012) 176–182. doi:10.1016/j.jnucmat.2011.12.009.
- [11] M.L. Lescoat, J. Ribis, Y. Chen, E.A. Marquis, E. Bordas, P. Trocellier, Y. Serruys, A. Gentils, O. Kaïtasov, Y. De Carlan, A. Legris, Radiation-induced Ostwald ripening in oxide

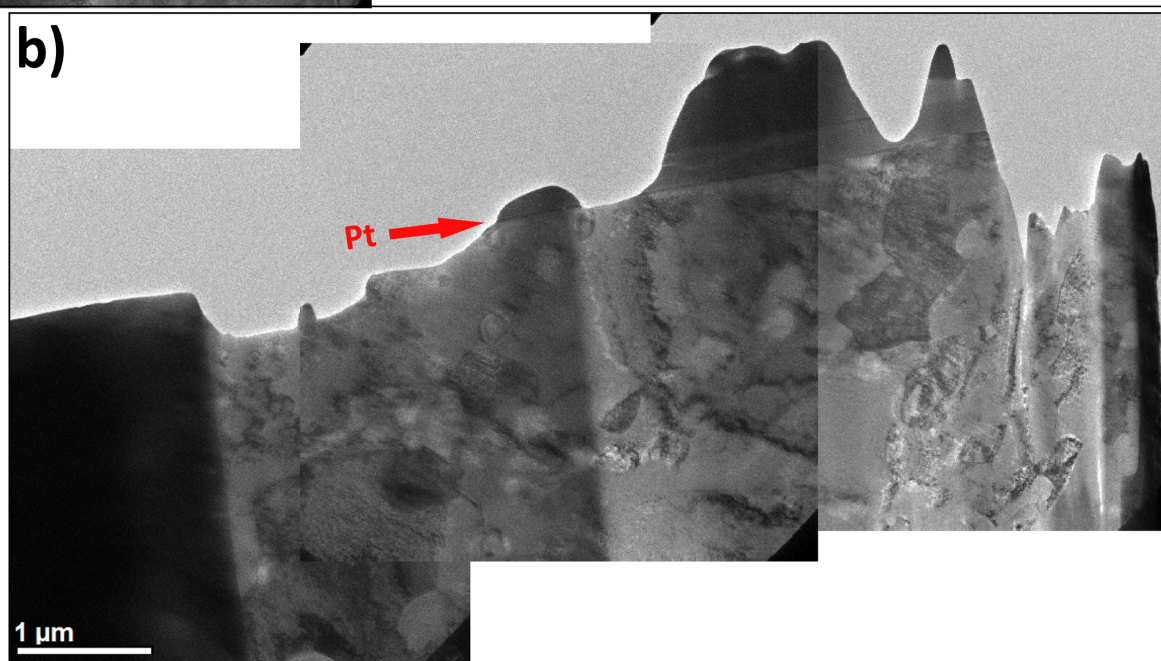
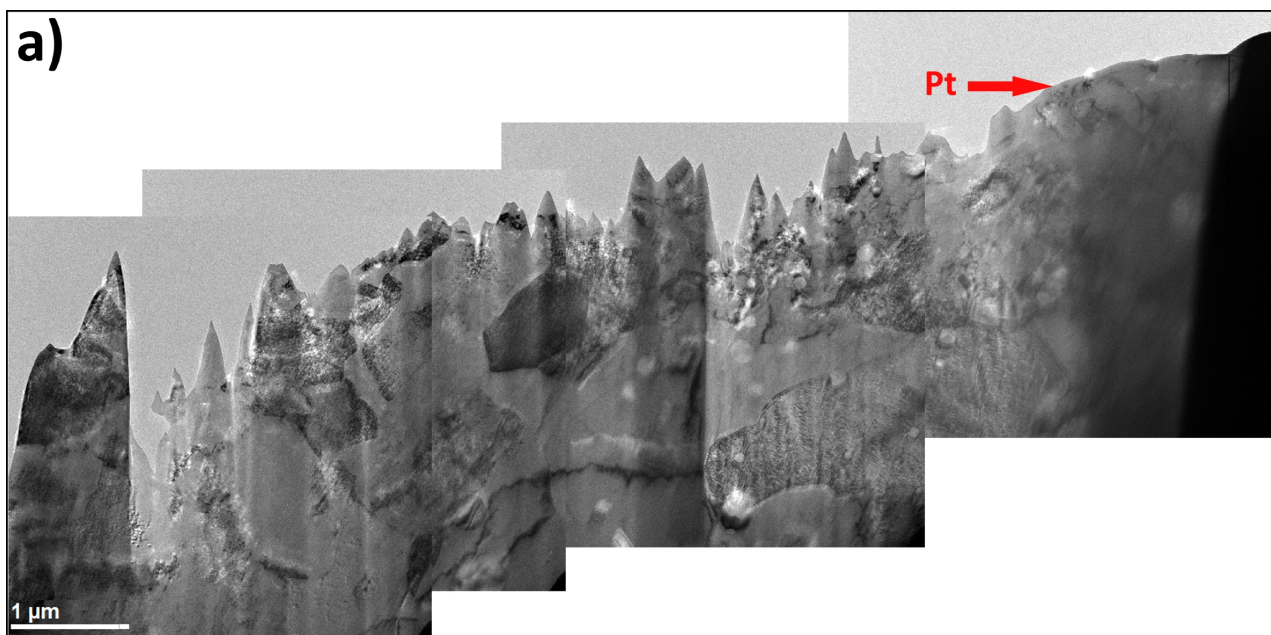
- dispersion strengthened ferritic steels irradiated at high ion dose, *Acta Mater.* 78 (2014) 328–340. doi:10.1016/j.actamat.2014.06.060.
- [12] A. Certain, S. Kuchibhatla, V. Shutthanandan, D.T. Hoelzer, T.R. Allen, Radiation stability of nanoclusters in nano-structured oxide dispersion strengthened (ODS) steels, *J. Nucl. Mater.* 434 (2013) 311–321. doi:10.1016/j.jnucmat.2012.11.021.
- [13] J.P. Wharry, M.J. Swenson, K.H. Yano, A review of the irradiation evolution of dispersed oxide nanoparticles in the b.c.c. Fe-Cr system: Current understanding and future directions, *J. Nucl. Mater.* 486 (2017) 11–20. doi:10.1016/j.jnucmat.2017.01.009.
- [14] M. a. Auger, V. de Castro, T. Leguey, M. a. Monge, a. Muñoz, R. Pareja, Microstructure and tensile properties of oxide dispersion strengthened Fe–14Cr–0.3Y₂O₃ and Fe–14Cr–2W–0.3Ti–0.3Y₂O₃, *J. Nucl. Mater.* 442 (2013) S142–S147. doi:10.1016/j.jnucmat.2012.11.001.
- [15] Y. Serruys, P. Trocellier, S. Miro, E. Bordas, M.O. Ruault, O. Kaïtasov, S. Henry, O. Leseigneur, T. Bonnaillie, S. Pellegrino, S. Vaubaillon, D. Uriot, JANNUS: A multi-irradiation platform for experimental validation at the scale of the atomistic modelling, *J. Nucl. Mater.* 386–388 (2009) 967–970. doi:10.1016/j.jnucmat.2008.12.262.
- [16] S. Pellegrino, P. Trocellier, S. Miro, Y. Serruys, É. Bordas, H. Martin, N. Chaâbane, S. Vaubaillon, J.P. Gallien, L. Beck, The JANNUS Saclay facility: A new platform for materials irradiation, implantation and ion beam analysis, *Nucl. Instruments Methods Phys. Res. Sect. B Beam Interact. with Mater. Atoms.* 273 (2012) 213–217. doi:10.1016/j.nimb.2011.07.078.
- [17] P. Trocellier, S. Miro, Y. Serruys, S. Vaubaillon, S. Pellegrino, S. Agarwal, S. Moll, L. Beck, Study of helium migration in nuclear materials at Jannus-Saclay, *Nucl. Instruments Methods Phys. Res. Sect. B Beam Interact. with Mater. Atoms.* 331 (2014) 55–64. doi:10.1016/j.nimb.2014.01.027.
- [18] J.P. Biersack, J.F. Ziegler, *The Stopping and Range of Ions in Solids*, Pergamon, New

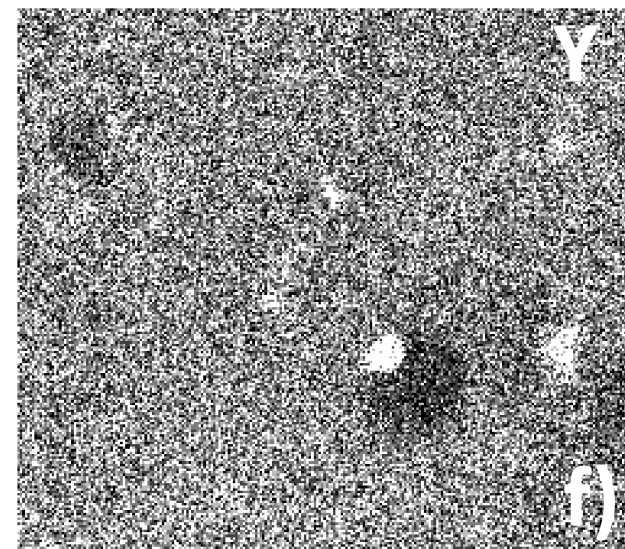
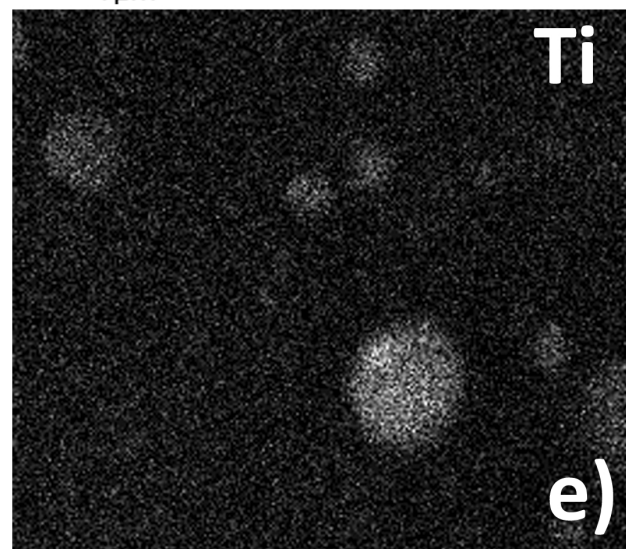
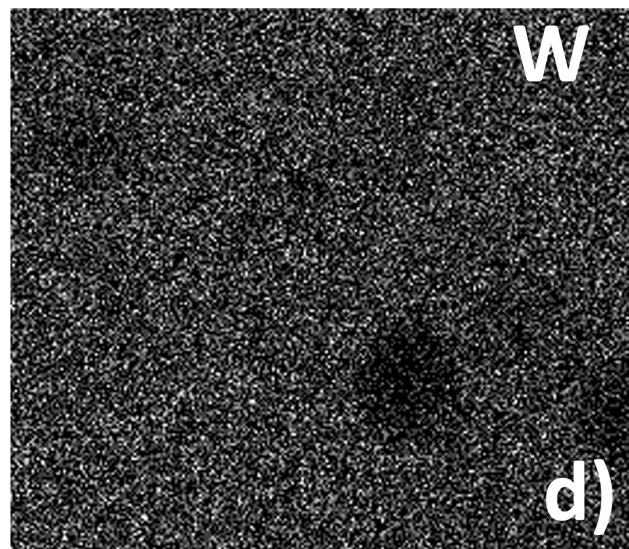
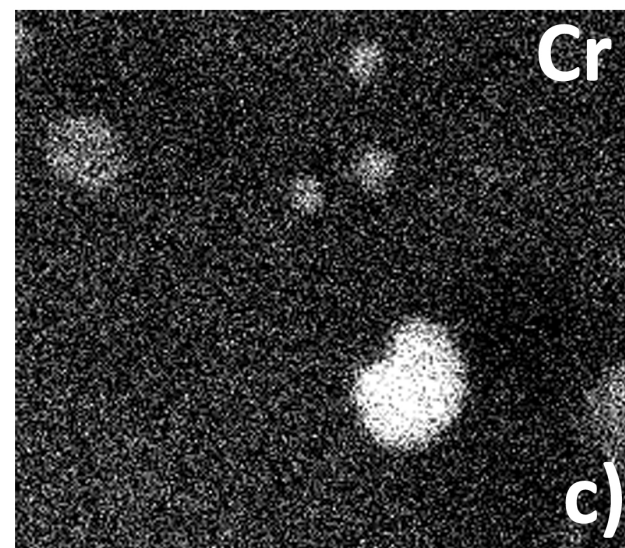
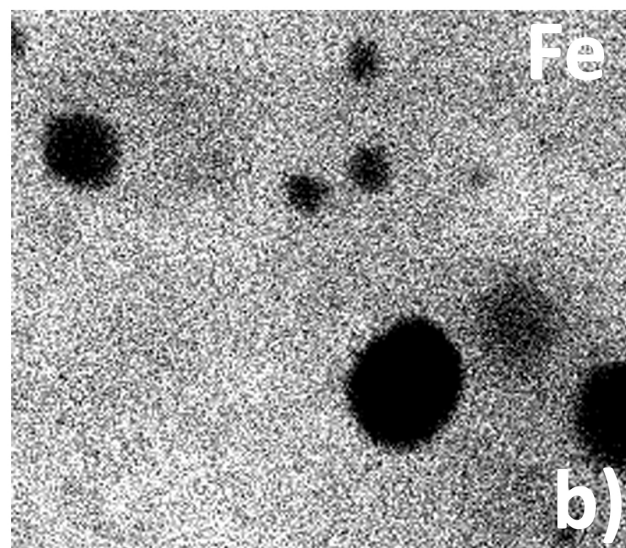
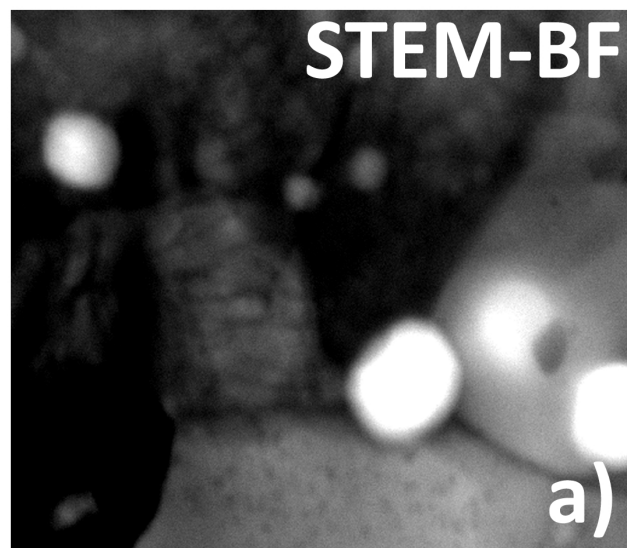
- York, 1982. doi:10.1007/978-3-642-68779-2_5.
- [19] M. Šćepanović, V. de Castro, T. Leguey, M.A. Auger, S. Lozano-Perez, R. Pareja, Microstructural stability of ODS Fe-14Cr (-2W-0.3Ti) steels after simultaneous triple irradiation, *Nucl. Mater. Energy*. 9 (2016) 490–495. doi:10.1016/j.nme.2016.08.001.
 - [20] A. Climent-Font, F. Pászti, G. García, M.T. Fernández-Jiménez, F. Agulló, First measurements with the Madrid 5 MV tandem accelerator, *Nucl. Instruments Methods Phys. Res. Sect. B Beam Interact. with Mater. Atoms*. 219–220 (2004) 400–404. doi:10.1016/j.nimb.2004.01.090.
 - [21] F.J. Sánchez, I. García-Cortés, J.F. Marco, D. Jiménez-Rey, A. Maira, J. Castellanos, R. Vila, Á. Ibarra, Influence of an external magnetic field on damage by self-ion irradiation in Fe 90 Cr 10 alloy, *Nucl. Mater. Energy*. 9 (2016) 476–479. doi:10.1016/j.nme.2016.05.010.
 - [22] D.B. Williams, C.C. Barry, *Transmission Electron Microscopy*, Springer US, 2009. doi:10.1007/978-0-387-76501-3.
 - [23] B. Gault, M.P. Moody, J.M. Cairney, S.P. Ringer, *Atom Probe Microscopy*, Springer-Verlag New York, 2012. doi:10.1007/978-1-4614-3436-8.
 - [24] M.K. Miller, K.F. Russell, K. Thompson, R. Alvis, D.J. Larson, Review of atom probe FIB-based specimen preparation methods, *Microsc. Microanal.* 13 (2007) 428–436. doi:10.1017/S1431927607070845.
 - [25] J.M. Hyde, E.A. Marquis, K.B. Wilford, T.J. Williams, A sensitivity analysis of the maximum separation method for the characterisation of solute clusters, *Ultramicroscopy*. 111 (2011) 440–447. doi:10.1016/j.ultramic.2010.12.015.
 - [26] M.K. Miller, E.A. Kenik, *Atom Probe Tomography : A Technique for Nanoscale Characterization*, *Microsc. Microanal.* (2004) 336–341. doi:10.1017/S1431927604040577.
 - [27] R.K.W. Marceau, L.T. Stephenson, C.R. Hutchinson, S.P. Ringer, Quantitative atom

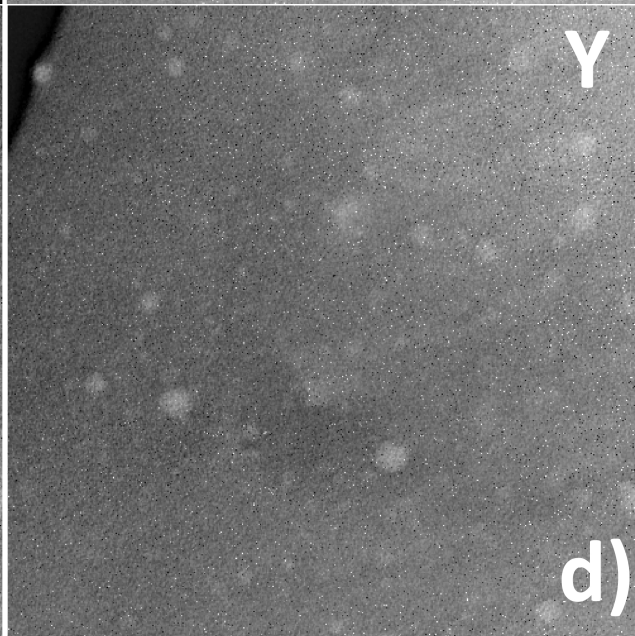
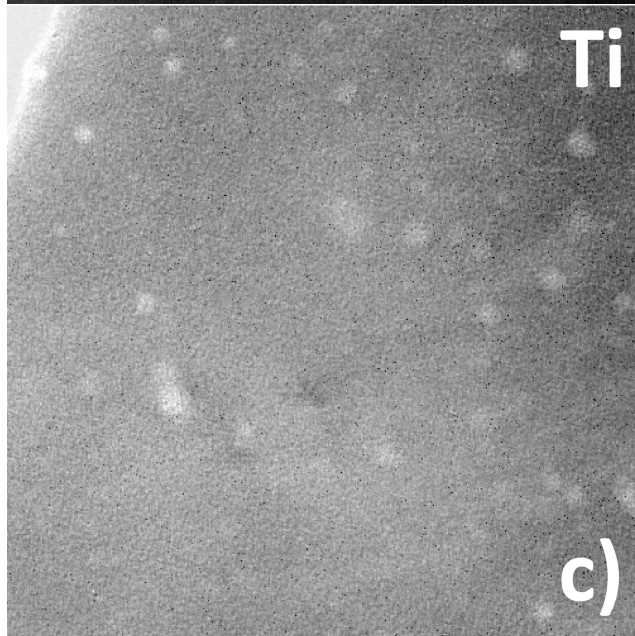
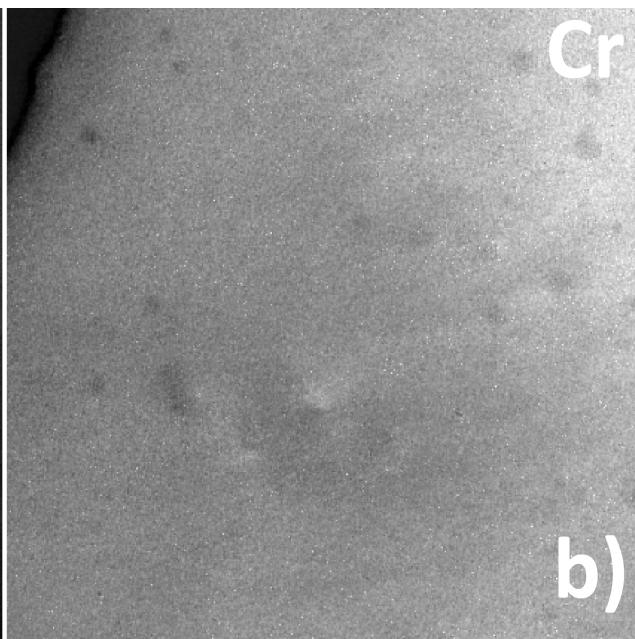
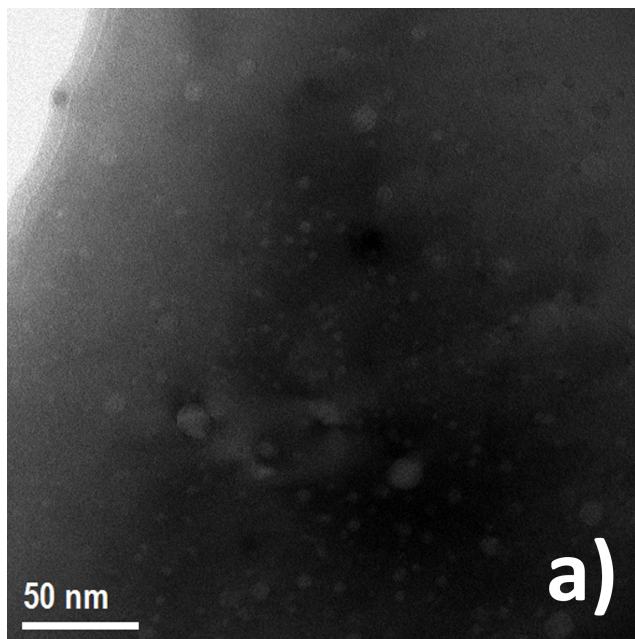
- probe analysis of nanostructure containing clusters and precipitates with multiple length scales, *Ultramicroscopy*. 111 (2011) 738–742.
doi:10.1016/j.ultramic.2010.12.029.
- [28] P. Hosemann, C. Vieh, R.R. Greco, S. Kabra, J.A. Valdez, M.J. Cappiello, S.A. Maloy, Nanoindentation on ion irradiated steels, *J. Nucl. Mater.* 389 (2009) 239–247.
doi:10.1016/j.jnucmat.2009.02.026.
- [29] C. Heintze, F. Bergner, M. Hernandez-Mayoral, Ion-irradiation-induced damage in Fe-Cr alloys characterized by nanoindentation, *J. Nucl. Mater.* 417 (2011) 980–983.
doi:10.1016/j.jnucmat.2010.12.196.
- [30] W.C. Oliver, G.M. Pharr, Measurement of hardness and elastic modulus by instrumented indentation: Advances in understanding and refinements to methodology, *J. Mater. Res.* 19 (2004) 3–20. doi:10.1557/jmr.2004.19.1.3.
- [31] M.A. Auger, V. de Castro, T. Leguey, S. Lozano-Perez, P.A.J. Bagot, M.P. Moody, S.G. Roberts, Effect of the milling atmosphere on the microstructure and mechanical properties of a ODS Fe-14Cr model alloy, *Mater. Sci. Eng. A*. 671 (2016) 264–274.
doi:10.1016/j.msea.2016.06.054.
- [32] M.C. Brandes, L. Kovarik, M.K. Miller, M.J. Mills, Morphology, structure, and chemistry of nanoclusters in a mechanically alloyed nanostructured ferritic steel, *J. Mater. Sci.* 47 (2012) 3913–3923. doi:10.1007/s10853-012-6249-x.
- [33] T. Tanaka, K. Oka, S. Ohnuki, S. Yamashita, T. Suda, S. Watanabe, E. Wakai, Synergistic effect of helium and hydrogen for defect evolution under multi-ion irradiation of Fe-Cr ferritic alloys, *J. Nucl. Mater.* 329–333 (2004) 294–298.
doi:10.1016/j.jnucmat.2004.04.051.
- [34] P.D. Edmondson, C.M. Parish, Y. Zhang, A. Hallén, M.K. Miller, Helium bubble distributions in a nanostructured ferritic alloy, *J. Nucl. Mater.* 434 (2013) 210–216.
doi:10.1016/j.jnucmat.2012.11.049.

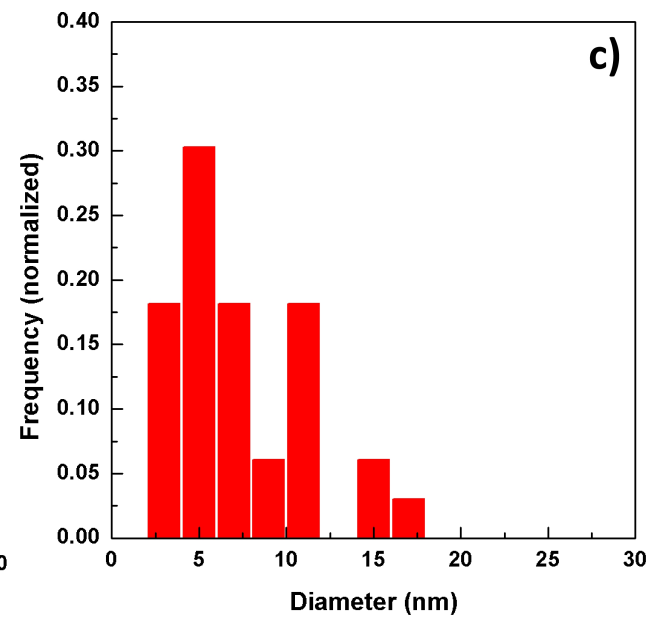
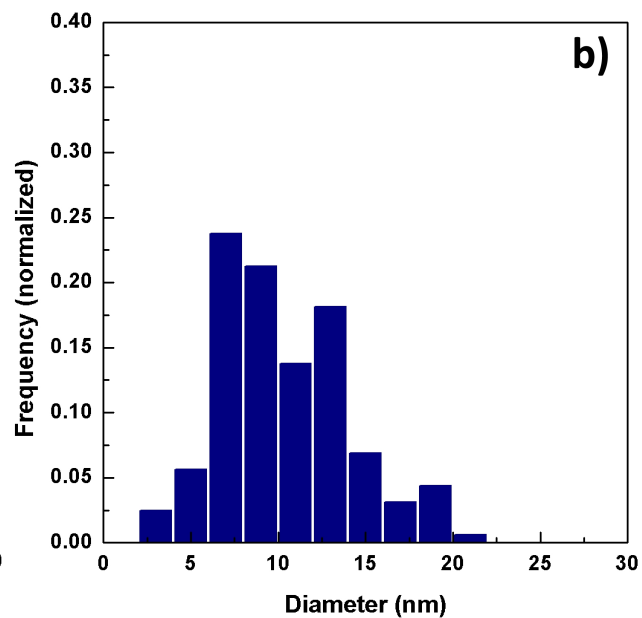
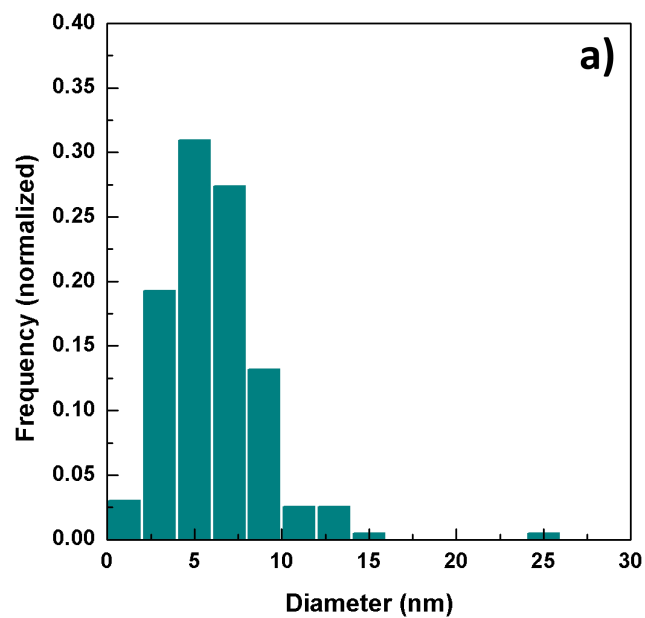
- [35] I.-S. Kim, J.D. Hunn, N. Hashimoto, D.L. Larson, P.J. Maziasz, K. Miyahara, E.H. Lee, Defect and void evolution in oxide dispersion strengthened ferritic steels under 3.2 MeV Fe⁺ ion irradiation with simultaneous helium injection, *J. Nucl. Mater.* 280 (2000) 264–274. doi:10.1016/S0022-3115(00)00066-0.
- [36] P. Parente, T. Leguey, V. De Castro, T. Gigl, M. Reiner, C. Hugenschmidt, R. Pareja, Characterization of ion-irradiated ODS Fe-Cr alloys by doppler broadening spectroscopy using a positron beam, *J. Nucl. Mater.* 464 (2015) 140–146. doi:10.1016/j.jnucmat.2015.04.033.
- [37] M.J. Puska, R.M. Nieminen, The Theory of Positrons in solids and on solid surfaces, *Rev. Mod. Physics*,. 66 (1994) 749–759.
- [38] W. Anwand, T. Leguey, M. Scepanovic, F.J. Sanchez, I. García-Cortés, A. Wagner, Fe⁺ Implantation Induced Damage in Oxide Dispersion Strengthened Steels Investigated by Doppler Broadening Spectroscopy, *Defect Diffus. Forum.* 373 (2017) 113–116. doi:10.4028/www.scientific.net/DDF.373.113.
- [39] H. Kishimoto, K. Yutani, R. Kasada, A. Kimura, Helium cavity formation research on oxide dispersed strengthening (ODS) ferritic steels utilizing dual-ion irradiation facility, *Fusion Eng. Des.* 81 (2006) 1045–1049. doi:10.1016/j.fusengdes.2005.09.049.
- [40] R. Kögler, W. Anwand, A. Richter, M. Butterling, X. Ou, A. Wagner, C.L. Chen, Nanocavity formation and hardness increase by dual ion beam irradiation of oxide dispersion strengthened FeCrAl alloy, *J. Nucl. Mater.* 427 (2012) 133–139. doi:10.1016/j.jnucmat.2012.04.029.

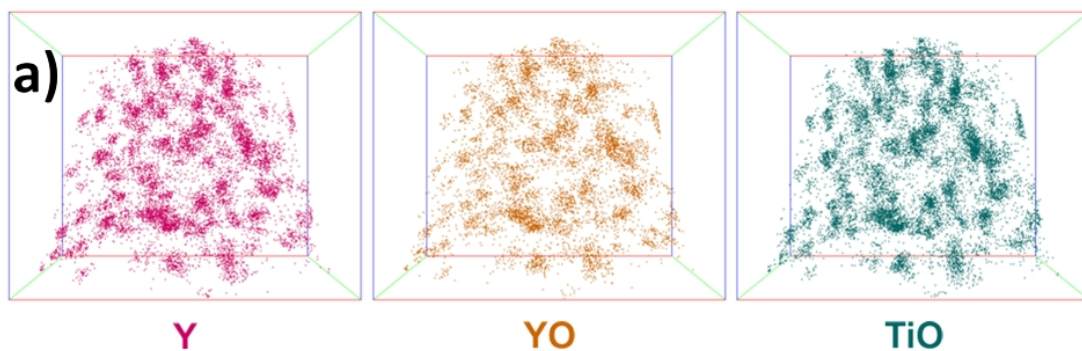




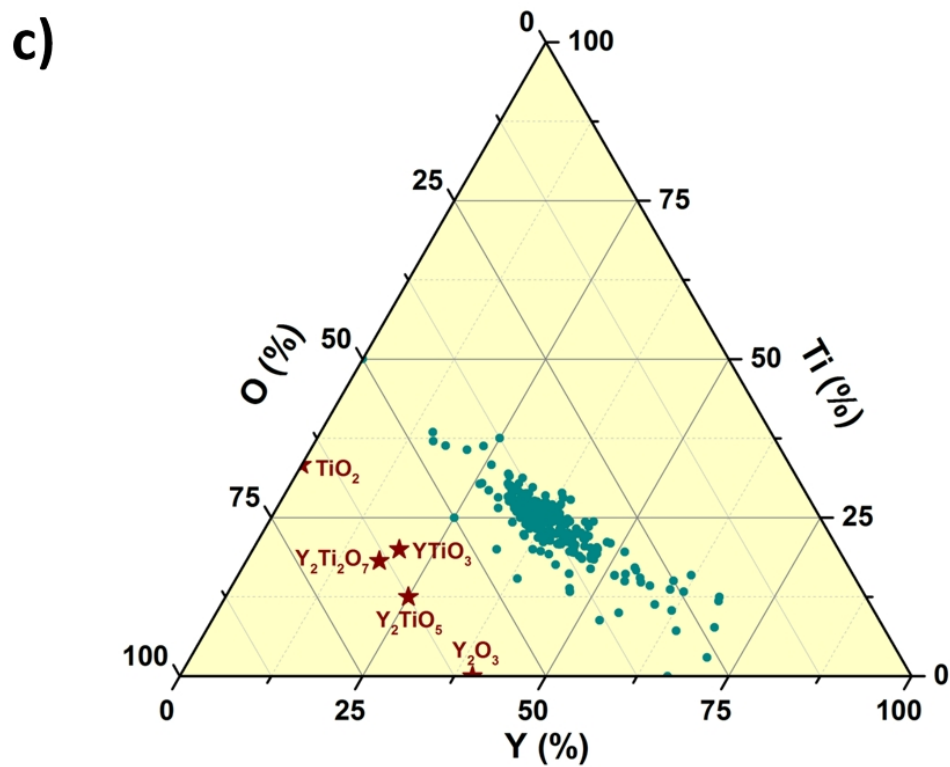
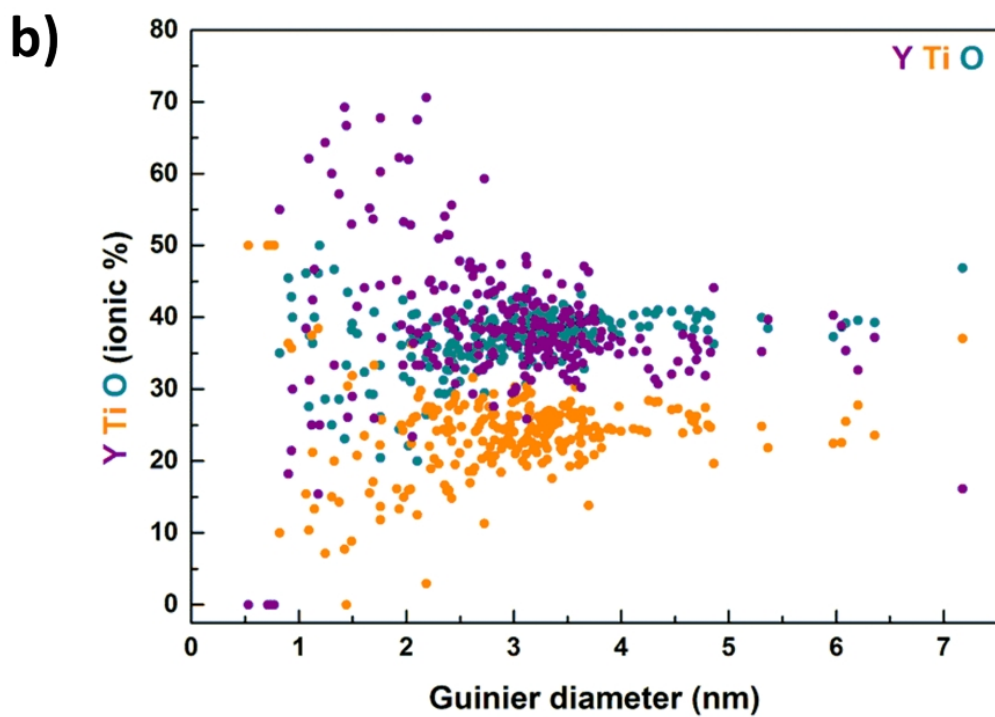


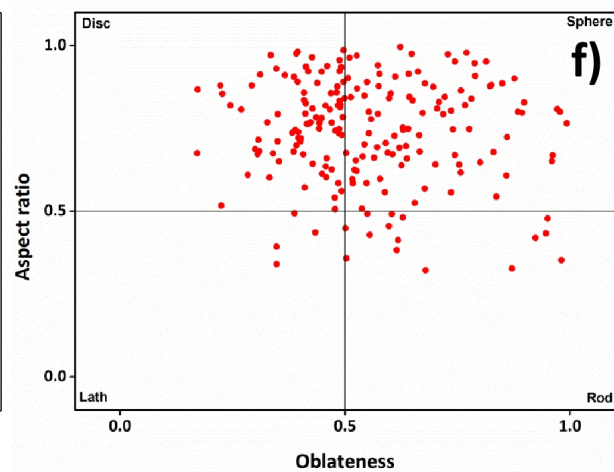
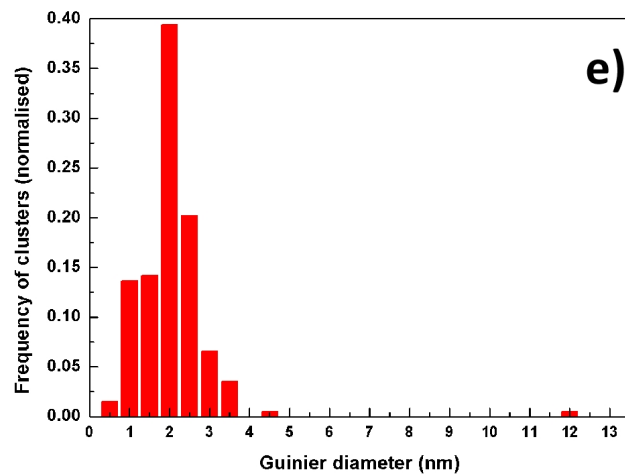
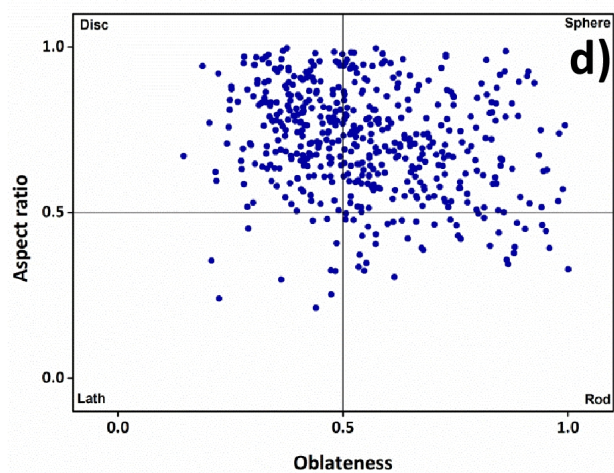
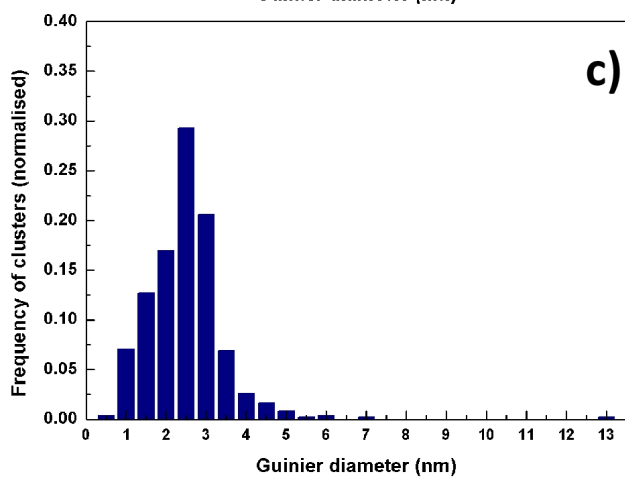
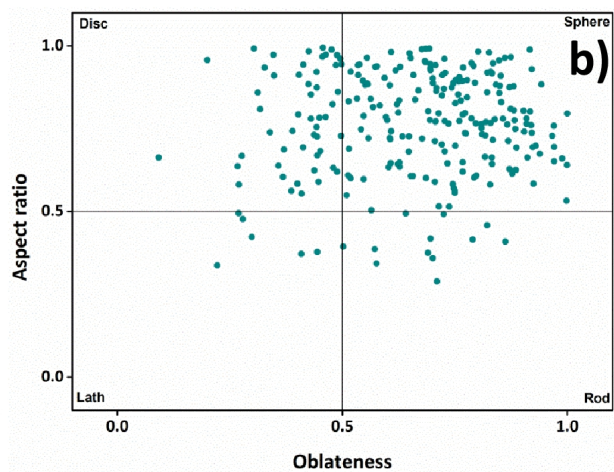
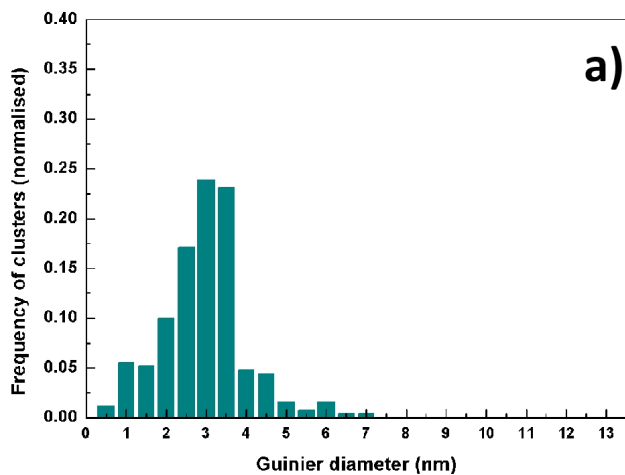


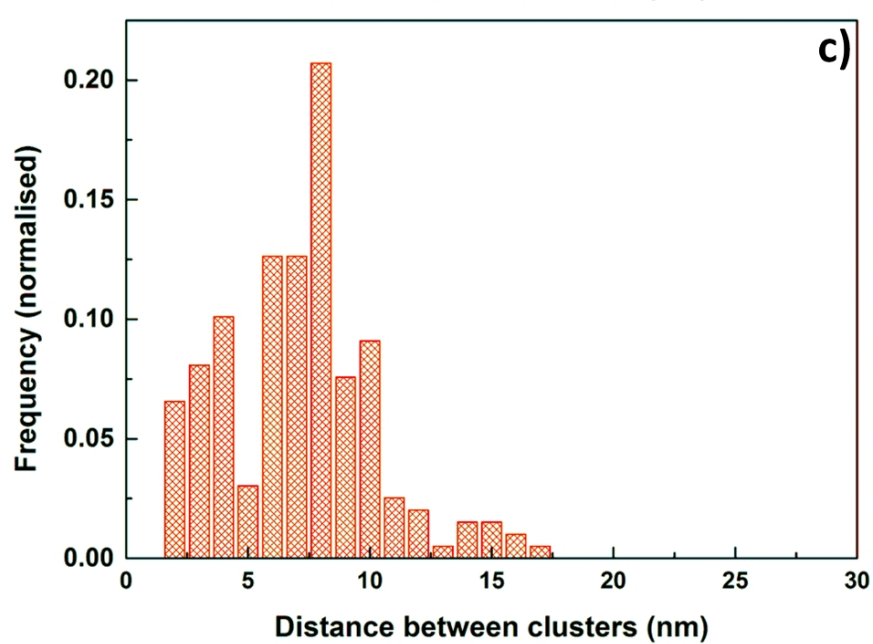
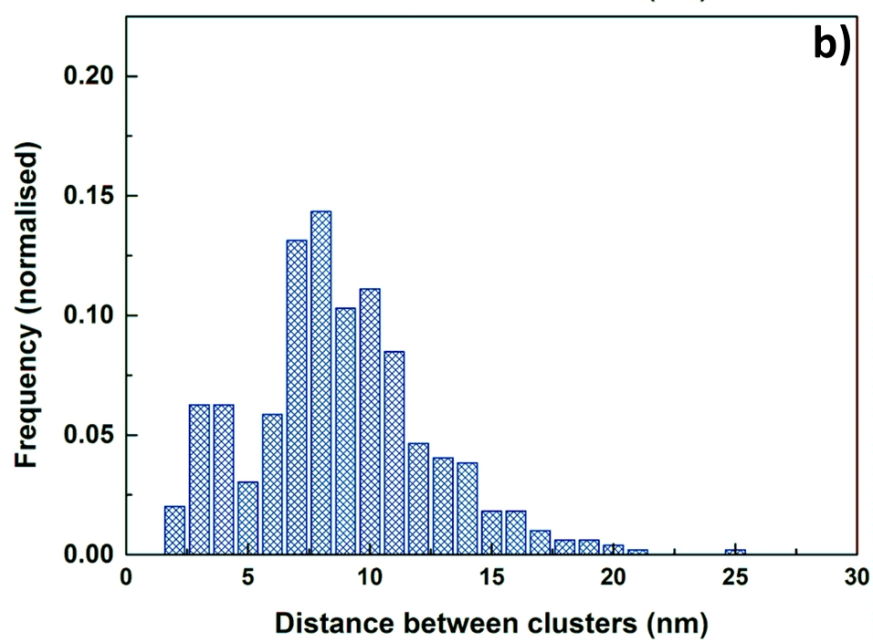
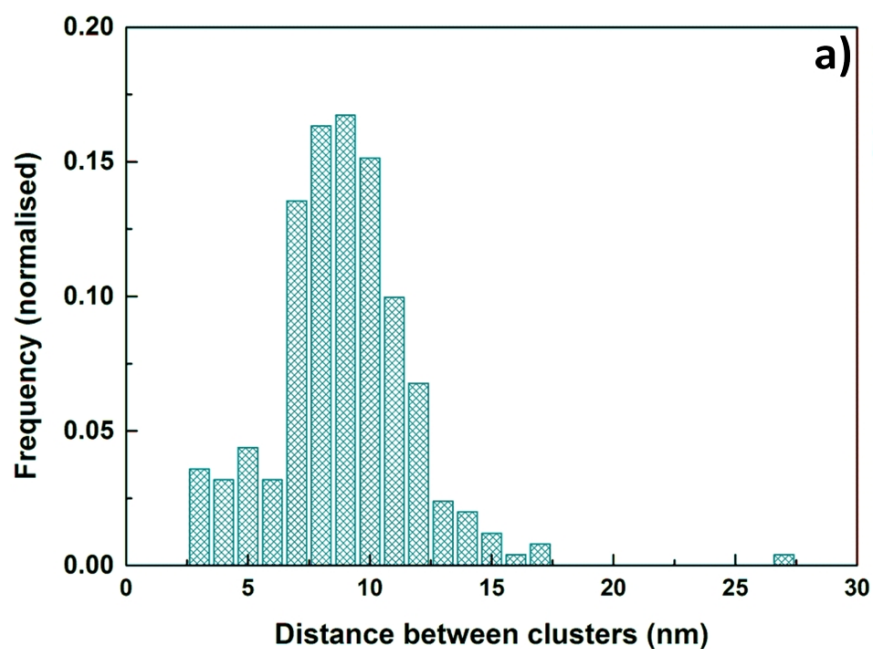


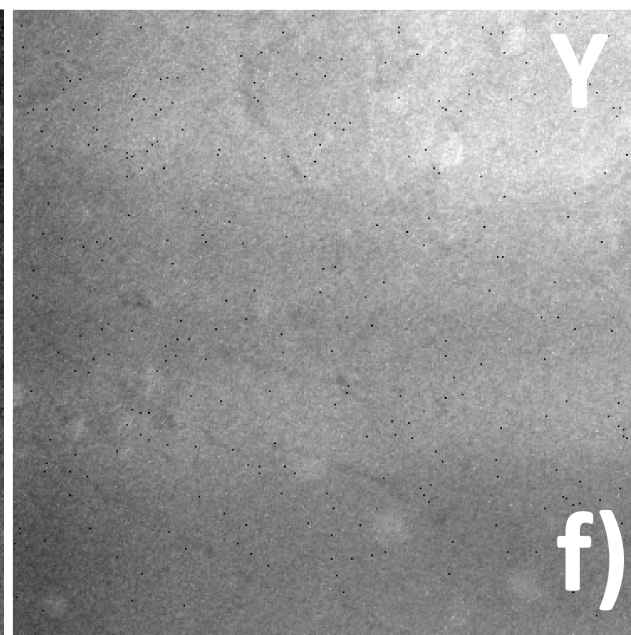
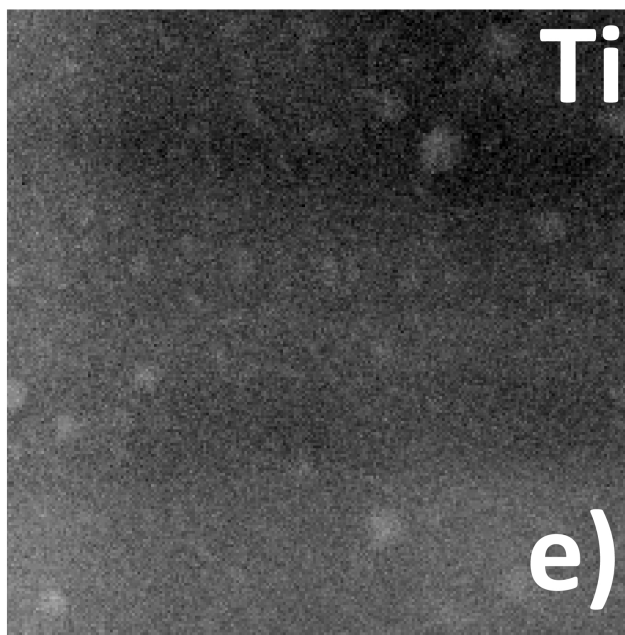
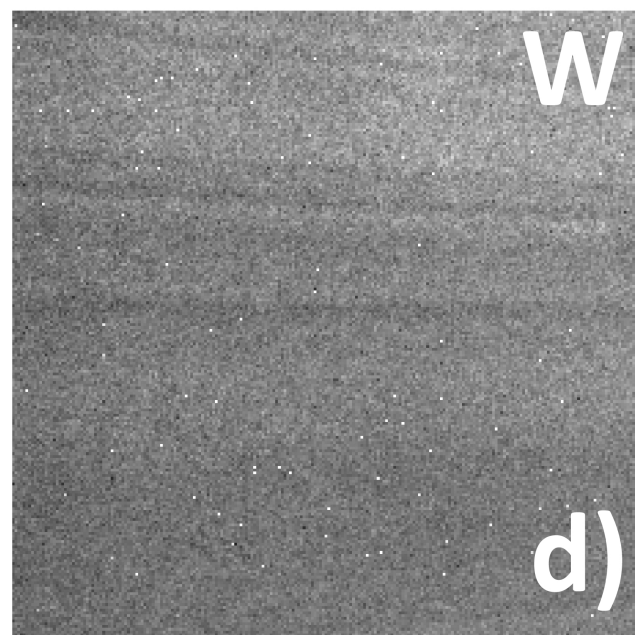
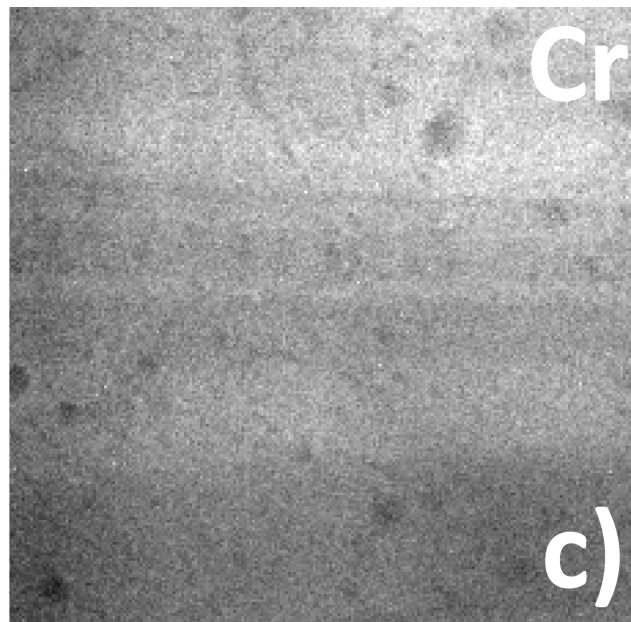
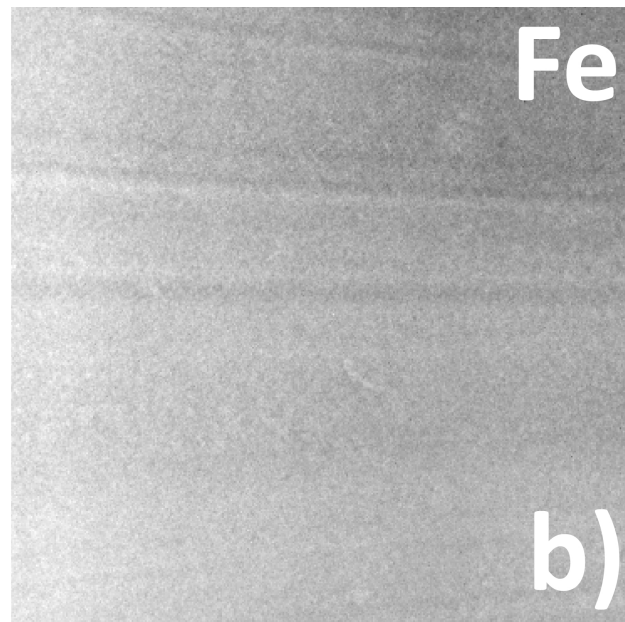
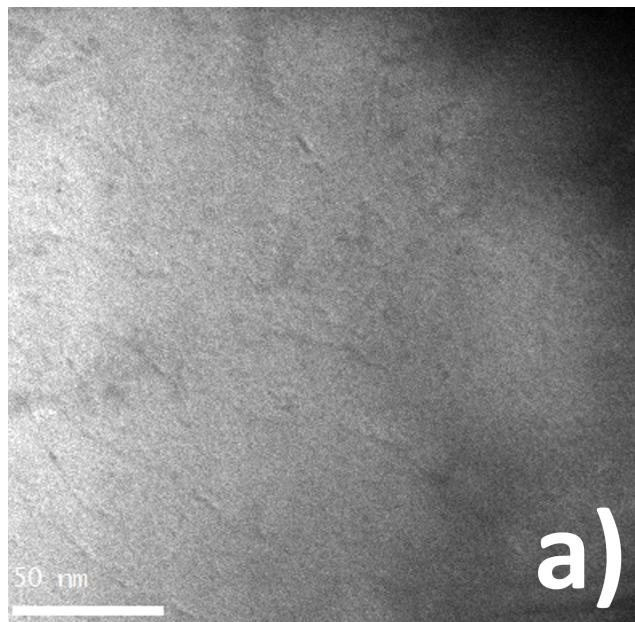


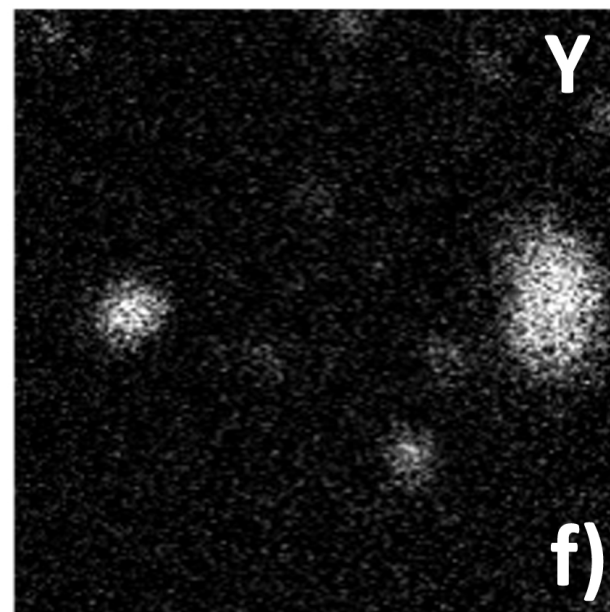
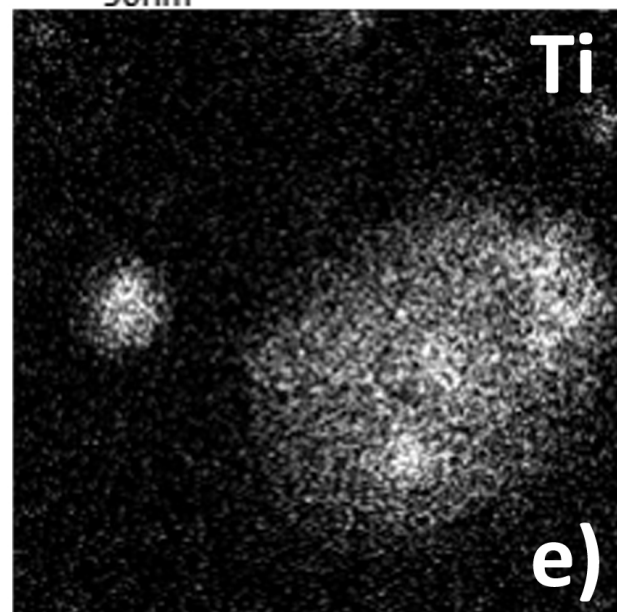
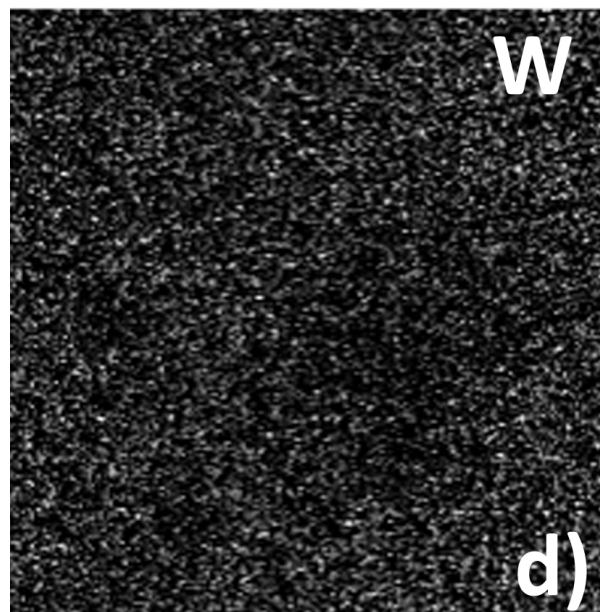
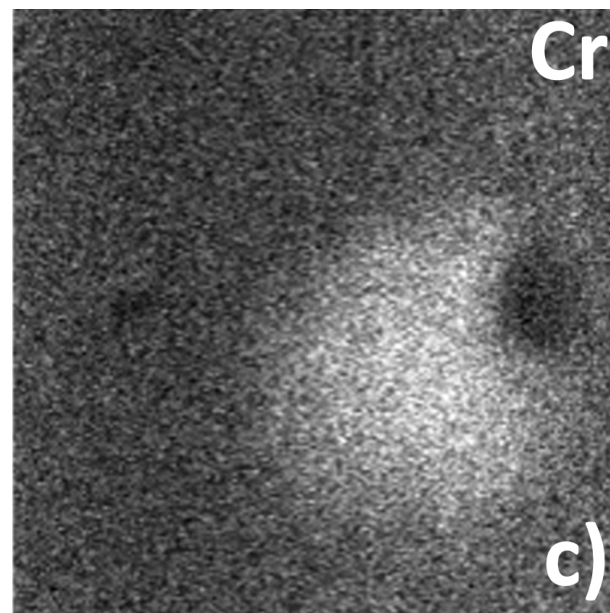
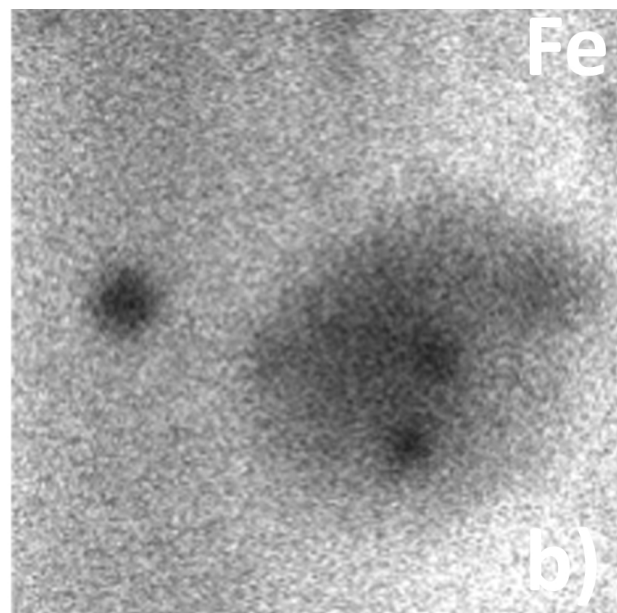
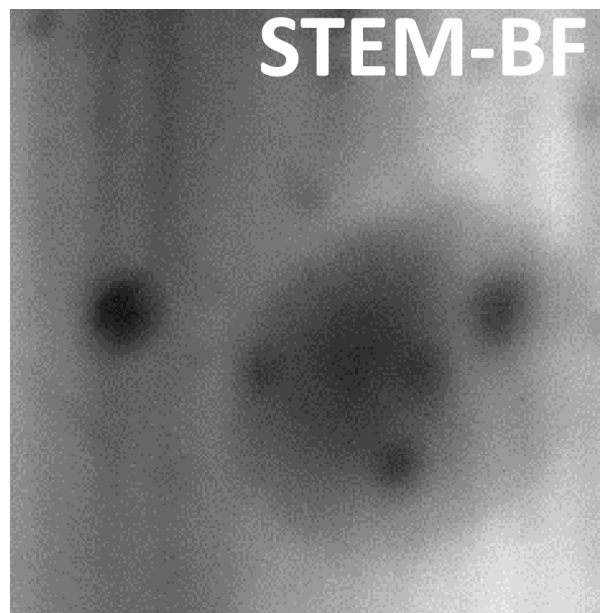
20 nm

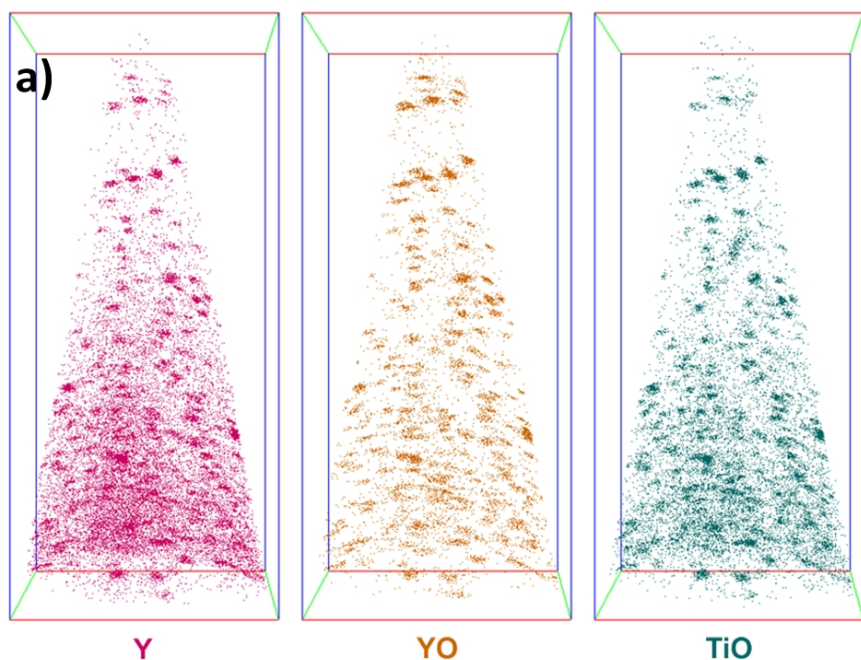




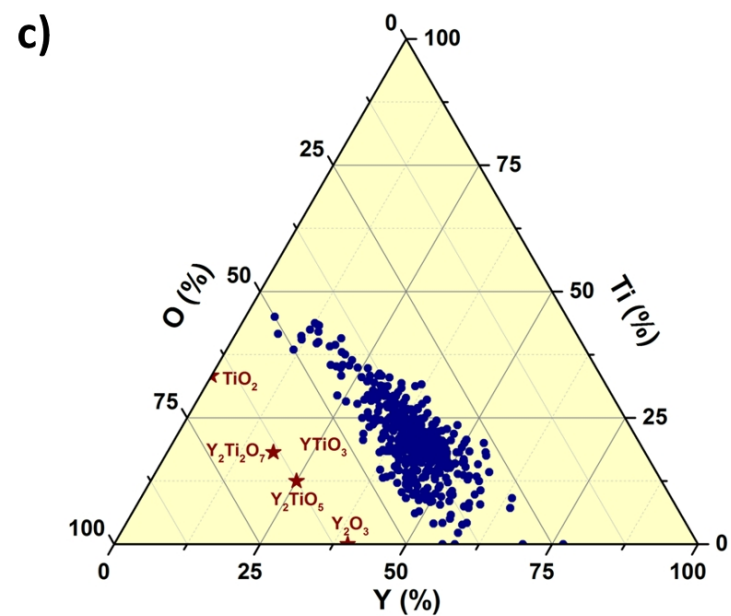
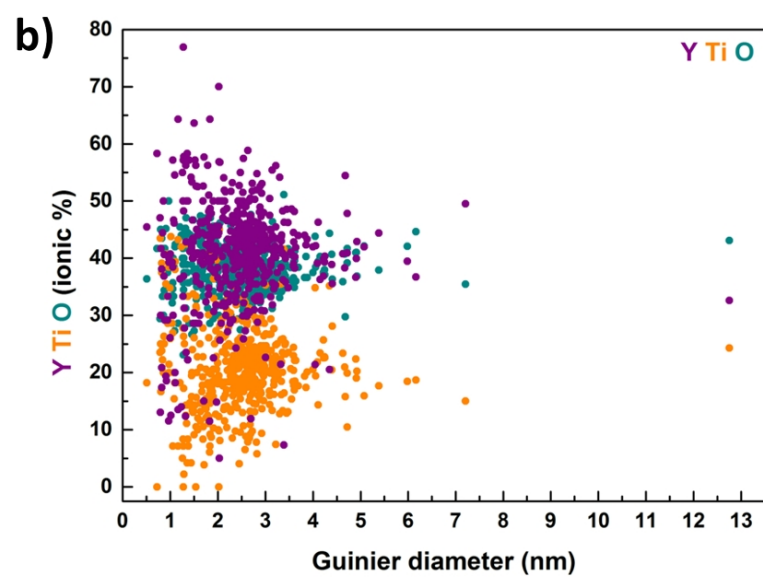


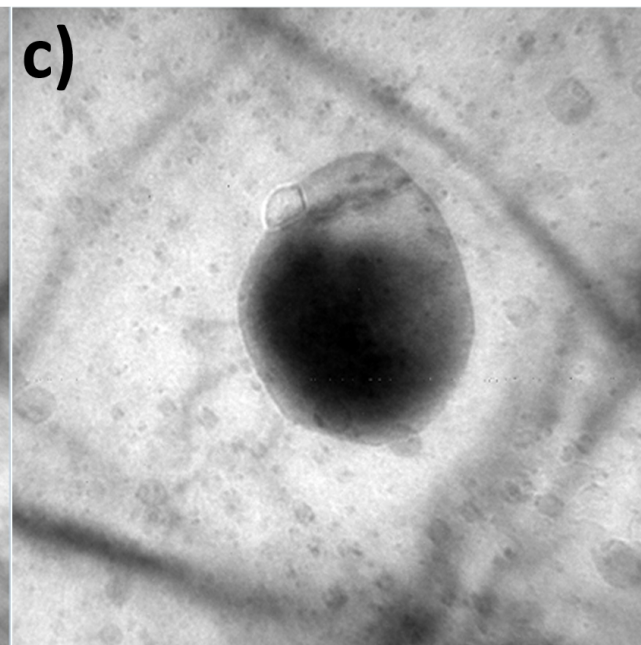
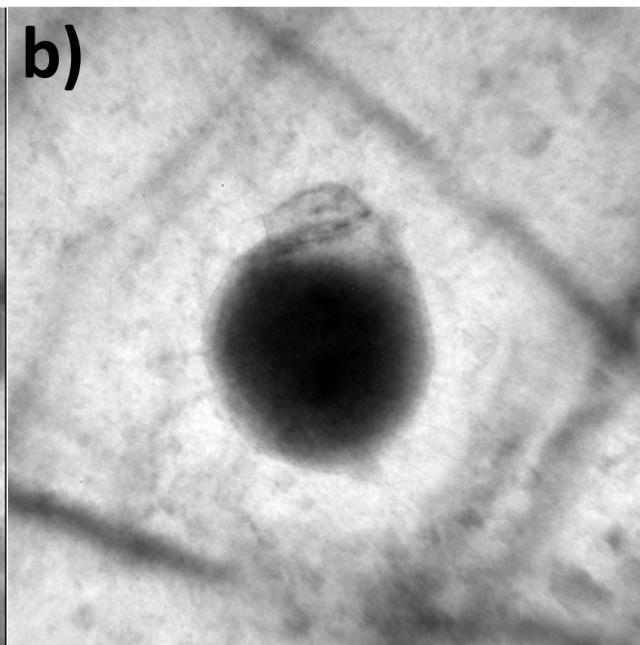
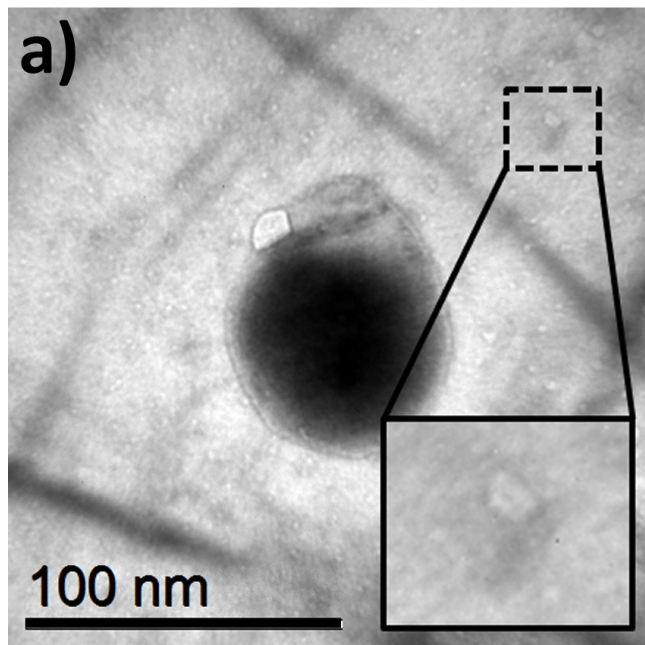


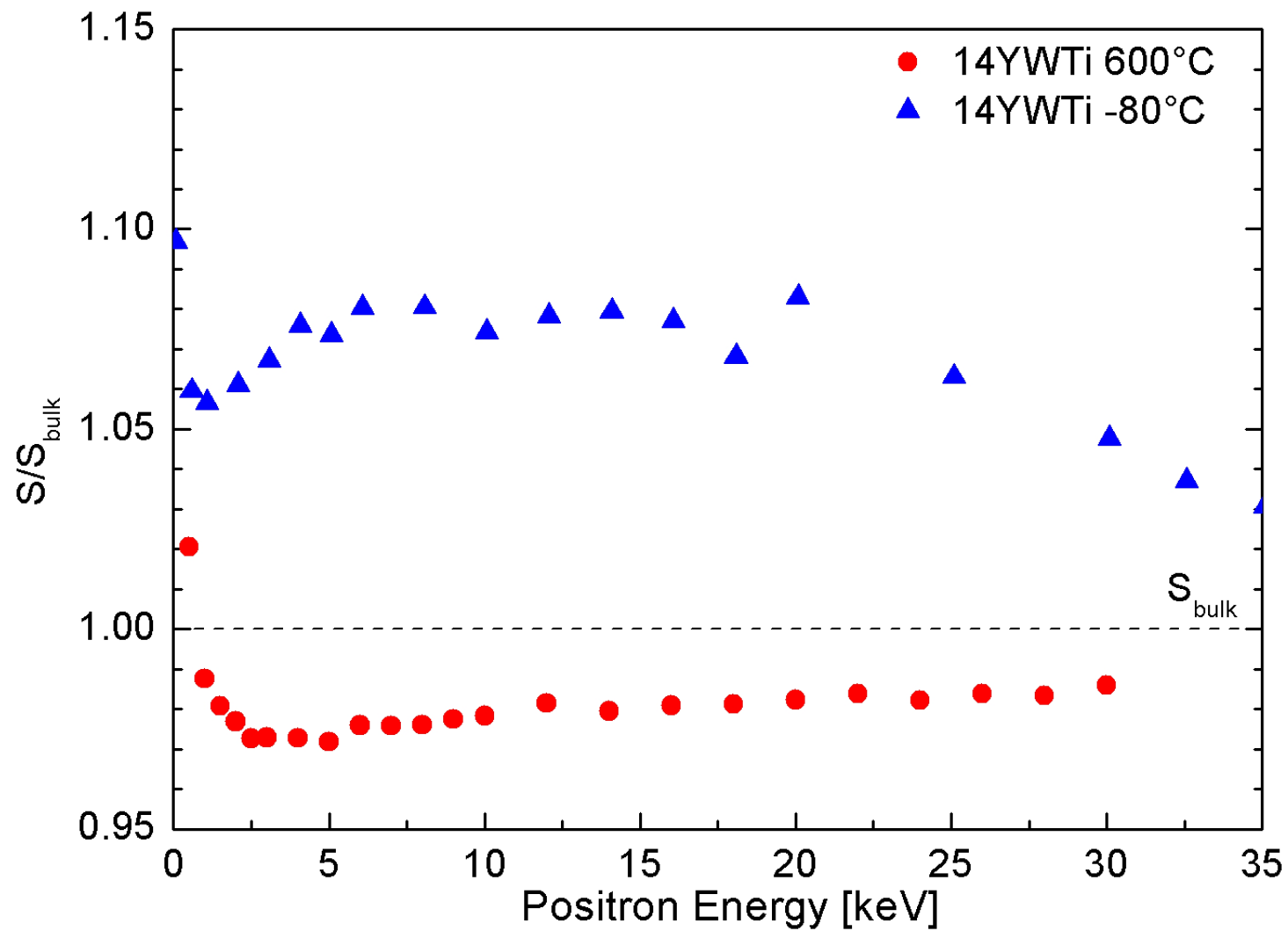


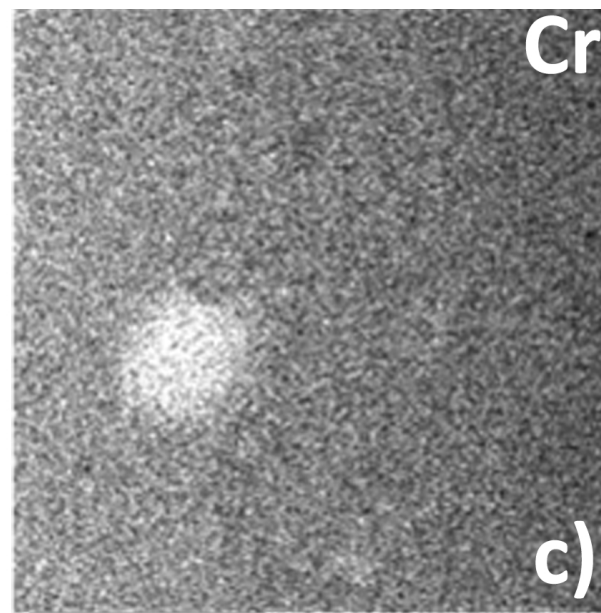
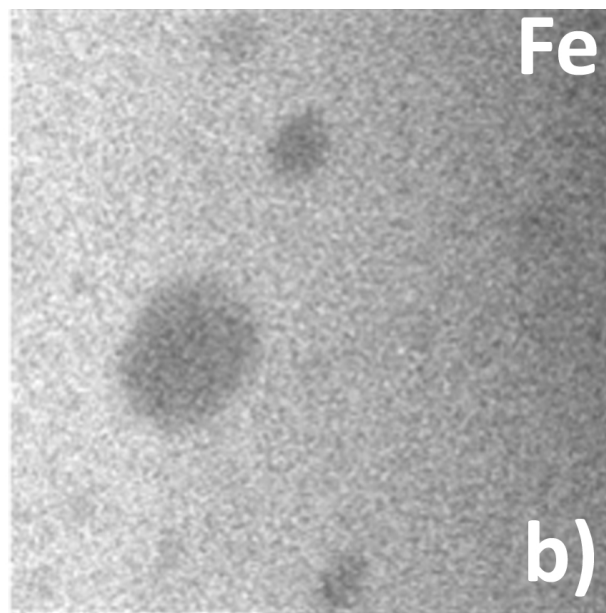
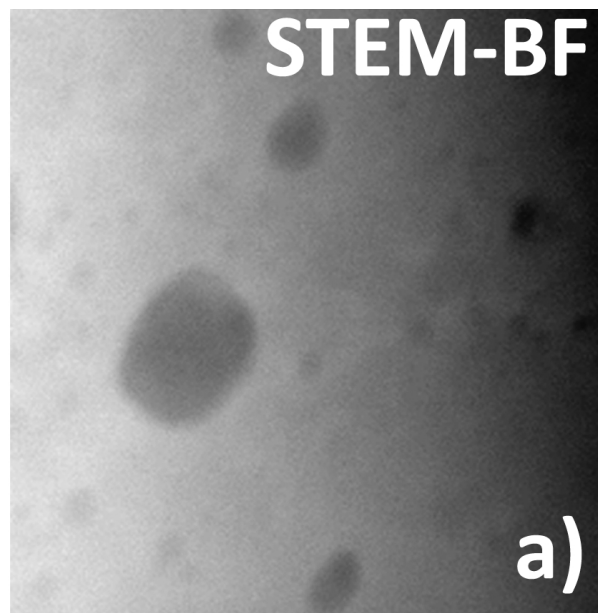


20 nm

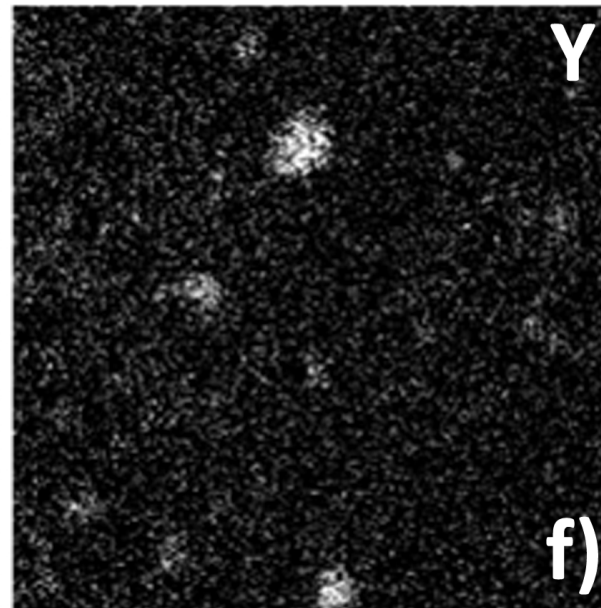
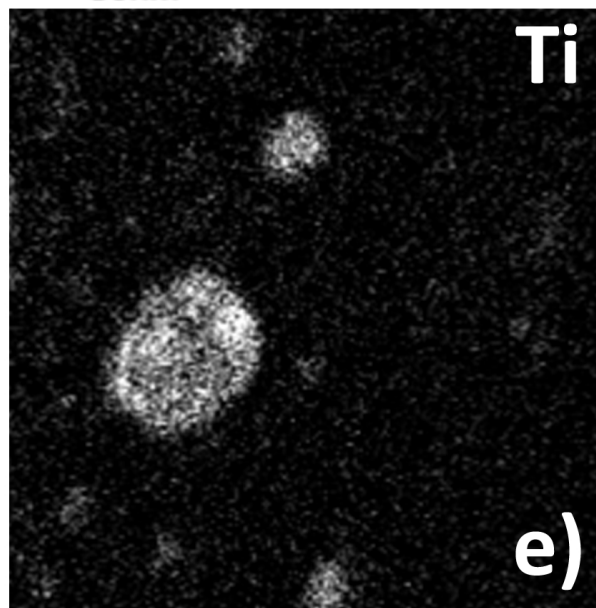
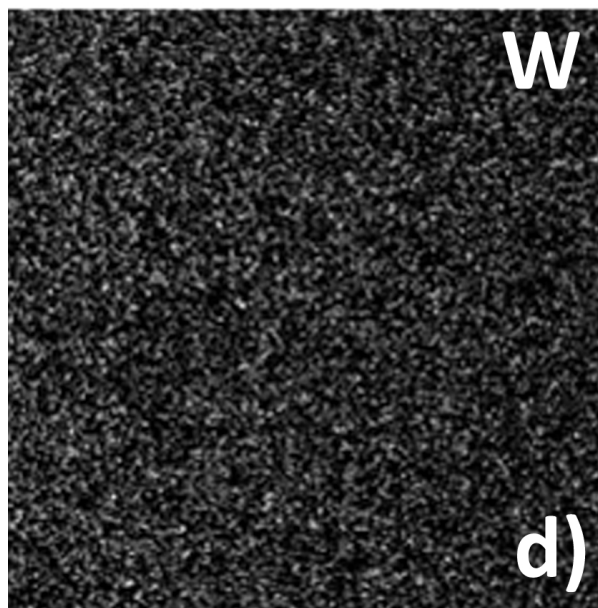


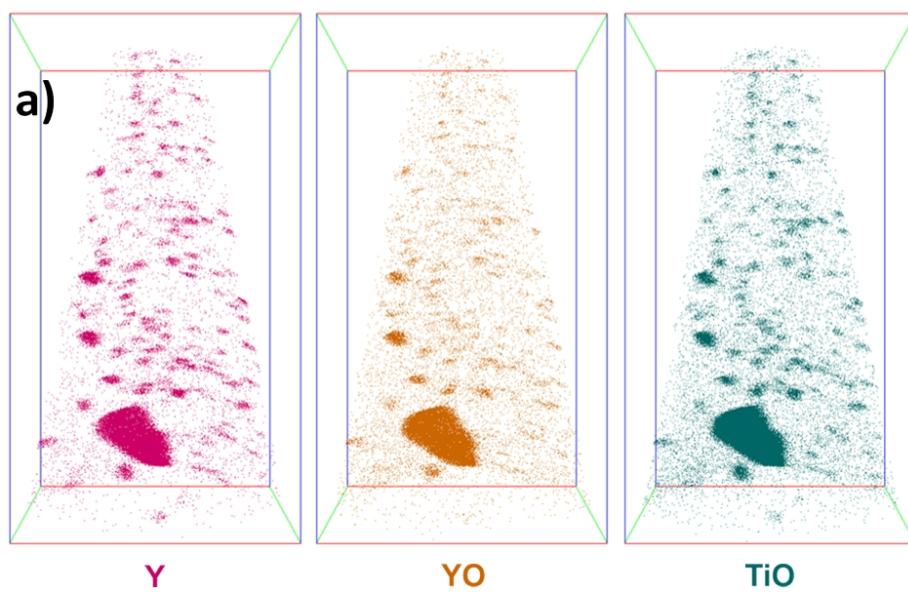






50nm





20 nm

